PROBA-V Image Quality Center (IQC) ATBD (US-05)

Status information

Security classification:	Project Confidential		State:	Final (for acceptance)
Current version number:	v1_7	Date of first issue:		22/06/2009
Prepared by:	Sindy Sterckx, Wouter Dierckx, Ils Reusen, Stefan Livens, Stefan Adriaensen, Geert Duhoux, Jan Biesemans	Date:		03/04/2013
Verified by:	PROBA-V PA team	Date:		03/04/2013
Approved by:	Jan Dries	Date:		03/04/2013

Copyright notice

Circulation / distribution list

Name	Address	P/E	Name	Address	P/E
PROBA-V team	VITO	E	Karim Mellab	ESA	E
			Juliette Kaysan	ESA	E
			Joe Zender	ESA	E

(P = Paper copy, E = Electronic version)

Document change record

Version	Date	Description	Affected sections	Editor(s)
0_1	29/10/2009	Initial (draft) version	All	**Error! Unknown document property name.**
	20/11/2009	PA modifications	2;3	Wouter Dierckx
1.0	10/02/2010	First release	All sections	**Error! Unknown document property name.**
1.1	17/06/2010	General review and update to current status:	3	Wouter Dierckx
		- sensor model is now with a fixed ADC gain and with nonlinearity correction as a first step	4.1	
		- masked edge pixels for dark current monitoring are no longer foreseen	4.3	
		- MTF algorithm description is compacted to the essential	4.9	
	22/06/2010	Change of solar irradiance file	4.4.1.2	Sindy Sterckx
		Update Visio with radiometric calculation, in line with sensor model update	Figure 10	
		Use of SPS and SPOT-VGT data for validation clarified	4.10	
		Updated graphs in Section on Cross Sensor calibration	4.10.1	Stefan Livens
1.2	14/09/2010	Corrected formulae in linear weighted model	4.6.2.3.2 and 4.6.2.3.4	Stefan Livens
1.3	28/09/2009	Sun glint error budget updated	Table 13	Sindy Sterckx
		NIR reflectance threshold modified	4.5.1.2.2.2	
		Resolution LUT modified	Table14	
		Aerosol data replaced by temp data	Figure 13	

Version	Date	Description	Affected sections	Editor(s)
1.4	28/04/2011	DCC cal : distance to coast removed; MODIS temp check removed	4.5.2	Sindy Sterckx
		Absolute calibration deserts modified	4.4.4	Sindy Sterckx
		Multi-temporal calibration deserts modified	4.5.3	Sindy Sterckx
		Cross-sensor calibration deserts modified	4.10.1	Stefan Livens/Sindy Sterckx
		Geometric calibration chapter deleleted, reference to ATBD geometry		
1.5	16/09/2011	Rayleigh: site depended CHL added	4.4.1.2.1.4	Sindy Sterckx
		cross-sensor deserts : outlier selection reference added	4.10.1.2.3	Sindy Sterckx
		Camera-to-camera : Usage of mean relative difference instead of mean difference	4.7.2.1	Sindy Sterckx
		Moon calibration: Under investigation removed	4.5.5	Sindy Sterckx
		Multiangular Calibraiton Antarctica: added theoretical background	4.8	Stefan Livens
1.6	25/10/2011	Update of Defect Pixel algo after internal review	4.3.2	Wouter Dierckx
	27/03/2013	Update Radiometric Sensor Model	4.2 4.3 4.7.2.2 4.8.3	Sindy Sterckx
		Update thermal behaviour	4.2.1.1	Wouter Dierckx
1.7	03/04/2013	Correction of dark current relation	4.2.1.1	Wouter Dierckx

TABLE OF CONTENTS

LIST OF TABLES

LIST OF FIGURES

1. INTRODUCTION

1.1 Scope

The present document is the Algorithm Theoretical Basis Document (ATBD) for the Image Quality Center of the PROBA-V User Segment (PV-02) project), under contract between VITO (supplier, Mol, Belgium,) and ESA (customer) as part of the PROBA-Vegetation (PROBA-V) project.

In the project Document Requirement List (DRL) [PVDOC-005] it is referred to as US-5.

The document provides a detailed description of the different algorithms that compose the Image Quality processing chains to monitor the sensor performance and to determine the parameters to be supplied to the processing facility (PF).

1.2 Applicability

This document defines the Algorithms Theoretical Basis of the Image Quality Center.

It has to be delivered to the customer at US-PDR, US-CDR. This document might be subject to change between the above mentioned review cycles and will reach a "final (accepted)" status at US-CDR.

2. REFERENCES

All applicable and reference documents for the PROBA-V PV02 project, either initiated by ESA or the consortium, are listed in [N77D7-PV02-PM-18-US-ApplicableAndReferenceDocumentsList].

2.1 Project reference documents

Project reference documents are listed in Table 1:

[PVDOC-005]	PROBA-V User Segment: Document Requirement List (DRL) and Document Requirement Description (DRD)
[PVDOC-623]	Detailed Processing Model IQC
[PVDOC-615]	User Segment Calibration Plan
[PVDOC-624]	Detailed Processing Model PF
[PVDOC-611]	Technical Note on Sun Glint
[PVDOC-034]	PROBA-V Vegetation Instrument : Thermal Design and Analysis Report
[PVDOC-068]	PROBA-V SPS Use Cases
[PVDOC-647]	PROBA-V TN on Radiometric calibration algorithms prototype results
[PVDOC-981]	Algorithm Theoretical Baseline Document Geometric Calibration

Table 1: Project reference documents

2.2 Other reference documents

Other reference docs (e.g. literature list) are listed below:

LIT1	Govaerts and Clerici, 2004	Govaerts, Y. and M. Clerici, 2004. Evaluation of radiative transfer simulations over bright desert calibration sites, IEEE Transactions on Geoscience and remote sensing 42(1), 176-187.
LIT2	Vermote et al., 1992	Vermote, E., R. Santer, P.Y. Deschamps, M. Herman, In-flight calibration of large field-of-view sensors at short wavelengths using Rayleigh scattering, Int. J. of Remote Sensing, 13, No18, 1992.
LIT3	Hagolle et al., 1999	Hagolle, O., P. Goloub, P-Y. Deschamps, H. Cosnefroy , X. Briottet, T. Bailleul, J.-M. Nicolas, F. Parol, B. Lafrance, M. Herman, Results of POLDER In-Flight Calibration, IEEE Transactions on Geoscience and Remote Sensing, Vol. 37, No. 3 (1999)
LIT4	Fougnie et al., 2007	Fougnie, B., G. Bracco, B. Lafrance, C. Ruffel, O. Hagolle, C. Tinel, PARASOL in-flight calibration and performance, Applied Optics, vol. 46, No. 22 (2007)

LIT5	Martiny et al., 2005	Martiny N., R. Santer, I. Smolskaia, Vicarious calibration of MERIS over dark waters in the near infrared, Remote Sensing of Environment 94 (2005) 475–490
LIT6	Vermote et al., 2008	6SV manual, http://6s.ltdri.org/6S_code2_thiner_stuff/6s_ltdri_org_manual.htm
LIT7	Thuillier et al., 2003	Thuillier, G., M. Hersé, P. C. Simon, D. Labs, H. Mandel, D. Gillotay, and T. Foujols, 2003, "The solar spectral irradiance from 200 to 2400 nm as measured by the SOLSPEC spectrometer from the ATLAS 1-2-3 and EURECA missions, Solar Physics, 214(1): 1-22
LIT8	Gordon and Wang, 1994	Howard R. Gordon and Menghua Wang, "Retrieval of water-leaving radiance and aerosol optical thickness over the oceans with SeaWiFS: a preliminary algorithm," Appl. Opt. 33, 443-452 (1994)
LIT9	Shettle and Fenn, 1979	Shettle, E. and R.W. Fenn, Models for the Aerosols of the Lower Atmosphere and the Effects of Humidity Variations on their Optical Properties, AFGL-TR-79-0214, Environmental Research Paper, No. 676
LIT10	Morel, 1988	A. Morel, Optical modeling of the upper ocean in relation to its biogenous matter content (case I waters), *Journal of Geophysical Research*, 93(C9), 10749-10768, 1988
LIT11	Fougnie et al., 2002	Fougnie, B., P. Henry, A. Morel, D. Antoine and F. Montagner, Identification and Characterization of Stable Homogeneous Oceanic Zones: Climatology and Impact on In-flight Calibration of Space Sensor over Rayleigh Scattering, Proceedings of Ocean Optics XVI, Santa Fe, New Mexico, 18-22 November 2002
LIT12	Kotchenova and Vermote, 2007	Svetlana Y. Kotchenova and Eric F. Vermote, "Validation of a vector version of the 6S radiative transfer code for atmospheric correction of satellite data. Part II. Homogeneous Lambertian and anisotropic surfaces," Appl. Opt. 46, 4455-4464 (2007)
LIT13	Gordon et al., 1988	Gordon, H. R., O. B. Brown, R. H. Evans, J. W. Brown, R. C. Smith, K. S. Baker, and D. K. Clark (1988), A semianalytic radiance model of ocean color, J. Geophys. Res., 93, 10,909– 10,924.
LIT14	Wang, 2005	M. Wang, A refinement for the Rayleigh radiance computation with variation of the atmospheric pressure, Int. J. Remote Sens. 26, 5651–5653 (2005).
LIT15	Tanré et al., 1990	D. Tanré, C. Deroo, P. Duhaut, M. Herman, J. J. Morcette, J. Perbos and P. Y.Deschamps, Description of a computer code to simulate the satellite signal in the solar spectrum: 5S

		code. Int. J. Remote Sensing,11,659-668 (1990).
LIT16	Rahman and Dedieu, 1994	Rahman H., Dedieu G. 1994: SMAC : a simplified method for the atmospheric correction of satellite measurements in the solar spectrum Int. J. Remote Sensing, vol.15, no.1, 123-143.
LIT17	Teillet et al, 2007	Teillet, P.M., J.A. Barsi, G. Chander, and K.J. Thome (2007). Prime Candidate Earth Targets for the Post-Launch Radiometric Calibration of Space-Based Optical Imaging Instruments. Proc. SPIE 6677, San Diego, 2007
LIT18	Biggar et al., 2003	Stuart F. Biggar, Kurtis J. Thome, and Wit Wisniewski, Vicarious Radiometric Calibration of EO-1 Sensorsby Reference to High-Reflectance Ground Targets, IEEE TRANSACTIONS ON GEOSCIENCE AND REMOTE SENSING, VOL. 41, NO. 6, JUNE 2003.
LIT19	Thome, 2001	K.J. Thome, 2001, Absolute radiometric calibration of Landsat 7 ETM+ using the reflectance-based method, Remote Sensing of Environment 78 (2001) 27– 38
LIT20	Dinguirard and Slater, 1999	Calibration of Space-Multispectral Imaging Sensors: A Review, Remote Sens. Environ. 68:194-205 (1999).
LIT21	Biggar et al., 1994	Biggar S.F., Slater P.N., and Gellman D.I., Uncertainties in the in-flight calibration of sensors with reference to measured ground sites in the 0.4 to 1.1 μm range. Rem. Sens. Environ. 48: 245-252
LIT22	Itten et al., 2008	Itten, K.I.,. F. Dell'Endice, A. Hueni , M. Kneubühler,D. Schläpfer, D. Odermatt, F. Seidel, S. Huber, J. Schopfer, T. Kellenberger, Y. Bühler, P. D'Odorico, J. Nieke, E. Alberti, and Koen Meuleman, APEX – the Hyperspectral ESA Airborne Prism Experiment, Sensors 2008, 8, 6235-6259
LIT23	Biesemans et al., 2007	Biesemans J., Sterckx, S., E. Knaeps, K. Vreys, S. Adriaensen, J. Hooyberghs, K. Meuleman, P. Kempeneers, B. Deronde, J. Everaerts, J. Schlaepfer and J. Nieke (2007) ; Image Processing Workflows For Airborne Remote Sensing. Proceedings 5th EARSeL Workshop on Imaging Spectroscopy. Bruges, Belgium ; eds. I. Reusen.
LIT24	Nieke, 2001	Nieke J., Technical Note 1 Compilation of Scientific Variables, Specification of an airborne spectroradiometer to calibrate and validate spaceborne Earth Observation sensors, 2001

LIT25	Teillet et al., 2001	P.M. Teillet, G. Fedosejevs, R.P. Gauthier, N.T. O'Neill, K.J. Thome, S.F. Biggar, H. Ripley, A. Meygret, A generalized approach to the vicarious calibration of multiple Earth Observation sensors using hyperspectral data, Remote Sensing of Environment 77 (2001) 304-327
LIT26	Hovis et al., 1985	W.A. Hovis, J.S. Knoll, G.R. Smith; Aircraft measurements for calibration of an orbiting spacecraft sensor; Appl. Optics; Vol. 24; pp 407-410 (1985)
LIT27	Hagolle et al., 2004	Hagolle, O., Nicolas, J.-M., Fougnie, B., Cabot, F. and Henry P. (2004)..Absolute calibration of VEGETATION derived from an interband method based on the Sun glint over ocean. IEEE Transactions on Geoscience and Remote Sensing, 42(7): 1472 – 1481.
LIT28	Cox and Munk,1954	Cox and Munk, Measurement of the roughness of the sea surface from photographs of the Sun's glitter, *J. Opt. Soc. Am.*, *44*, 838–850, 1954
LIT29	Born and Wolf,1975	Born, M. and Wolf, E., 1975. Principles of Optics. In: , Pergamon, Oxford, p. 90.
LIT30	Hale and Querry,1973	Hale and Querry,1973. Optical Constants of Water in the 200-nm to 200-μm Wavelength Region," Appl. Opt. 12, 555-563**,**1973.
LIT31	Lafrance et al., 2002	Lafrance B., Hagolle O., Bonnel B., et al., 2002 : Interband calibration over clouds for POLDER space sensor. IEEE Trans Geosc. Rem. Sens., 40 (1): 131-142
LIT32	Henry and Meygret, 2001	Henry and Meygret 2001. Calibration of HRVIR and VEGETATION cameras on SPOT4. COSPAR 2000. Advances in Space Research 28 1 (2001), pp. 49–58.
LIT33	Sohn et al., 2009	Sohn B, Ham S,Yang P (2009) Possibility of the Visible-Channel Calibration Using Deep Convective Clouds Overshooting the TTL. Journal of Applied Meteorology and Climatology 48(11): 2271
LIT34	Hu and Stamnes,1993	Hu, Y.X. and K. Stamnes, An Accurate parameterization of the Radiative Properties of Water Clouds Suitable for Use in Climate Models. J. Climate, 6, 728--742, 1993.
LIT35	Baum et al,2005	Baum, B. A., A. J. Heymsfield, P. Yang, and S. T. Bedka, 'Bulk scattering models for the remote sensing of ice clouds. Part 1: Microphysical data and models', 2005, J.Appl. Meteor., 44, 1885-1895 Baum, B. A., P. Yang, A. J. Heymsfield, S. Platnick, M. D. King, Y.-X. Hu, and S. T. Bedka, 'Bulk scattering models for the remote sensing of ice clouds. Part 2: Narrowband models', 2005, J. Appl. Meteor.,

		44, 1896-1911. Baum, B. A., P. Yang, S. L. Nasiri, A. K. Heidinger, A. J. Heymsfield, and J. Li, 'Bulk scattering properties for the remote sensing of ice clouds. Part 3: High resolution spectral models from 100 to 3250 cm-1.', 2007, J. Appl. Meteor. Clim., Vol. 46,423-434.
LIT36	Zhang et al., 2009	Zhang, Z., P. Yang, G. W. Kattawar, J. Riedi, L. C-Labonnote, B. A. Baum, S. Platnick, and H. L. Huang, 2009: Influence of ice particle model on satellite ice cloud retrieval: lessons learned from MODIS and POLDER cloud product comparison. *Atmos. Chem. Phys.*, 9, 7115-7129
LIT37	Lattanzio et al., 2006	Lattanzio, A., P. D. Watts, and Y. Govaerts, 2006: Activity report on physical interpretation of warmwater vapour pixels, EUMETSAT, Technical Memorandum 14.
LIT38	Cosnefroy et al., 1996	Cosnefroy, H., M. Leroy, and X. Briottet, 1996: Selection and characterization of Saharan and Arabian desert sites for the calibration of optical satellite sensors, Reomte Sensing Env., 58, 101- 114
LIT39	Rahman et al., 1993	Rahman, H., Pinty, B. and Verstraete, M. M. (1993) Coupled surface-atmosphere reflectance (CSAR) model 2. Semiempirical surface model usable with NOAA Advanced Very High 93 Resolution Radiometer data. Journal of Geophysical Research, 98, pp. 20791-20801.
LIT40	Stone, 2008	Stone, 2008. Use of the Moon for in-flight calibration stability monitoring QA4EO-WGCV-IVO-CLP-001 (CEOS Cal/val portal) (2008).
LIT41	Govaerts et al., 2004	Govaerts, Y. M., M. Clerici, et al. (2004). "Operational Calibration of the Meteosat Radiometer VIS Band." IEEE Transactions on Geoscience and Remote Sensing 42(9): 1900-1914.
LIT42	Bruegge et al., 1999	C. Bruegge , N. Chrien, D. Diner ATBD-MISR-02 MISR: Level 1 In-Flight Radiometric Calibration and Characterization December 13, 1999
LIT43	Levenson et al, 2000	Levenson, M.S. et al: An approach to combining results from multiple methods motivated by the ISO GUM, J. Res Natl. Stand. Technol. 105, 571 (2000)
LIT44	Galbraith et al.	Amy Galbraith, James Theiler, and Steve Bender. Resampling Methods for the MTI Coregistration Product. Proceedings SPIE 5093.

LIT45	Press et al, 2007	Press W.H., Teukolsky S. A., Vetterling W.T., Flannery B.P., 2007: Numerical recipes: the art of scientific computing
LIT46	Fougnie et al, 2000	Fougnie, B., Henry, P., Cabot, F., Meygret, A. and Laubies, M.-C, 200, Vegetation: in-flight multi-angular calibration, in Earth Observing Systems V, Proc. SPIE 4135, 331-338
LIT47	Fox, 2004	Fox, N. Validated data and removal of bias through traceability to SI units, Post-Launch Calibratin of Satellite Sensors – Morrain & Budge (eds), 2004 Taylor & Francis group
LIT48	Zhang et al., 2000	Zuxun Zhang, Jlanqlng Zhang, Mlngsheng Uao, and U Zhang. Automatic Registration of Multi-Source Imagery Based on Global Image Matching. Photogrammetric Engineering & Remote Sensing Vol. 66, No. 5, May 2000, pp. 625-629.
LIT49	Canters et al., 2009	J. Ma , J.C.-W. Chan , F. Canters. Automatic image registration of multi-angle imagery for CHRIS/PROBA. 6th EARSeL SIG IS workshop, March 16-19, 2009, Tel Aviv, Israel
LIT50	Tempelmann et al.	Udo Tempelmann, Ludger Hinsken, Utz Recke. ADS40 Calibration & Verification Process. Proceedings of the ISPRS WG1/5 International workshop.
LIT51	Hagolle and Cabot, 2002	Hagolle O;, Cabot F.: Absolute calibration of MERIS using natural targets. Proceedings of "MERIS level 2 validation workshop, Frascati, Italy, DeC. 13-14, 2002.
LIT52	Hagolle and Cabot, 2003	Hagolle O. , Cabot F., Absolute Calibration Of Meris Using Natural Targets, MAVT 2003 proceeding.
LIT53	Morel and Gentili, 2009	Morel A, Gentili B.,A simple band ratio technique to quantify the colored dissolved and detrital organic material from ocean color remotely sensed data, Remote Sensing of Environment,2009, 113:998-1011
LIT54	Morel et al. 2010	Morel A., Claustre H. and Gentili, B. . The most oligotrophic subtropical zones of the global ocean: similarities and differences in terms of chlorophyll and yellow substance. Biogeosciences Discuss. ,2010,7: 5047-5079.
LIT55	Morel et al.,2007	Morel A., Claustre H., Antoine, D. abd Gentili, B. Natural variability of bio-optical properties in Case 1 waters: attenuation and reflectance within the visible and near-UV spectral domains as observed in South Pacific and Mediterranean waters.

		Biogeosciences,2007,4:913-925.
LIT56	Fougnie et al.,2010	Bertrand Fougnie, Jérome Llido, Lydwine Gross-Colzy, Patrice Henry and Denis Blumstein, "Climatology of oceanic zones suitable for in-flight calibration of space sensors", Proc. SPIE 7807, 78070S (2010); doi:10.1117/12.859828

Table 2: Literature references

3.   TERMS, DEFINITIONS AND ABBREVIATED TERMS

General terms, definitions and abbreviations used within the scope of this document are listed in [PVDOC-303] Directory of Acronyms and Abbreviations.

Abbreviations and acronyms used within the scope of this document are listed in Table 3:

6SV	Second Simulation of a Satellite Signal in the Solar Spectrum, Vector
AGL	Above ground level
AOT	Aerosol Optical Thickness
CCD	Charge Coupled Device
CMOS	Complementary Metal Oxide Semiconductor
DCC	Deep Convective Clouds
FWHM	Full Width at Half Maximum
IVOS	Infrared and Visible Optical Systems
LST	Local Solar Time
PDF	probability distribution function
ROLO	Robotic Lunar Observatory
RVP	Rahman-Pinty-Verstraete
WGCV	Working Group Calibration/Validation

Table 3: Abbreviations and acronyms

4.   RADIOMETRIC CALIBRATION

4.1   Introduction

The assessment of the PROBA-V performance, the analysis of the image quality and the calibration after launch will be performed by the PROBA-V Image Quality Center (IQC). Due to outgassing phenomena during launch, aging of the optical parts and cosmic ray damage variation in the characteristics of PROBA-V instrument are likely to occur in orbit, necessitating the need for in-orbit stability monitoring and calibration. The Image Quality Center will ensure the highest possible image quality, both radiometrically and geometrically. Given the constraints on power consumption and the small size and weight of the platform (160 kg) vicarious calibration techniques will be used to monitor sensor performance over time.

In this document the algorithms used by IQC to monitor the sensor performance and to determine the parameters to be supplied to the processing facility (PF) are described in detail. Related documents are : [PVDOC-624] which gives the details of the processing to be applied to the PROBA-V images ; The calibration plan [PVDOC-615] which contains details on calibration zones, frequency of calibration and instrument setting .

To cover the wide angular field of view (101°) the optical design of PROBA-V is made up of three cameras (identical Mirror Anastigmatic (TMA) Telescopes). Each camera has 2 focal planes, one for the short wave infrared (SWIR) band and one for the visible and near-infrared (VNIR) bands. The VNIR detector consists of 4 lines of 5200 pixels. Three spectral bands are selected, compatible with SPOT-Vegetation: BLUE, RED and NIR. The SWIR detector is a linear array composed of 3 mechanically butted detectors of 1024 pixels. The correspondence between instrument design and captured image data is schematically represented in Figure 1.
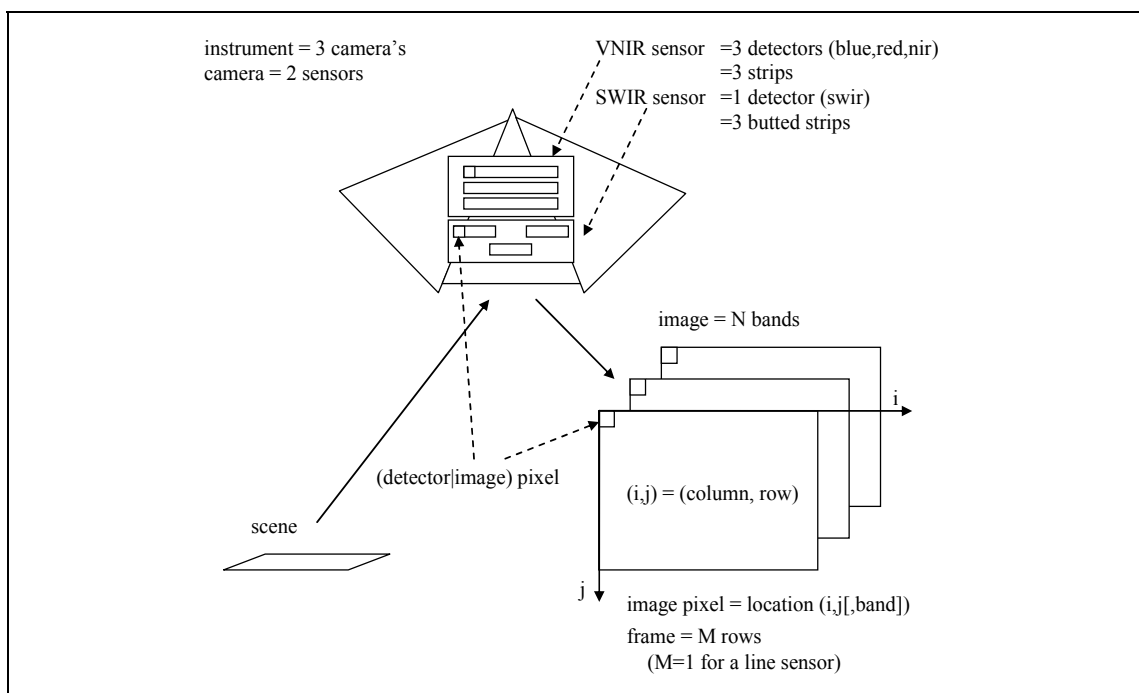
Figure 1: Conceptual overview

The three PROBA-V cameras are treated separately in the in-flight radiometric calibration, except in section (4.7) where possible biases between cameras are analysed.

In section 4.2 the radiometric model is given. It describes the conversion of the digital output of a pixel to the at-sensor spectral radiance. In this section special attention is given to temperature effects due to lack of an active thermal control mechanism. The conversion of digital numbers to spectral radiances is achieved through the use of the different sensor calibration coefficients.

These are: dark currents, absolute calibration coefficients and equalization/non-uniformity/multi-angular coefficients. The initial values of the calibration parameters is fixed by the pre-launch calibration measurements. After launch these parameters are monitored, validated and, if needed, updated by the vicarious calibration activities described in the subsequent sections.

In section 4.3 first the algorithms to define the dark currents per pixel are described (section 4.3.1). Degraded or defect pixels can be detected using the algorithms given in section 4.3.2. As a linear radiometric model is assumed, it is essential that any deviation from this assumed linearity can be detected. The in-flight approach for detecting deviations from non-linearity is described in 4.3.3.

In the next three section (4.4, 4.5 and 0) the methods for in-flight calibration of the absolute calibration coefficients are given. Several different and independent approaches will be used as
- ⇨ The methods are not always suitable for all bands and combination of methods are needed to allow accurate calibration of all spectral bands
- ⇨ Independent validation of the results is required to determine and to account for systematic errors in one or more techniques. For instance uncertainties in the characterization of target BRDF or assumptions in aerosol characteristics can induce systematic errors (Govaerts and Clerici., 2004 [LIT1]).
- ⇨ Some methods can only be used during a few months in the year (eg. calibration over Antarctica)
- ⇨ One method is not sufficient to cover the full dynamic range of the sensor : bright (e.g. deserts) versus dark calibration areas (e.g. oceans)
- ⇨ The uncertainty in the calibration results can be decreased by consistency check of the different methods the procedures are often limited to a few spectral bands

A distinction has been made between absolute (4.4) and relative calibration methods (4.5). The operational absolute calibration for BLUE and RED PROBA-V bands can be performed using the so-called Rayleigh calibration approach (4.4.1). Other approaches are the reflectance based methods (4.4.2) and underflights with the APEX sensor (4.4.3). Due to the high operational costs for these latter two methods they can't however be used frequently, and therefore they are mainly considered for validation purposes. The results of the Rayleigh calibration method can be transferred to other bands (NIR, SWIR) based on a 'relative' inter-band calibration approach that uses almost spectrally invariant targets as sun glint (4.5.1) or deep convective clouds (which is not suitable for SWIR) (4.5.2). Temporally stable targets are ideal for monitoring the stability of PROBA-V. Suitable targets for multi-temporal calibration are stable deserts (4.5.3), Antarctica (4.5.4) and even the moon (4.5.5) .

To reduce both random and systematic error effects, calibration coefficients derived over a large number of images and obtained with different methods will be statistically averaged. The statistical approach used to determine the absolute calibration coefficient to be used by the processing facility is detailed in 0.

In the absolute and relative calibration methods the three cameras are treated separately, which may introduce biases between the cameras. In the overlap zone, targets are simultaneously seen by 2 independent cameras. In 4.7 it is described how this overlap zone can be used to indicate possible bias between cameras.

The in-flight monitoring and calibration of the equalization coefficients is described in 4.8. The equalization coefficient can be split up in a low and a high frequency term. The in-flight determination of the low frequency is performed using stable deserts with know bidirectional effects. High frequency variation can be assessed using images over Antarctica or Greenland (4.8.3.4).

The algorithms for assessment of the general instrument image quality are given in section 4.9. The section describes noise analyses (4.9.1) , MTF measurement (4.9.2) and the quantification of SNR (4.9.3).

In section 4.10 is described how these algorithms will be validated before and after launch. In order to secure proper data continuity and consistency between SPOT-VGT and PROBA-V cross sensor calibration is essential. The necessity of almost simultaneous observations can be overcome by the use of stable sites as deserts or Antarctica. This approach is described in 4.10.1. This cross-sensor calibration is also considered as independent validation of routine calibration.

4.2   Sensor Radiometric Model

4.2.1   Model overview

The Sensor Radiometric Model defines the relation between the raw digital output which is registered by the sensor and sent down for data processing, and the derived effective spectral radiance assumed to be present at the sensor. This model will be used in two stages:

- **pre-launch calibration**: at this stage, both the digital output and the input effective spectral radiance are known up to a given accuracy, and the calibration parameters determining the relation between both can be derived;
- **post-launch calibration**: at this stage, the effective radiance must be derived from the digital output and the calibration parameters currently used. The initial values of the calibration parameters is fixed by the pre-launch calibration measurements, these parameters are then updated and validated by the vicarious calibration activities described in the subsequent sections.

The mathematical model representing the radiometric response of PROBA-V is :

$$DN_{i,g,T}^k = AVG_g\left(dc_{i,g,T}^k\left(IT+dIT^k\right)+off_{i,g}^k+L^k.A_T^k\cdot g_{i,g}^k\left(IT+dIT^k\right)\right)+NL_g^k$$

with

- k denotes the spectral band;
- i is the pixel index;
- g is the gain setting;
- T is the detector temperature;
- DN is the digital number.

where

- $dc_{i,g,T}^k$ is the dark current coefficient. This coefficient depends on the temperature and for the SWIR detectors it is also gain setting dependent
- IT the integration time
- dIT^k is the so-called integration time offset, a parameter introduced allowing to improve the radiometric model fit with calibration results. This parameter is dependent on the spectral band k.
- $off_{i,g}^k$ is the offset which is both dependant on and varying in proportion with the average gain level
- A_T^k: is the absolute radiometric coefficient, indicating the sensitivity of the spectral band k. It is dependent on the detector temperature.
- AVG_g is the average gain level (average over all recorded pixels i). By definition, is set to 1 for the nominal gain setting, and best fitted by calibration for the other gain settings.
- NL_g^k is a non-linear function of DN, expressed in DN units (i.e. LSB counts). It can be expressed as a look-up table for each pixel i of each spectral band k and for gain g.
- $g_{i,g}^k$ is the equalisation coefficient and represents the pixel to pixel response variation due to the possible pixel to pixel gain variation, so $\bar{g}_g^k$, being the average of $g_{i,g}^k$ over all recorded pixels i, is by definition 1.

4.2.1.1   Temperature effect on dark current

The dark current is higly dependent on temperature following an exponential model :

$$dc_{i,g}^k(T) = dc_{i,g}^k(T_{reference}) . \exp\left[\frac{\Delta E_i^k}{k} \left(\frac{1}{T} - \frac{1}{T_{reference}} \right) \right]$$

Equation 1: Analytic relation dark current-temperature

with ΔE_i^k : the activation energy

Therefore, a LUT of dark current values will be available for calibration, based on the this formula. The reference temperature will be the temperature for which the most recent dark current value is known. The initial value will be the dark current registered pre-launch in lab conditions, these values will then be updated in-flight during the dark current calibration, using temperature measurements of thermistors available on the platform. Starting from the reference temperature existing during these measurements, the LUT with values at surrounding temperatures can be generated.

From the current thermal design analysis, it appears that the maximum change in temperature expected over one orbit is below 2 °C for the VNIR band, below 5°C for the SWIR band. Differences caused by temperature will thus have to be taken into account.

In addition, over the course of a year there is a seasonal effect that results in a temperature difference. Based on the Hot/Cold case analysis done by QS, a worst-case monthly variation of 1 to 1.5°C is expected. This seasonal difference implies the reference temperature will change over the time of year, and must be accounted for by updating the dark current information at regular time steps.

4.2.2 Inverse model

In calibration operations, the model has to be used in inverse direction, starting from DN data and working toward effective spectral radiance. In radiometric characterization approaches, three phases can be distinguished.

As a first phase, the acquired DN result must be corrected for nonlinearity and for the offset:

$$DN_i^k = DN_{i,acquired}^k - NL_g^k(DN_{i,acquired}^k) - off_{i,g}^k$$

The second phase is a correction for **dark current** (section 4.3.1). The objective here is to deduce and then subtract the dark signal offset -taking into account the integration time and integration time offset- and retrieve an intermediate DN result:

$$DN_{cor1,ig}^k = DN_i^k - dc_{i,g,T}^k \left(IT + dIT^k \right)$$

Equation 2: Dark current offset correction

In the third phase the current values for <A,g,.> are used to derive the effective spectral radiance result:

$$L_{TOA,i}^k = \frac{DN_{cor1,ig}^k}{A_T^k \cdot g_{i,g}^k \left(IT + dIT^k \right)}$$

Equation 3: Conversion to effective spectral radiance

These two equations can be put together to describe the relation between acquired DN data and effective spectral radiance:

$$L_{TOA,i}^k = \frac{DN_{i,acquired}^k - NL_g^k(DN_{i,acquired}^k) - off_{i,g}^k - dc_{i,g,T}^k\left(IT + dIT^k\right)}{A_T^k \cdot g_{i,g}^k\left(IT + dIT^k\right)}$$

Equation 4: Inverse sensor model relation

4.2.3 Operational dependencies

Each camera will be treated separately. Estimation of the different parameters in the sensor model is discussed in subsequent sections:

- dark current dc_i^k in section 4.3.1.
- absolute calibration coefficient A^k in sections 4.4, 4.5 , 0
- equalization coefficient g_i^k in section 4.8
- nonlinearity parameter NL is not estimated in-flight, but the linearity of the system after nonlinearity correction is verified by the process described in section 4.3.3.

4.3   Radiometric Characterization

4.3.1   Dark Current

4.3.1.1   Introduction

Dark current ($dc_{i,g}{}^{k}$) is caused by thermally generated electrons that build up in the pixels. The magnitude of the dark current is expected to increase with time due to space radiation. Moreover, as described in section 4.2.1.1, noticeable variations of dark current are expected over the course of the year as a result of temperature effects. It is therefore important to monitor the dark current in orbit.

Uncompressed images taken during the nighttime portion of the orbit of dark ocean sites (situated in Northern hemisphere in winter and Southern hemisphere during summer) will be used to determine the dark current values for all pixels.

Central assumption in the calibration is that the effective signal captured during the dark current calibration is much lower than the dark current itself. The effective signal of each pixel will then be composed mainly of its dark current signal, the associated dark current shot noise and the signal-independent read noise. The latter two contributions can be eliminated by taking the mean of the signal of each pixel over time.

4.3.1.2   Algorithm

Starting from the assumptions of the previous section, the steps to follow in this algorithm are:

- Select dark ocean sites (at night time) for which the effective signal **can be expected to be** sufficiently low. Sites have been selected and defined in the In-flight Characterization and Calibration Plan [PVDOC-615]. For these sites, L1B data is retrieved for regular overpasses of at least 500 lines.
- Remove saturated values[1] from further processing.
- Correct the acquired DN ($DN_{i,acquired}^{k}$) for Non-linearity and offset :

$$DN_i^k = DN_{i,acquired}^k - NL_g^k (DN_{i,acquired}^k) - off_{i,g}^k$$

- For each pixel, detect lines containing significant outliers. Significant line outliers are an indication of 'local events', either caused by an unwanted signal (such as moon glint) or unwanted behaviour of the instrument. Line outliers can be detected and removed by determining the median and median absolute deviation. This approach is discussed in 4.3.1.2.1.
- When line outliers are removed, for every pixel the average DN value is calculated over the remaining lines l: $dc_{i,g}^k = \left\langle DN_{i,g,l}^k \right\rangle_l$. The result is considered as the current value of dark current for this pixel and gain setting.

The time range corresponding to 500 lines is 7,5 s. Variations in temperature can be expected to be minimal over this time, and therefore an average temperature T_{ref} existing for the current calibration can be assumed. From this reference temperature the dark current at other temperatures can be derived using Equation 1.

For the optical band signals, all dark current values, not including saturated lines, can be considered reliable. For the SWIR signals however, a stronger influence of dark current and risk of radiative damage must be accounted for. This is done by performing a quality check procedure on the averaged pixel values (see 4.3.1.2.2). The result of this procedure is a set of dark current values for the qualified pixels, and a quality map allowing for four cases:

---

[1]A DN value is saturated when the value is equal to the maximum bit of the data.

- 'undefined': the pixel is saturated, and no value could be defined for it
- 'aberrant': value of the pixel is suspect, and no reliable value could be defined for it
- 'singular': value of the pixel is suspect, but a corrected value is defined by looking at neighbouring values
- 'good': the pixel's value is not suspect.

4.3.1.2.1 Line outlier detection

The concepts of median and median absolute deviation (MAD) are better suited to the detection of outliers than the mean value and standard deviation. The calculation is defined as:

$$MED_{i,g}^{k} = \text{median}(DN_{i,g,l}^{k})_l$$

$$MAD_{i,g}^{k} = \text{median}\left(\left|DN_{i,g,l}^{k} - MED_{i,g}^{k}\right|\right)_l$$

Equation 5: Median metrics for outlier detection

The MAD value can be made equivalent to a standard deviation of a distribution by multiplying with a constant K. In the assumption of a normal distribution, K=1.4826. Hence:

$$S_{MAD,i,g}^{k} = 1.4826\, MAD_{i,g}^{k}$$

Equation 6: Equivalent median-standard deviation for normal distributions

When the MAD value is zero, most values are close to the median. In this case no outliers are eliminated, since no additional information on the values differing from the median has been retrieved by the statistics.
For every non-zero value, the 2-sigma confidence interval is selected as the region of valid lines. Every other line is considered an outlier. The DN values therefore have to obey the following condition:

$$MED_{i,g}^{k} - 1.96\, S_{MAD,i,g}^{k} \leq DN_{i,g,l}^{k} \leq MED_{i,g}^{k} + 1.96\, S_{MAD,i,g}^{k}$$

Equation 7: 2-sigma confidence interval based on median-standard deviation

4.3.1.2.2 SWIR pixel quality check and pixel outlier correction

Pixel quality is checked and if possible and necessary corrected by comparing the difference in value between a pixel and its neighbours. To avoid the influence of saturated pixels in this calculation, a pixel mask *sat*(j) is defined such that *sat(j) = 1* when the pixel is saturated in all lines, and *sat(j) = 0* when the pixel is not saturated.
A status list is defined, containing a status value for all pixels. Possible status values are:
- *blank*: no value defined yet
- *undefined, aberrant, singular, good*: as described above.

All values from first pixel 1 to final pixel N_p are set to *blank* initially. At either edge, an extra value is given and set to *aberrant* to account for the fact that the edge pixels have only one neighbour they can compare to. In addition, the status of saturated pixels is set to *undefined*. These operations are illustrated in Figure 2.
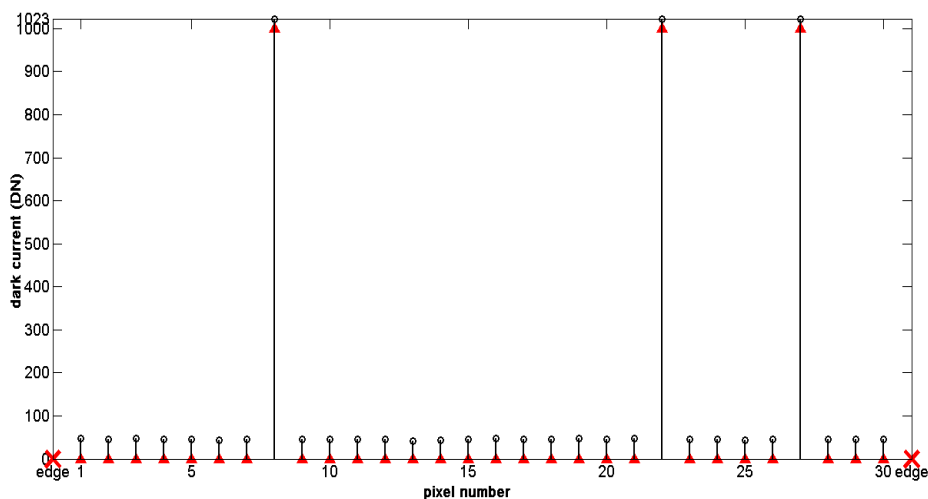
Figure 2: Initial quality status in red for 30 pixels.

Triangles at high levels represent 'undefined' status, triangles at low levels represent 'blank' status. The red crosses at either end represent 'aberrant' status for the extra edge values.

The quality status of pixels is derived from a statistical analysis of their averaged value (which is the metric of the dark current value for 'good' pixels). This can be motivated by observing Figure 3.
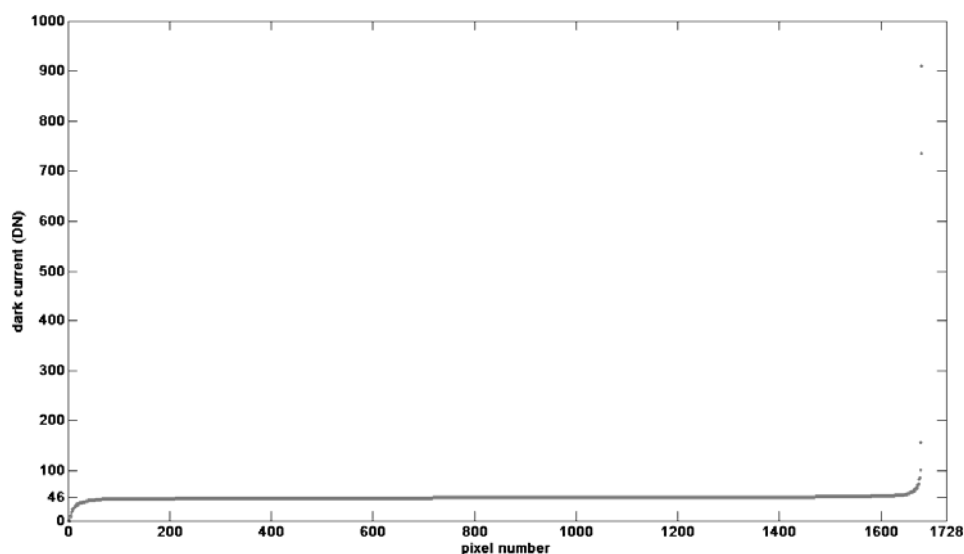
Figure 3: Dark current data for VGT-MIR data (from 512 lines)

This shows dark current data extracting from the CNES SPOT-VGT mission, for 512 lines of the MIR band (which corresponds spectrally to PROBA-V SWIR). The values are sorted from small to large. This shows that the large majority of pixels displays a very similar dark response, with a minor set of outliers found at either end of the signal range. A pixel's status can therefore be defined as 'good', 'singular' or 'aberrant' depending on its deviation from the mean value.

An 'aberrant' status is mainly seen at the higher signal end: these are associated with pixels showing a significantly different behaviour, and are therefore assumed to be impossible to correct. A 'good' status is associated with pixels who are very close to the mean. 'Singular' status is to describe intermediaries, which might be corrected by comparing with neighbouring values.

Two metrics are calculated as demarcations for these three categories. The MAD-standard deviation is again calculated, as a conservative measure to distinguish 'good' pixels from

'singular' ones. A less tight measure is the standard deviation: this is used to distinguish 'singular' pixels from 'aberrant' pixels. The demarcations are described as such:

$\left| dc_{i,g}^{k} - mean(dc_{i,g}^{k})_{i} \right|$	Status
$... \leq 1.96\ \sigma_{MAD,g}^{SWIR}$	good
$1.96\ \sigma_{MAD,g}^{SWIR} < ... \leq 1.96\ \sigma_{std,g}^{SWIR}$	singular
$... > 1.96\ \sigma_{std,g}^{SWIR}$	aberrant

Table 4: Pixel quality calculation

Once the quality of all pixels is assessed, a correction can be performed for every singular pixel. This is done by checking the status of its neighbours. If one of its neighbours is 'good', it is assumed that the same dark current is present in both pixels. If not, then the 'singular' value is not corrected.

4.3.2　Detection of defective and degraded pixels

4.3.2.1　Introduction

Defective pixels can either be stuck pixels (which exhibit consistently a lower or higher bias of charge) or they can have a gain reduction, deviating to such an extent that a calibration by equalization is no longer possible for these pixels. Defects can develop from radiation damage in-flight or unexpected malfunctioning, and therefore the status of every pixel needs to be assessed continuously in-flight. Aside from a supervised evaluation on uniform sites done at the IQC at a regular basis (the regularity of which is to be decided during the commissioning phase), an automatic method of correction is available in the PF [PVDOC-624]. This method allows the PF to catch new defects in a fast way, without having to rely on an update of the pixel statuses by the IQC. This will only be implemented in the PF if the amount and frequency of detected defects is too much to rely on supervised evaluation alone.

During the commissioning phase, the supervised evaluation of pixel quality is intensely investigated to gain confidence that the followed procedure maintains control and overview of quality status of every pixel. The investigation proceeds according to several phases which are described in sections 4.3.2.2.3-4.3.2.2.6. When the investigation is complete, the nominal supervised evaluation is set as fixed for the nominal operations.

4.3.2.2　IQC evaluation activities

The evaluation focuses on the imaging of uniform sites, as is done in other calibration activities. Strong deviations from a uniform signal are then expected to be caused by the pixel's behaviour only, therefore allowing aberrant behaviour to be detected more easily.

Because of radiometric noise effects, a good grasp of a pixel's systematic behaviour can only be done when averaging out the pixel's signal over a sufficient amount of lines. However, one must be cautious for unexpected 'local' events unrelated to pixel defects. These events can be avoided by detecting outliers. This process is described in 4.3.2.2.1.

During commissioning, the development of the defective pixels evaluation proceeds according to several phases. In the first phase, detections are performed for each uniform site separately. This allows to detect bias deviations specific for a site (deviations of averaged pixel signals from the averaged signal of that uniform site). The detection results can be compared across different sites and sites can thus be validated. This process is described in section 4.3.2.2.3.

After validation, different sites are integrated into one detection system. The goal is here is to combine information from different sites, and deliver one output. This is described in section 4.3.2.2.4.

At this point, several pixels can still be flagged as suspect. This might be because of defects not explainable as a strong bias effect. A gain method is then used as an additional detection strategy. This is discussed in section 4.3.2.2.5.

Finally, the final combination of all relevant sites and methods is integrated, and fixed as the final IQC evaluation process. As data of relevant sites are also used by other calibration methods, these relations are briefly discussed. This is done in section 4.3.2.2.6.

4.3.2.2.1 Line outlier detection & averaging

The goal of line outlier detection is to detect temporary deviations of a pixel's signal that are not typical for that pixel. Causes for this are unexpected events, such as clouds, a local reflection (sun glint, moon glint), or radiative collision. Radiative collision are possible causes for permanent defects, but can also temporarily influence the pixel's signal; only the latter is considered a line outlier.

Obvious line outliers are saturated values. These are removed from further processing. Note that by removing saturated values, it could be possible that the remaining lines are too few to be reliable for averaging. A number of unsaturated lines (default = 200) is required at minimum, if this is not the case, the pixel status calculation is considered as failed and the pixel is flagged as 'suspect'(see 4.3.2.2.2). If all lines are consistently saturated , for a site containing at least a minimum number of lines for this pixel (default = 200), this is considered a saturated line and the pixel is flagged as 'bad'.

Next, the acquired DN ($DN^k_{i,acquired}$) for Non-linearity and offset :

$$DN^k_i = DN^k_{i,acquired} - NL^k_g(DN^k_{i,acquired}) - off^k_{i,g}$$

Further line outliers are detected as deviations from the mean signal. This approach is similar to that in section 4.3.1.2.1 and Equation 7:

$$MED^k_{ig} - 1.96 \ S^k_{MAD,i,g} \le DN^k_{i,g,l} \le MED^k_{i,g} + 1.96 \ S^k_{MAD,i,g}$$

In this case however, it is not optimal to use the concept of median deviation(MAD), because a defective pixel can have a lot of erratic lines, but still have a good mean and median[2]. Therefore, the MAD is replaced by a standard deviation figure, and the median by the mean figure:

$$\mu^k_{i,g} - 1.96 \ \sigma^k_{STD,i,g} \le DN^k_{i,g,l} \le \mu^k_{i,g} + 1.96 \ \sigma^k_{STD,i,g}$$

When $\sigma^k_{STD,i,g}$ is significantly larger than the average noise value for other pixels, the pixel status calculation is considered as failed and the pixel is flagged as 'bad' (see 4.3.2.2.2).

The averaged pixel value is then calculated by averaging over the remaining lines:

$$DN^k_{i,g,mean} = \left\langle DN^k_{i,g,l} \right\rangle_l$$

4.3.2.2.2 Pixel status definitions

Three statuses are distinguished:
- 'good' : pixels are qualified as good when their behaviour is identified as normal

---

[2] Example: Take as reference of a good pixel, one with values averaged around 1000DN, and some small noise (values of 1005, 994, 1002,..). A bad pixel is then the following: an average of 1000DN, with 200 lines at value 100 and 800lines at 1225. This behavior is bad, considering that the imaged site is supposedly uniform, and should not return values of 100 at one time, 800 at another. Still, the MAD figure will be small, because the erratic behavior of the 200 lines will not be detected.

- 'bad' : pixels are qualified as aberrant when their behaviour is defective, not normal
- 'suspect' : pixels are qualified as suspect when their behaviour has been impossible to identify. When a quality detection has failed or was impossible to determine, a pixel is qualified as suspect.

4.3.2.2.3   Bias methods validation phase

In this phase, evaluation is first done for each site separately. Every site can be associated with a nominal signal level. The assumption is that this signal level will be located somewhere around the median level: $DN_{site,g,mean}^k = median\left(DN_{i,g,mean}^k\right)_i$.

Defective pixels are assumed to deviate significantly from this nominal level, similar to the discussion in 4.3.1.2.2. From the perspective of bad pixel detection however, a pixel is only flagged as 'bad' when a clear distinction can be made. When unsure about a pixel's behaviour, it will be flagged as 'suspect'. Hence, it is more likely that in this phase, a lot of pixels will be flagged 'suspect' instead of 'bad'.

When all sites have been evaluated, a pixel status list is available for each of them. These status lists are cross-validated as follows:
- if a pixel is flagged as 'bad' in one site, and is flagged as 'bad' or 'suspect' in all other sites of a later date, it is considered as 'bad' over all these sites. Thus, one indication is good for all.
- however, if a pixel is flagged as 'bad' in one site, and is flagged as 'good' in a site at a later date, this indicates a misdetection. The method is then invalidated, and the evaluation is re-checked manually for this pixel.
- if a pixel is flagged as 'suspect' in one site, and is flagged 'suspect' or 'good' in all other sites (of a later date), it is considered as 'suspect' over all these sites.
- if a pixel is flagged as 'good' for all sites, it is considered a good pixel and does not undergo further processing.

4.3.2.2.4   Bias methods integration phase

When the validation phase is finished, a final result for the pixel status list is achieved. It is then checked if the information of some sites can be considered redundant wrt others. This is checked as follows:
- when one site allows for all detections of suspect or aberrant pixels as another site, and allows for more detections still, then this site is superior and the other site is removed from the evaluation list.

When all sites have been checked in this manner and redundant sites have been removed, the remaining sites are then integrated in one system. This system is then tested with new data: if the system produces the same pixel status list result for 10 subsequent trials as the full list of sites, the system is considered validated. It is expected no further trials are necessary, considering the validation is done over all pixels.

4.3.2.2.5   Gain method phase

In the gain method, only the pixels flagged as 'suspect' are still under evaluation.
When moving to the gain method, averaged pixel values from different sites need to be compared. Since the site data is possibly captured under different imaging conditions, this needs to be compensated for first. Hence, the differences are rescaled with the nominal site value as

defined above : $DN_{i,scaled,mean}^k = \dfrac{DN_{i,g,mean}^k}{DN_{site,g,mean}^k}$.

When the gain is defective, the value for higher signals (ie. brighter sites or sites with stronger gain) deviates more from the nominal value than the value for lower signals does. Therefore, the detection algorithm proceeds as follows:
- sort site values from low to high values
- calculate for each site the deviation of pixel values from nominal values:

$$\Delta DN_{i,site}^{k} = DN_{i,scaled,mean}^{k} - 1$$

- when this deviation increases significantly for high values, the pixel is flagged as 'bad'. If it doesn't, no further indication of a defect is possible, and the pixel status remains 'suspect'.

4.3.2.2.6 Full evaluation phase

When all methods are finished, the full chain of methods is evaluated. As the goal of the defect detection is to flag pixels either as 'bad' or 'good', the pixels still flagged as 'suspect' at this stage are held under scrutiny. When it is assured that no better conclusion can be made based on the existing data, the pixel's flag is set to 'good'. This is the only acceptable conclusion: for the time being no defective behaviour can be observed in the pixel. As a final output, a pixel quality map is therefore made showing pixels either as 'good' or 'bad'.

In the full evaluation phase, the defect detection procedure can be considered to be finalized. Some further comments need to be made then:

- when a pixel is flagged as 'bad' in the final procedure, it is considered defect for all further dates. Therefore, it makes no sense to re-investigate its state in a later detection procedure. The pixel quality map is therefore handled as an input to eliminate 'bad' pixels at the start of the procedure
- also, the uniform site data used in the procedure is likely to be used by other calibration operations as well. The dependencies between these must be clearly defined.
- Finally, the statistics used in the detection methods are controlled by thresholding values which can be controlled by the user. These, together with the finalized pixel status list, should be transparent to the calibration manager. Table 5 shows a full list of the thresholding values.

Parameters	Used in:		
	Line outlier detection	Bias deviation calculation	Gain deviation calculation
REQ_LINES	single value		
$\sigma_{STD,threshold}^{k}$	value per band		
$DEV_{site,threshold\_low}^{k}$		value per band and site	
$DEV_{site,threshold\_high}^{k}$		value per band and site	
DEV_{LO}		single value	
DEV_{HI}		single value	
$GDEV_{threshold}^{k}$			value per band

Table 5: Thresholding values for defect detection

4.3.2.3 PF automatic operations

An automatic pixel detection method is available in the PF for the analysis of SWIR pixels. A SWIR sensor tends to be quite sensitive to radiation. For this reason, the PF processing might be disadvantaged if it must wait for an update of IQC calibration files before knowing which pixels have become defective since the previous calibration file update. A quick automatic pixel

detection allows the PF to assess obvious cases of new bad pixels independently before the arrival of new IQC calibration files.

The PF detection method is based on the study of signal stability, and of nearest neighbour deviations. Signal stability is first checked: when the signal of a pixel is very unstable over a certain number of lines, it is considered as an aberrant pixel. Stable signals are then averaged, to assess the average value of a pixel. These are then checked with nearest neighbours, according to a voting strategy. Very high deviations are a mark of aberrant behaviour, significant but not so high deviations are still considered as a correctable offset (similar to a dark current). The full motivation of this method is described in [PVDOC-624].

4.3.3 Linearity Check

4.3.3.1 Introduction

The measurement of the linearity of the relation between effective spectral radiance and digital output is crucial, as systematic deviations from this linearity are able to happen when in-flight. Possible causes of this are:

- saturation of the sensor because of surface full well (interface traps capturing electrons)
- saturation of the electronics because of voltage cut off, when an input has a higher voltage than the maximum voltage corresponding to the maximum bit being registered.

A reliable method of measuring linearity is by changing the integration time, while imaging a stable light source. In the assumption that the input is stable and integration time always has a linear relationship, the dynamic range can be explored by collecting more or less signal in varying the integration time. This process is illustrated in Figure 4.
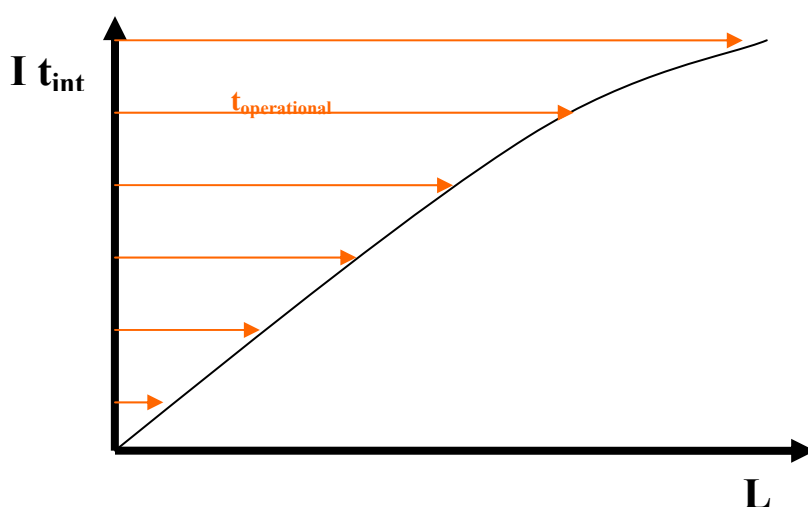
Figure 4: Measurement of linearity, by varying integration time.

The incoming radiance generates a current which is collected during the configured integration time. At large integration times, more charge is collected, and saturation defects are more likely to occur. By varying integration time, it can be assessed at which integration time (and thus, at which collected charge) saturation defects become significant. An integration time setting that is used operationally **must** be below this threshold integration time. If not, the response is nonlinear, without the sensor model being able to correct for it.

In the context of vicarious calibration, by a stable light source is meant a uniform calibration zone. The signal magnitude over this zone should be low enough to be still able to measure the response at the range of integration times to be tested (if signal magnitude is too high, saturation will be reached too soon). Ideal candidates for these zones are the desert zones that are used for multi-temporal calibration operations (see section 4.5.3).

4.3.3.2 Algorithm

4.3.3.2.1 Establish radiance outputs

input:
- Images captured over deserts with a set of integration times, spread over the dynamic range of the instrument for different bands: (set TBD).
- Sensor model parameters: A, g, dc. All the parameter sets for the bands, pixels, temperatures, gain numbers under investigation need to be defined.

procedure:
- For each of the image points, remove all lines that are outliers, and determine the average result over each different integration time set for each pixel using the procedure described in section 4.3.2.2.1.
- Derive the effective spectral radiance **L** for each of the image points and associated parameter sets, using Equation 4.
- For each of the image points, collect the L values for the different integration time sets. If the linearity degrades, the values will show a similar behaviour as depicted in Figure 5. A more clear distinction can be made when the values are multiplied with their respective integration time, so values **L x t_{int}** are investigated in function of **t_{int}**.
- Apply linear regression to the ensemble of data points. If no significant regression error is obtained, the entire ensemble is in the linear regime. If a significant error is obtained, proceed to the next step.
- Apply linear spline fitting to the ensemble of data points. It is expected that two or three regions will be found: one regime describing nominal levels, one regime describing saturation, one (optional) regime describing low level deviations.
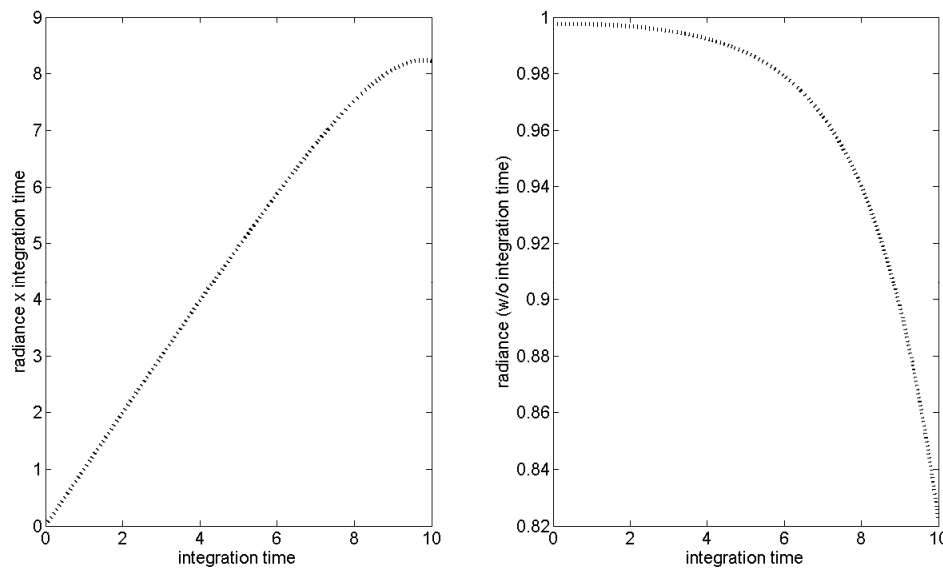

Figure 5: Illustration of linearity degradation.

output:
- The regression error corresponding to the linear or linear spline model that is obtained.
- If not sufficiently linear, the coefficients of the linear spline are also provided.

4.4   Absolute radiometric calibration

4.4.1   Rayleigh calibration: oceans

4.4.1.1   Introduction

The aim of the so-called Rayleigh calibration is to determine the absolute calibration coefficient A^k for the BLUE and RED bands. This method has been successfully applied to other sensors (POLDER, PARASOL, SPOT/VEGETATION, MERIS,…) and detailed descriptions exist in the literature (Vermote et al., 1992 [LIT2]; Hagolle et al., 1999 [LIT3]; Fournie et al., 2007 [LIT4]; Martiny et al., 2005 [LIT5]).

The at-sensor radiance at short wavelengths over dark deep oceans under large solar and viewing angles comes mainly from Rayleigh scattering (scattering by air molecules). Rayleigh or molecular scattering can accurately be calculated based on the surface pressure and viewing angles. The contribution of aerosol scattering (more specifically the aerosol optical thickness (AOT), can be derived from the NIR reference band where molecular scattering is very low (due to the strong wavelength dependence of Rayleigh scattering of λ^{-4}). The aerosol content estimated from the NIR band is then transferred to the BLUE and RED band to model the TOA radiance with a radiative transfer software module (6SV, [LIT6]). The simulated radiance values are then compared with the measured values to derive the absolute calibration coefficient.

To reduce the perturbing part of the signal due to ocean reflectance and presence of foam, strict pixel selection procedures are used. Pixels can only be chosen within oligotrophic areas with well known weak and stable chlorophyll content. To minimize foam radiance meteorological data are used to select zones with low wind speed. Finally only pixels outside sun glint direction are used.

The Rayleigh calibration approach allows for absolute calibration of the BLUE, and RED bands taken the NIR band as reference band. The method cannot be applied to the SWIR band. The results can be transferred to other bands (NIR, SWIR) based on inter-band calibration approaches as sun glint (for both NIR and SWIR) or clouds (NIR) as described in section 4.5.1 and 4.5.2 respectively.

4.4.1.2   Algorithm

4.4.1.2.1   Physics of the algorithm

4.4.1.2.1.1   Conversion of TOA radiance to TOA reflectance

Following the inverse sensor model relation (Equation 4), the radiance L_{TOA}^k at the TOA for pixel i is derived from the measured digital number DN.

L_{TOA}^k is then normalized by the exo-atmospheric solar incident flux in order to obtain the TOA reflectance ρ_{TOA}^k:

$$\rho_{TOA}^k = \frac{\pi L_{TOA}^k}{E_0^k \cos(\theta_s)\left(\frac{d_0}{d}\right)^2}$$

Equation 8: Conversion of TOA radiance to TOA reflectance

with

E_0^k is the mean extra-terrestrial solar irradiance (CEOS recommended irradiance file : Thuillier ,2003 [LIT7]) integrated over the spectral response of the different PROBA-V spectral bands ($S_k(\lambda)$) as

$$E_0^k = \frac{\int_0^\infty S_k(\lambda)E_0(\lambda)d\lambda}{\int_0^\infty S_k(\lambda)d\lambda}$$

θ_s is the solar zenith angle

d_0 / d is the ratio of Sun-Earth distance at the acquisition date to the mean Sun-Earth distance, calculated based on the Julian day according to the formula in the 6SV subroutine varsol.

4.4.1.2.1.2 TOA reflectance signal decomposition

Over oceans the TOA reflectance ρ_{TOA} (outside strong oxygen and water vapour absorption bands) can be decomposed as (omitting spectral band index and angles for simplicity):

$$\rho_{TOA} \approx Tr_{gas}\left[\rho_{path} + \frac{\rho_w Tr_{tot,s} Tr_{tot,v}}{(1 - s\rho_w)}\right]$$

Equation 9:TOA reflectance decomposition

with

ρ_w	the water leaving reflectance
$Tr_{tot,s}$, $Tr_{tot,v}$	the total atmospheric transmittance for aerosols and molecules (sum of direct and diffuse components) respectively for the solar and viewing zenith angles
s	spherical albedo of the atmosphere
Tr_{gas}	the total gaseous transmittance (assumed to be decoupled from the scattering)
ρ_{path}	the path reflectance due to molecular and aerosol scattering in the atmosphere, including coupling terms and the specular reflection by the wavy surface

We ignore here the surface foam reflectance, which is negligible for surface wind speeds under 10 m/s (wind speed mask applied in processing). The specular reflection of direct sun light or the sun glint reflectance is also ignored as for Rayleigh calibration only pixels outside sun glint direction are used (glitter mask applied in processing).

The path reflectance ρ_{path} can be decomposed into the following components :

$$\rho_{path} = \rho_m + \rho_{gm} + \rho_a + \rho_{ga}$$

Equation 10: Path reflectance decomposition

with

ρ_m	reflectance due to multiple scattering of air molecules (Rayleigh reflectance) in absence of aerosols
ρ_{gm}	reflectance due to specular reflection at the rough sea surface of the light scattering by the molecules in the atmosphere
ρ_a	reflectance due to multiple scattering by aerosols and by combined successive scattering by molecules and aerosols; This term is computed as $\rho_a = \rho_{a+m} - \rho_m$.

ρ_{ga}		reflectance due to specular reflection at the rough sea surface of the
and		light scattering by combined successive scattering by molecules aerosols

Because the Fresnel surface reflectivities are small, the additional path reflectance terms ρ_{gm} and ρ_{ga} are smaller than the direct path reflectance terms (ρ_m, ρ_a). Because wind speed alters the magnitude of the reflected radiance, ρ_{gm} and ρ_{ga} depend on the wind speed.

The water leaving reflectance in the near infrared (NIR) wavelength region is generally equal to zero for dark oceanic waters Gordon and Wang (1994) [LIT8] due to the strong seawater absorption. This is the so called black pixel assumption. Therefore the equation for the TOA reflectance (Equation 9) for the NIR band can be simplified as

$$\rho_{TOA}(NIR) \approx Tr_{gas}(NIR)\rho_{path}(NIR)$$

Equation 11: NIR TOA reflectance simplified decomposition

In Figure 6 the preliminary spectral response curves of PROBA-V bands are given with respect to the major gaseous absorption bands. These figures indicate that gaseous transmittance in the PROBA-V NIR band is (slightly) contaminated by water vapour. For dark surfaces like oceans we can however not fully decouple water vapour absorption and scattering (Martiny et al, 2005 [LIT5]) because aerosol and water vapour can be located at the same level in the atmosphere. As information on the relative scale height of the water vapour and of the aerosols is generally not available, we will adopt the scheme given by Vermote et al. [LIT6] in the 6SV manual. This scheme assumes that the aerosol path radiance is generated above the middle of the boundary layer. Thus the additional attenuation is made by half the precipitable water:

$$\rho_{TOA}(NIR) \approx Tr(O_3,O_2,M)\left[\rho_m + Tr^{H_2O}\left(M,\frac{U_{H_2O}}{2}\right)\rho_a + Tr^{H_2O}\left(M,U_{H_2O}\right)\left(\rho_{gm} + \rho_{ga}\right)\right]$$

with

M	the air mass given by $M = \dfrac{1}{\cos(\theta_s)} + \dfrac{1}{\cos(\theta_v)}$
$Tr(O_3,O_2,M)$	the gaseous transmittance of O_3,O_2
Tr^{H_2O}	the water vapour transmittance.
U_{H_2O}	the total precipitable water in units of g/cm²

The TOA apparent reflectance corrected for the gaseous transmittance of O_3,O_2 will be denoted as :

$$\rho^c_{TOA} = \frac{\rho_{TOA}}{Tr(O_3,O_2,M)}$$

Equation 12: Correction of TOA reflectance for gaseous (Ozone, Oxygen) absorption
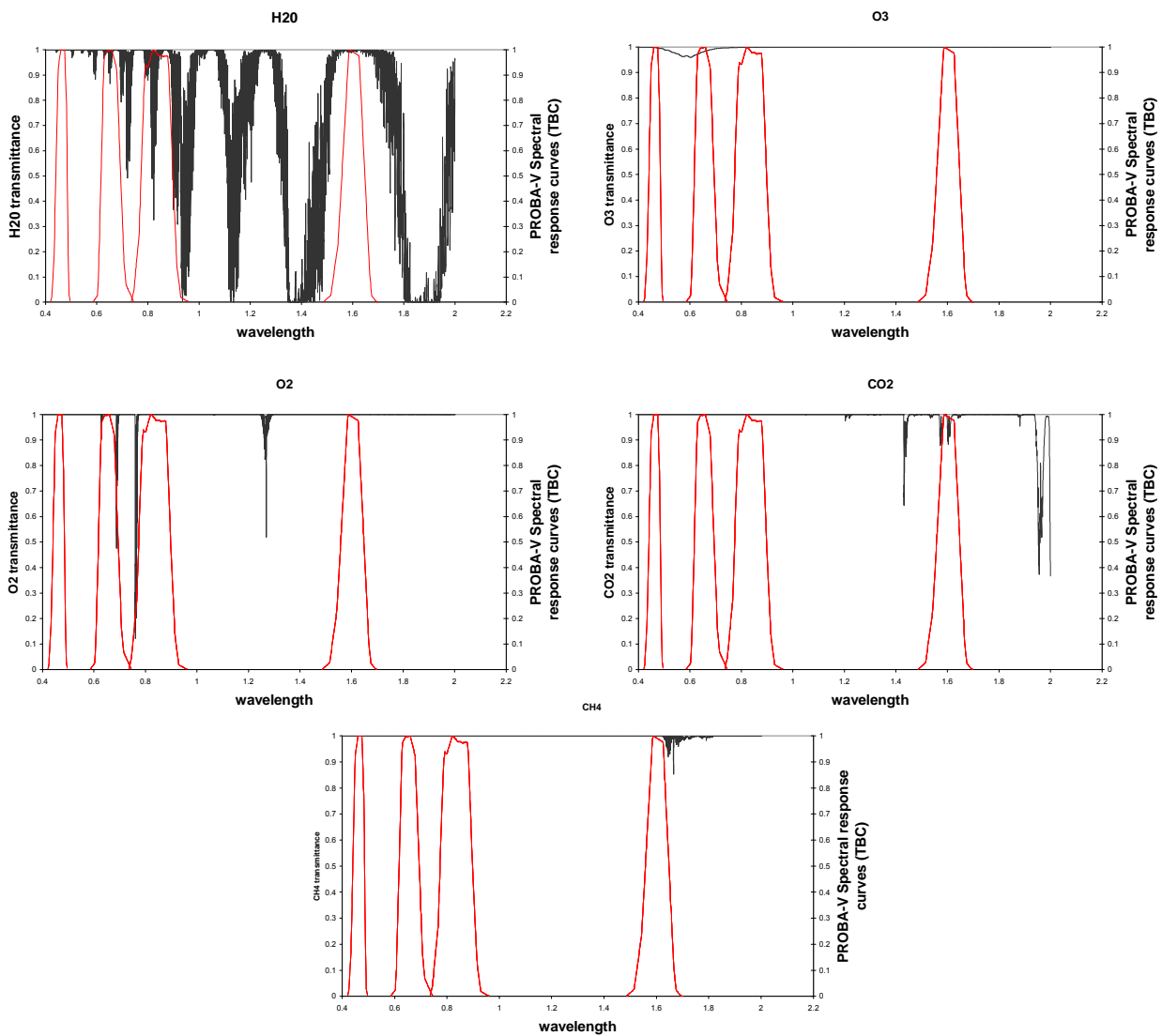
Figure 6: Gaseous absorption in PROBA-V bands

4.4.1.2.1.3   Retrieval of the aerosol optical thickness (AOT) from NIR band

The gaseous transmittance and molecular scattering can be calculated with 6SV based on the available ancillary data (surface pressure, amount of ozone and total precipitable water, wind speed). 6SV includes polarization and specular reflection by the wavy surface. The only unknown in Equation 11 is the aerosol scattering contribution, which depends on the aerosol optical thickness (AOT) and the aerosol model.

The aerosol model adopted for the 6SV calculations is the Shettle and Fenn Maritime aerosol model with 98% humidity (denoted as M98) (Shettle and Fenn, 1979 [LIT9]). Following Hagolle *et al.* (1999) [LIT3] highest accuracies can be achieved with the M98 model (errors due to deviation from M98 are taken into account in the error budget). The maritime aerosol model has two components (a) a sea-salt component and (b) a continental component which is assumed to be identical to the rural aerosol with the exception that very large particles were eliminated. The M98 aerosol model can be introduced in 6SV by specifying the particle size distribution of each component of the aerosol model, represented by a log normal distribution function. Tables with individual component refractive indices (real and imaginary) in function of humidity versus wavelength are given in the report by Shettle and Fenn (1979) [LIT9].

The aerosol optical thickness (AOT) is however not *a priori* known and will be derived from the NIR band. The primary assumption of Gordon and Wang (1994) [LIT8] is that the ocean (i.e. the water leaving reflectance) does not contribute to the TOA signal in the NIR, (i.e., all radiance reaching the sensor is of atmospheric origin (including fresnel reflection on the ocean

surface)). Using this assumption, the NIR bands can then be employed for the aerosol determination in the calibration process. This assumption holds for Case 1 waters with low chlorophyll concentration and where phytoplankton is the only optically significant water column contributor.

The AOT per pixel is retrieved from the NIR band based on a LUT. This LUT contains modelled $\rho_{TOA}^{c,\text{mod}el}(NIR)$ in function of geometrical parameters, pressure, water vapour, wind speed and AOT. The LUT of simulated/modelled $\rho_{TOA}^{c,\text{mod}el}(NIR)$ are interpolated (on the angles, water vapor, windspeed, pressure of each pixel) to obtain a LUT of $\rho_{TOA}^{c,\text{mod}el,NIR}$ in function of only AOT. The AOT value for which the measured $\rho_{TOA}^{c,meas}(NIR)$ fits best with the modelled $\rho_{TOA}^{c,\text{mod}el}(NIR)$ is searched for.

4.4.1.2.1.4   Retrieval of the calibration coefficients for the BLUE and RED bands

Once the AOT is determined $\rho_{TOA}^{c,\text{mod}el}(RED)$ and $\rho_{TOA}^{c,\text{mod}el}(BLUE)$ can be calculated according to Equation 9 with the radiative transfer model 6SV. The water leaving reflectance in 6SV is calculated using the semi-analytical reflectance model described in Morel, 1988 [LIT10]. This model is based on the bulk diffuse attenuation coefficient or downward irradiance $Kd(\lambda)$. On average this coefficient depends on the chlorophyll content (CHL) in Case1 waters, according to

$$Kd(\lambda) = Kw(\lambda) + \chi(\lambda)CHL^{e(\lambda)}.$$

Where $Kw(\lambda)$ corresponds to the contribution of pure water to $Kd(\lambda)$; the coefficient $\chi(\lambda)$ and exponent $e(\lambda)$ are tabulated values obtained through regression analysis performed on $Kd(\lambda) - Kw(\lambda)$ and CHL quantities in Case 1 waters. The equation accounts implicitly for coloured dissolved organic matter (CDOM) associated and co-varying with the CHL concentration in Case 1 waters. The $Kd(\lambda)$ are transformed in water leaving reflectance ρ_w in an iterative way. The water leaving reflectance ρ_w in Equation 9 is therefore a function of the CHL the chlorophyll content.

The Rayleight calibration is based on pre-defined oligotrophic waters with low and very stable chlorophyll concentrations. The calibration zones (Table 6) are taken from Fougnie et al.,2002 [LIT11] who selected these zones based on stability and uniformity criteria during two years (1998, 1999) of SeaWIFS level 3 products.

Name	Min. latitude (deg)	Max. latitude (deg)	Min. longitude (deg)	Max. longitude (deg)
South of Atlantic	-19.9	-9.9	-32.5	-11
South of Indian	-29.9	-21.2	89.5	100.1
North of Atlantic	17	27	-62.5	-44.2
North of Pacific	15	23.5	179.4	200.6
North west of Pacific	10	22.7	139.5	165.6
South-East of Pacific	-44.9	-20.7	-130.2	-89

Table 6: Stable oligotrophic oceanic sites

In the recent studies by Fougnie et al. (2010) [LIT56] the monthly variation of marine reflectance for the defined calibration zones is analyzed on the basis of 9 years of SEAWIFS data. A similar study has been performed by Morel et al (2010)[LIT54]. In this latter study, the monthly averaged CHL and $CDOM$ concentrations for six selected oligotrophic areas (similar to or located within the zones listed in Table 6) are reported. As shown in Figure 7 notable difference in the seasonal variation of CHL occur. The seasonal variation is less pronounced and featureless in the North-West of Pacific and in the The North Pacific gyre. For this latter the highest annual mean CHL (0.059 mg m^{-3}) are observed. The seasonal CHL pattern for the other 4 oligotrophic zones are comparable and rather reproducible from year to year with peaks occurring around July-August.
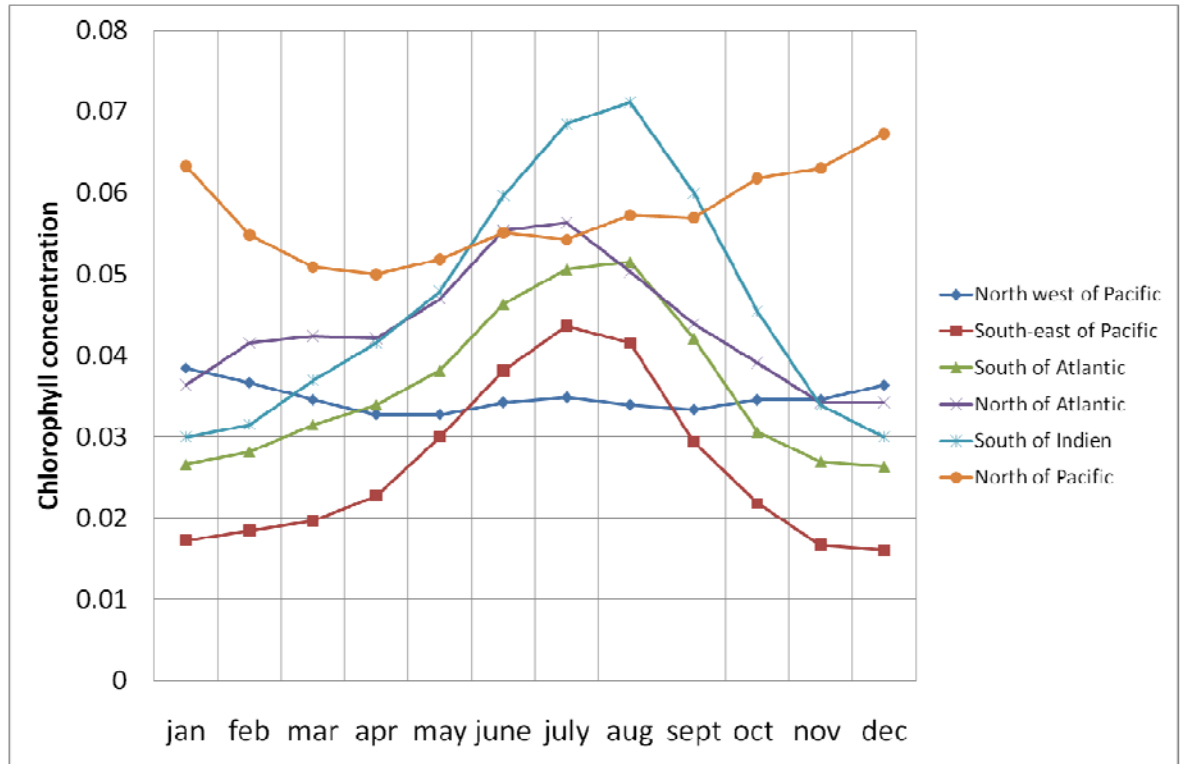
Figure 7: Monthly averaged chlorophyll (in mg m^{-3}) for each Rayleigh calibration zone

To model $\rho_{TOA}^{c,\mathrm{model}}(RED)$ and $\rho_{TOA}^{c,\mathrm{model}}(BLUE)$ with 6SV the montly varying and site-depended *CHL* values as given in Figure 7 are used. The coefficient   and exponent   ) are replaced with the slightly modified values from Morel et al (2007) [LIT55].

The Morel (1988) [LIT10] semi-analytical model used in 6SV implicitly includes a "mean" relationship between *CHL* and *CDOM*. In recent studies by Morel et al (2010) [LIT56]and Morel and Gentili (2009)[LIT53] deviations from these mean relationship has been observed and studies for the different oligotrophic zones. To account for these difference in the Morel (1988) [LIT10] semi-analytical model, the model could be operated with geographically distinct   values if avalaible for these zones (at this moment only published for the South Pacific).

The evaluation of the calibration coefficients consists in comparing $\rho_{TOA}^{c,\mathrm{model}}(RED)$ and $\rho_{TOA}^{c,\mathrm{model}}(BLUE)$ computed with the radiative transfer model 6SV (model) with $\rho_{TOA}^{c,meas}(RED)$ and $\rho_{TOA}^{c,meas}(BLUE)$ derived from the PROBA-V sensor measurements (meas), assuming a given (old) calibration (the one we want to evaluate).

Consequently, the ratio ΛA^{k}, relative change in calibration coefficients, defined as:

$$\Lambda A^{RED} = \frac{A_{RED}^{new}}{A_{RED}^{old}} = \frac{\rho_{TOA}^{c,meas}(RED)}{\rho_{TOA}^{c,\mathrm{model}}(RED)} \quad \text{and} \quad \Lambda A^{BLUE} = \frac{A_{BLUE}^{new}}{A_{BLUE}^{old}} = \frac{\rho_{TOA}^{c,meas}(BLUE)}{\rho_{TOA}^{c,\mathrm{model}}(BLUE)}$$

provides a measure of the difference in calibration coefficients with respect to the reference values (old). This ratio will be determined for each selected pixel. In section 0 it is explained how these individual estimates of A^{new} from the different pixels, sites and acquisition days will be statistically analyzed to define the final A^{new}.

4.4.1.2.2   **Algorithm implementation**

4.4.1.2.2.1 Generation of LUTs

As it is computationally prohibitive to run a radiative transfer model for every pixel of all the Rayleigh calibration images, a LUT approach will be used. The LUT will be created using 6SV (Vermote, 2008 [LIT6]) simulations. As its scalar predecessors, the vector version of 6S is based on the method of successive orders of scattering (SOS). The effects of polarization are taken into account in the vector version. Accounting for radiation polarization is extremely important for radiative transfer calculations over dark targets such as ocean surfaces. Ignoring the effects of polarization leads to large errors in calculated top-of-atmosphere reflectances: more than *10%* for a molecular atmosphere and up to *5%* for an aerosol atmosphere (Kotchenova et al., 2007 [LIT12]).

For the NIR band a LUT will be created for apparent TOA reflectance, corrected for gaseous transmittance of O_3, O_2 for an atmosphere bounded by black (ρ_w=0) fresnel reflecting wind roughened oceanic surface. This LUT will be a function of sun zenith angle, view zenith angle, relative azimuth angle, wind speed, pressure, water vapour and AOT.

Often LUTs are only calculated for standard atmospheric pressure of 1013.25 hPa and correction for atmospheric pressure variation are performed using the empirically retrieved formula from Gordon et al. (1988) (LIT13). Wang (2005) [LIT14] has however showed that this approach result in an extra uncertainty, especially in the blue. To improve the performance of the Rayleigh calibration approach we will use the Rayleigh solution of the radiative transfer calculations as done with 6SV. The effect of surface pressure variation can be exactly calculated with 6SV by changing $P(z)$ in the atmospheric profile (Kotchenova, private communication, July 2009).

For the BLUE and RED bands also LUTs are created for the apparent TOA reflectance, corrected for gaseous transmittance of O_3, O_2 for an atmosphere bounded by fresnel reflecting wind roughened oceanic surface with a chlorophyll concentration taken from
 in function of the month and site. These LUTs are a function of sun zenith angle, view zenith angle, relative azimuth angle, wind speed, pressure, water vapor and AOT.

For the generation of the LUTs with 6SV two options are considered: (a) a global pre-calculated LUT and (b) an *on-the-fly* calculated LUT. The global LUT will be valid for all imagery and will contain ρ_{TOA}^c for a variety of sun-view geometries, AOTs, pressures, water vapor concentrations and wind speeds within certain ranges. The *on-the-fly* calculated LUT is much smaller and only valid for the image under consideration. The ranges of the parameters are constrained by the ancillary image and meteorological data.

4.4.1.2.2.2 Processing on the PROBA-V calibration imagery

⇨ **Conversion to ρ_{TOA}^{meas}:** The input DNs for all image pixels are converted to TOA reflectance ρ_{TOA}^k following Equation 4 and Equation 8.

⇨ **Clear pixel selection :** Only pixels at a distance of at least 30 km from clouds will be kept, by extending the standard cloud mask. Furthermore only pixels for which the retrieved AOT in the NIR band is less than 0.05 will be selected in order to reject data with sensible aerosol loading.

⇨ **Masking white caps :** To avoid contamination by white caps or foam only pixels for which the wind speed (from the meteorological data) is smaller than 5 m/s will be kept.

⇨ **Masking pixels probably affected by sun glint :** To avoid sun glint only pixels with $\theta_n > 20°$ are selected:

$$\theta_n = ar\cos\left(\frac{\cos\theta_s + \cos\theta_v}{2\cos\left(\dfrac{\theta_p}{2}\right)}\right) \text{ with } \theta_p = ar\cos(\cos\theta_s\cos\theta_v + \sin\theta_s\sin\theta_v\cos\phi)$$

⇨ **Correction for gaseous absorption of ozone and oxygen; conversion from ρ_{TOA}^{meas} to $\rho_{TOA}^{c,meas}$:**
The correction is made using a pre-calculated exponential variation with air mass and gaseous amount, for example

$$Tr(gas, M) = \exp(a*(airmss*Ug)^\wedge n)$$

Equation 13: Calculation of gaseous transmittance

where Ug is the gaseous concentration (eg. total amount ozone in units of cm/atm; the amount of oxygen is calculated via pressure), a and n are coefficients which depend on the response of the given spectral band. Details can be found in Tanré et al (1990) [LIT15] and the SMAC model (Rahman and Dedieu, 1994 [LIT16]). The 6SV radiative transfer model is used to calculate $Tr(O_3, O_2, M)$ in each PROBA-V spectral band for a range of total amount of gas and a view angles. These 6SV runs are used to derive the coefficients of the exponential relationship.

⇨ **Estimate for each pixel the aerosol optical thickness (AOT^{est}):** the simulated $\rho_{TOA}^{c,model}(NIR)$ (in the global LUT or the on-the-fly calculated LUT) are interpolated on the angles, water vapour and pressure from each pixel to obtain $\rho_{TOA}^{c,model}(NIR)$ corresponding to the geometry and atmospheric conditions (water, pressure, windspeed) of the observation. Then $\rho_{TOA}^{c,model}(NIR, AOT_i)$ and $\rho_{TOA}^{c,model}(NIR, AOT_{i+1})$ that surround $\rho_{TOA}^{c,meas}(NIR)$ are the aerosol optical thickness (AOT^{est}) corresponding to $\rho_{TOA}^{c,meas}(NIR)$ is estimated through interpolation.

⇨ **Calculate ΛA^{BLUE} and ΛA^{RED} :**

For each pixel find $\rho_{TOA}^{c,model}(Blue, RED)$ corresponding to AOT^{est}: $\rho_{TOA}^{c,model}(Blue, RED, AOT^{est})$ is derived from interpolation between $\rho_{TOA}^{c,model}(Blue, RED, AOT_i)$ and $\rho_{TOA}^{c,model}(Blue, NIR, AOT_{i+1})$ at the estimated AOT^{est}. Next, for each pixel the change in calibration coefficients for the BLUE and RED bands is calculated as :

$$\Lambda A^{BLUE} = \frac{A_{BLUE}^{new}}{A_{BLUE}^{old}} = \frac{\rho_{TOA}^{c,meas}(BLUE)}{\rho_{TOA}^{c,model}(BLUE)} \; ; \Lambda A^{RED} = \frac{A_{RED}^{new}}{A_{RED}^{old}} = \frac{\rho_{TOA}^{c,meas}(RED)}{\rho_{TOA}^{c,model}(RED)}$$

4.4.1.2.2.3   Required ancillary data

Ancillary data required for the pixel selection, gaseous transmittance correction and LUT interpolation are:

⇨ **Wind speed at the sea level**

This parameter can be accessed through the European Center for Meteorological and Weather Forecast (ECMWF) . The typical accuracy attached to wind speed is of about 2 m/s.

⇨ **Atmospheric pressure at the sea level**

This parameter can be accessed through the European Center for Meteorological and Weather Forecast (ECMWF). About 5-10 mbars is a reasonable accuracy for the atmospheric pressure.

⇨ **Total ozone amount**

This parameter can be accessed through the European Center for Meteorological and Weather Forecast (ECMWF) or from the measurements of the Total Ozone Mapping Spectrometer (TOMS). An accuracy of about 10-20 mAtm-cm (Dobson Units, DU) is a typical accuracy for the total ozone amount of the atmosphere.

⇨ **Water vapor content**

This parameter can be accessed through the European Center for Meteorological and Weather Forecast (ECMWF). An uncertainty of 20 % is considered.

Other ancillary data (attached to the input image) : time, date, sun zenith angle, solar zenith angle, relative azimuth angle and a cloud mask (calculated from the image itself)

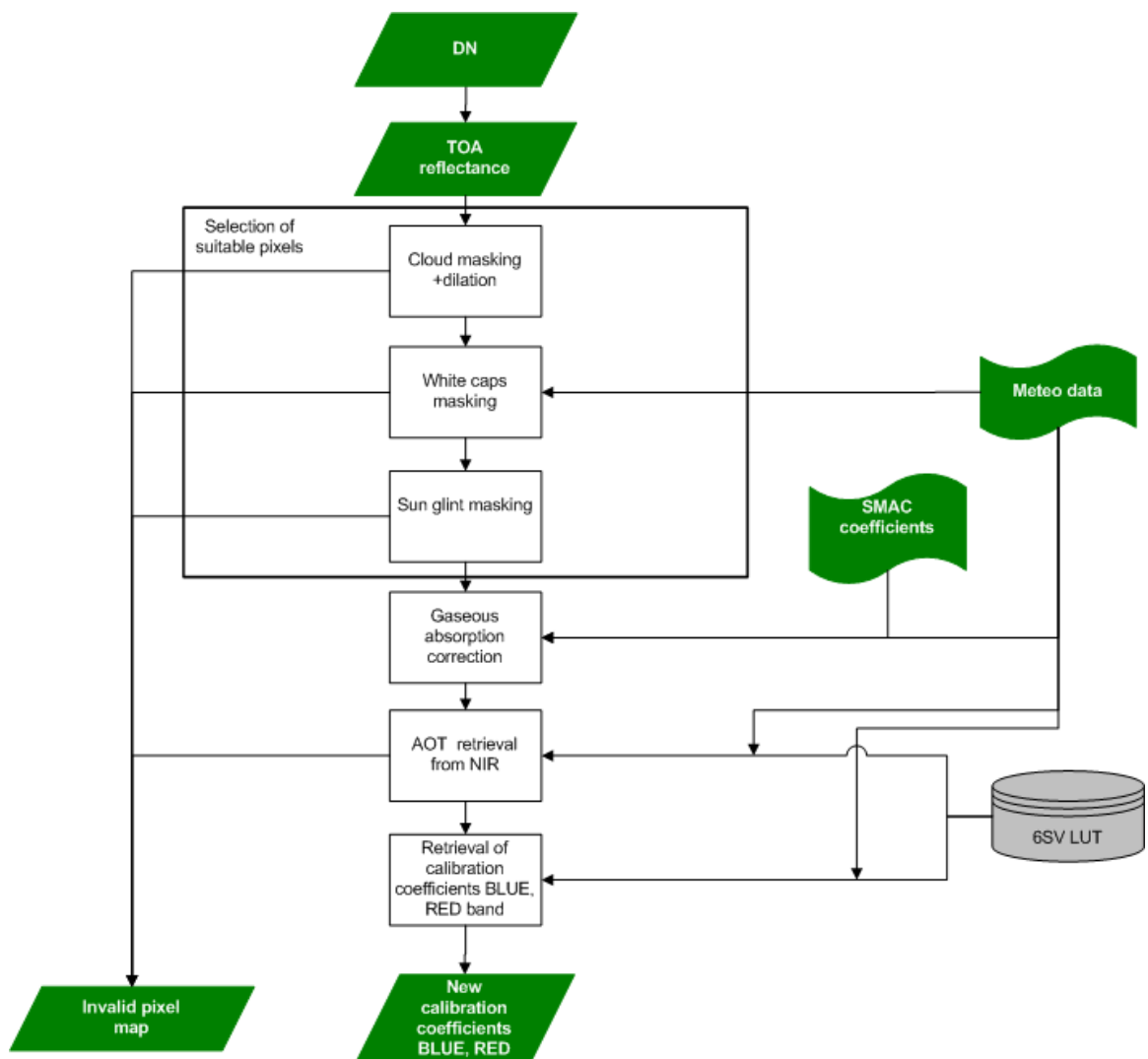### 4.4.1.2.2.4   Summary of the processing steps

Figure 8**: Overview flowchart Rayleigh calibration**

4.4.1.3   Error analysis

The considered error sources are :

1)   Surface pressure: a maximal error of 10 hPa is used in the error analysis

2)   Wind speed: The wind speed impacts the contribution of photons scattered by the atmosphere after their reflection over the sea-surface. A typical accuracy of 2 m/s in wind speed is used in making up the error budget.

3)   NIR calibration: an error of 3% is used to make the error budget

4)   Aerosol model: The aerosol model is assumed fixed (M98); Uncertainties in the calibration method related to the aerosol type are analyzed by calibrating a scene generated with a coastal aerosol (C70) with a LUT generated with M98

5)   Gaseous transmittance: An error in the ozone amount and water vapor of respectively 5 % and 20 % is used in the error budget. An uncertainty on water vapour will have a small direct effect on the RED band, and an indirect impact due to the aerosol retrieval in the NIR band.

6)   Chlorophyll content : an error of 50% on the chlorophyll concentration has been used for making up the error budget. This will have a direct effect on the BLUE and RED band, however as the water surface can be assumed totally black in the NIR band, an error in the chlorophyll content will have no effect on the AOT retrieval.

The error analysis is performed by using a LUT generated according to the reference specifications. This LUT is then used to perform a Rayleigh calibration on an artificial image generated according to the same specifications except for the parameter of interest (e.g. C70 model instead of M98 model in LUT) or by introducing an error in the meteo-data (e.g. 20 % error in water vapour).

Table 7 summarizes the error budget for the Rayleigh method for both BLUE and RED band. The table contains the average error, the error at 1-sigma and at 2-sigma The error sources are assumed to be non-correlated and thus the total error is the quadratic sum of all errors. The impact of uncertainties related to the input parameters is estimated on the calibration result. As uncertain impact parameters were considered : pressure, wind speed, NIR calibration, aerosol model, gaseous amount and marine reflectance (chlorophyll concentration).

As the exact spectral response curves for the PROBA-V bands are not yet known, this error analysis may be updated in a later phase.

Error Sources	BLUE			RED		
	average error (%)	1-sigma error (%)	2-sigma error (%)	average error (%)	1-sigma error (%)	2-sigma error (%)
Pressure	0.571	0.632	0.693	0.364	0.394	0.425
Wind speed	0.570	1.535	2.501	0.735	2.035	3.335
NIR calibration	0.580	0.650	0.720	1.822	1.943	2.065
Aerosol model	0.536	0.959	1.331	1.070	1.825	2.580
Ozone	0.029	0.032	0.036	0.267	0.300	0.333
Water vapour	0.047	0.102	0.157	0.089	0.135	0.181
Chlorophyll	0.951	1.106	1.261	0.280	0.334	0.388
Total absolute	**1.477**	**2.310**	**3.262**	**2.301**	**3.409**	**4.745**

Table 7: Summary of Rayleigh absolute calibration error budget.

In the BLUE band the performance is determined by the accuracy on the wind speed, marine reflectance and aerosol model. In the RED band the error in the NIR calibration, wind speed and aerosol model are the limiting factors to accuracy. In section 0 it is explained how the uncertainty calculation is used in the determining the final error budget.

4.4.2 Reflectance-based method

4.4.2.1 Introduction

In the reflectance-based method ground-based reflectance measurements are used as input. At the time of the PROBA-V overpass a field crew measures the spectral reflectance of the selected calibration site using a well-calibrated field spectroradiometer under optimal (cloud-free) weather conditions. Furthermore, the atmospheric and meteorological conditions during the overpass have to be accurately characterized using sun photometer measurements and meteo station data. Using a radiative transfer model the surface reflectance spectra can be converted to TOA radiance and compared to the measured PROBA-V radiance. (The accuracy of the reflectance-based method is generally lower than for the radiance-based method due to uncertainties in the aerosol modelling.) A higher accuracy is possible by the improved reflectance-based method which uses the same measured data as from the reflectance-based method as well as the measured ratio of diffuse-global spectral irradiance at ground level. Because of the mobilization costs of the field crew, the reflectance-based method will only be applied to validate the operational calibration methods at an ad hoc basis through collaboration with other teams or by joining calibration/validation exercises like the CEOS 2010 campaign at Tuz Gölü, Turkey, one of the eight CEOS endorsed core instrumented IVOS Sites (Table 8) provisionally called LANDNET sites. The characteristics of these eight LANDNET sites can be obtained from http://calval.cr.usgs.gov/sites_catalog_ceos_sites.php.

Core "Instrumented" IVOS Site	Center latitude	Center longitude	Point of Contact
Railroad Valley Playa, NV, USA, North America	38.50	-115.69	Dr. Kurtis J. Thome (kurtis.thome@nasa.gov) – NASA
Ivanpah, NV/CA, USA, North America	35.57	-115.40	Dr. Kurtis J. Thome (kurtis.thome@nasa.gov) – NASA
Lspec Frenchman Flat, NV, USA, North America	36.81	-115.93	Carol J. Bruegge (Carol.J.Bruegge@jpl.nasa.gov) – NASA JPL
La Crau, France, Europe	43.56	4.86	Patrice Henry (patrice.henry@cnes.fr) – CNES, France
Dunhuang, Gobi Desert, Gansu Province, China, Asia	40.13	94.34	Xiuqing Hu (huxq@cma.gov.cn)-NSMC/CMA, China
Negev, Southern Israel, Asia	30.11	35.01	Arnon Karnieli (karnieli@bgu.ac.il) – Ben Gurion University, Israël
Tuz Gölü, Central Anatolia, Turkey, Asia	38.83	33.33	Selime Gurol (selime.gurol@uzay.tubitak.gov.tr) – TUBITAK UZAY, Turkey
Dome C, Antartica	-74.50	123	Stephen Warren (sgw@atmos.washington.edu) – University of Washington, USA

Table 8: CEOS Core Instrumented IVOS Sites (LANDNET sites).

These instrumented reference test sites are primarily used for field campaigns to estimate the radiometric absolute calibration coefficients and can serve as a focus for international efforts, facilitating traceability and cross-comparison to evaluate biases of in-flight and future sensors in a harmonized manner.

An in-flight radiometric calibration experiment needs to be performed under clear sky conditions above at least one of the prime large and homogenous earth calibration targets (Teillet et. al., 2007 [LIT17]). In case of non-linearity of PROBA-V detectors, more calibration sites should be selected covering the full dynamic range (water, sand, ice,…).

Radiometry reference test site selection criterion put forward by the CEOS WGCV subgroup IVOS are listed in Table 9 (Teillet et al., 2007 [LIT17]).

Selection criterion	Purpose
High spatial uniformity over a large area (within 3%)	Minimize misregistration and adjacency effects
Surface reflectance greater than 0.3	Provide higher SNR and reduce uncertainty due to atmosphere
Flat spectral reflectance	Reduce uncertainties due to different spectral response profiles
Temporally invariant surface properties (within 2%)	To reduce BRDF, spectral, surface reflectance effects
Horizontal surface with nearly lambertian reflectance	Minimize uncertainty due to different solar illumination and observation geometry, to minimize slope-aspect effects
At high altitude, far from ocean, urban, and industrial areas	Minimize aerosol loading and atmospheric water vapour, to minimize anthropogenic aerosols
In arid regions with low probability of cloud cover	Minimize precipitation that could change soil moisture and to increase the probability of the satellite instruments imaging the test site at the time of the overpass.

Table 9: Radiometry reference test site selection criterion.

An on-line Catalogue of worldwide test site for sensor characterization is available at http://calval.cr.usgs.gov/sites_catalog_map.php.

CEOS envisages a free and open data policy. Satellite products and in-situ data from a number of test sites (not all LANDNET sites are included yet) can be queried free of charge from the CEOS cal/val portal (http://calvalportal.ceos.org/cvp/web/guest). The objective of CEOS is to provide by 2012 through the CEOS cal/val portal satellite and in-situ data from all LANDNET sites free of charge to the cal/val community (N. Fox, private communication, December 2009). Recently added to the list of CEOS instrumented site is the calibration site at Tuz Gölü, Turkey. Tuz Gölü (Latitiude 38°46'21.00''N, Longitude 33°28'23.16''E) is a salt lake which dries to a salt surface for about 3 month a year (mainly halite and gypsum with minor amounts of polyhalite and coelestine) in central Anatolia in Turkey far from the influence of the sea. In July and August the dried salt lake has a homogeneous area over 324.026 km². The dried salt lake surface is smooth, uniform (spatially uniform with RMS of deviation from mean smaller than 2% for a 300x100 m target), flat (slope less than 1°) and with high surface reflectance (0.4-0.58 in VNIR). July and August are the optimum months for reflectance-based radiometric calibration as these months are the most dry, sunny and cloud-free months of the year based on local data between 1987 and 2007. All these characteristics together with the fact that Tuz Gölü is easily accessible especially for Europe makes this site well suited for the radiometric calibration of PROBA-V.

4.4.2.2 Algorithm

4.4.2.2.1 Physics of the algorithms

Reflectance-based method
The reflectance-based method uses ground-based reflectance measurements as primary input. At the time of the overpass the upwelling radiance of the test site is measured and divided by the

measured radiance of the calibration panel to become the reflectance of the test site. Measurements should be taken in a short time frame (40 minutes) to prevent change of atmospheric conditions and changing illumination conditions. Measurements are taken over ground blocks of 100 m x 100 m (size of nadir PROBA-V BLUE, RED, NIR pixels) and averaged to account for spatial variation. The size of the measurement site is typically 4 cross track pixels and 16 along track pixels (Biggar et al., 2003 [LIT18]) which means for PROBA-V 16 x 4 100 m pixels. As described in Thome, 2001 [LIT19] measurements with a field spectroradiometer are taken parallel to the across track direction in the center of the 4 across track pixels. This sampling strategy is repeated 16 times for the along track pixels. With the field spectroradiometer (8° FOV foreoptic at 2 m height means a ground diameter of 0.3 m) 30 spectra per sample are collected. For each pixel 10 spectra are averaged. That means in total 300x4x16=19200 (N) spectra and 640 samples are collected over the total area of the site (sampling strategy to be updated). Collecting this data takes 45 to 60 minutes. Reflectance is determined by the ratio of the radiance of the reference target L_{ref} by the BRDF corrected radiance of the spectralon calibration panel L^{BRDF}_{panel} for which the BRDF factor is determined in the lab. The calibration panel radiance is measured at the start and end of the data collection and after each 8 pixels or 80 samples.

$$\rho_{ref} = \frac{1}{N} \sum_{pixels} \frac{Lref}{L^{BRDF} panel}$$
Equation 14

All reflectance spectra are averaged to give one single reflectance spectrum for the measured test site. Global, downwelling irradiance data are also collected near the test site to determine if there are significant changes in diffuse skylight illumination during the measurement period.
Positions of the ground-based measurements need to be recorded by a Global Positioning System (GPS) to locate the measured pixels in the PROBA-V image. Another possibility is to mark the corners of the site with large tarpaulins visible in the PROBA-V image.
The atmospheric parameters like aerosol optical depth, Angström coefficient and water vapour content is determined from sun photometer measurements following the Langley method based on measurement of direct solar radiation whose voltage output V can be written as:

$$V = V_0 \cdot D_s \cdot Tr_{gas} \cdot e^{-\tau M}$$
Equation 15

with V sun photometer voltage output, V_0 calibration coefficient, D_s Sun-Earth distance factor given by

$$D_s = \frac{1}{1 - 0.01673\cos[0.9856(JD - 4)]}$$
Equation 16

with JD the day of the year and Tr_{gas} gaseous transmittance, τ the total atmospheric optical depth (sum of optical depth due to aerosol scattering and optical depth due to Rayleigh scattering) and M air mass which depends on the solar zenith angle and the pressure.
When applying the natural logarithm on equation Equation 15, it can be written as:

$$\ln\left[\frac{V}{D_s Tr_{gas}}\right] = \ln V_0 - \tau M$$
Equation 17

A plot of ln[V/DsTrgas] versus M for several solar zenith angles and an assumed stable atmosphere gives V0 (=e[intercept]) and the total optical depth τ (=-slope). From τ and $\tau_{Rayleigh}$ (the latter only depends on wavelength and pressure) $\tau_{aerosol}$ can be determined for the bands not affected by water vapour.

The spectral variation of aerosol optical depth can be written (according Angström's turbidity formula) as

$$\tau_{aerosol}(\lambda) = \beta\lambda^{-\alpha}$$

Equation 18

with β the Angström turbidity coefficient that is proportional to the horizontal visibility (VIS) according formula

$$\beta = 0.613 \, e^{-VIS/15}$$

Equation 19

and α the Angström coefficient (α in function of wavelength).

By plotting measured τaerosol in function of wavelength and fitting Equation 18 to these points, β (and thus VIS (in km)) and α can be determined. Subsequently, knowing α and β, AOT550 which is equal to τaerosol(550 nm) can be estimated from Equation 18.
By plotting the measured τ as a function of wavelength and fitting Equation 20 to these points, τ at the water vapour affected band can be determined.

$$\tau(\lambda) = ae^{b/\lambda}$$

Equation 20

The spectral band at 936 nm can be used to estimate water vapour content UW as there is an important water vapour absorption band in this spectral region. Here the Tr_{gas} is not equal to 1 but is estimated from

$$Tr_{gas} = e^{-0.6767.UW^{0.5093}.M^{0.5175}}$$

Equation 21

The Langley equation can now be written as:

$$\ln\left[\frac{Ve^{\tau M}}{D_s}\right] = \ln V_0 - UW^{0.5093}(0.6767M^{0.5175})$$

Equation 22

and thus V0 at 936 nm and UW (g/cm^2) can be determined.

Using a radiative transfer model (such as 6SV) the measured reference reflectance ρref is converted to TOA radiance L_{TOA}^{ref} using input aerosol optical thickness at 550 nm, Angström coefficient, and water vapour determined from sun photometer measurements. Subsequently the ground-based TOA radiance measurements are convolved with the PROBA-V spectral response function S(λ) according the following equation:

$$L_{TOA}^{k,ref} = \int L_{TOA}^{ref} S_k(\lambda)d\lambda$$

Equation 23

Finally L_{TOA}^{ref} are compared to the TOA radiance measured by PROBA-V L_{TOA}^{meas} (average of 4 along track x 16 along track pixels; we assume nadir PROBA-V viewing geometry, in case of non-nadir viewing geometry a BRDF correction will be applied based on goniometer measurements of the reference site).

This method can cause problems for sensors with coarse ground resolution (300 m-1200 m) because of the required time to sample the test site. Another disadvantage are the assumptions made for aerosol size and composition.

4.4.2.2.2   **Algorithm implementation**

4.4.2.2.2.1   Processing

Ground-based measurements processing

⇨ **Divide ground measured** reference site radiance by BRDF corrected radiance of the calibration panel to become ground-based reflectance (including a bidirectional reflectance factor correction for the solar zenith angle)

⇨ **Averaging** of ground-based reflectance measurements

⇨ **Radiative transfer calculations** (e.g. 6SV) (with as input aerosol optical thickness at 550 nm, Angström coefficient, and water vapour determined from sun photometer measurements) to convert ground-based surface reflectance to TOA radiance L_{TOA}^{ref} .

⇨ **Convolution with PROBA-V spectral response**: the modelled L_{TOA}^{ref} data measurements are convolved with the PROBA-V spectral bands.

PROBA-V processing

⇨ **Extract** calibration site pixels (4 across track x 16 along track pixels)

⇨ **Conversion** of DN to L_{TOA}^{meas} : The input DNs for all selected image pixels are converted to TOA radiance L_{TOA}^{meas} following Equation 4.

⇨ **Clear pixel selection** : Visual inspection for clouds. The reflectance-based method is only applied under optimal weather conditions (cloud-free).

⇨ **Calculate** ΛA^k : for each pixel the change in calibration coefficients for the BLUE, RED, NIR and SWIR bands is calculated based on a comparison of PROBA-V and ground-based TOA radiance as :

$$\Lambda A^{BLUE} = \frac{A_{BLUE}^{new}}{A_{BLUE}^{old}} = \frac{L_{TOA}^{meas}(BLUE)}{L_{TOA}^{ref}(BLUE)} ; \Lambda A^{RED} = \frac{A_{RED}^{new}}{A_{RED}^{old}} = \frac{L_{TOA}^{meas}(RED)}{L_{TOA}^{ref}(RED)}$$

$$\Lambda A^{NIR} = \frac{A_{NIR}^{new}}{A_{NIR}^{old}} = \frac{L_{TOA}^{meas}(NIR)}{L_{TOA}^{ref}(NIR)} ; \ \Lambda A^{SWIR} = \frac{A_{SWIR}^{new}}{A_{SWIR}^{old}} = \frac{L_{TOA}^{meas}(SWIR)}{L_{TOA}^{ref}(SWIR)}$$

4.4.2.2.2.2   Required ancillary data

Required ground-based equipment for determining ground-based TOA radiance

⇨ field spectroradiometer (e.g. FieldSpec Pro FR) for reflectance measurements
⇨ field spectroradiomete (e.g. FieldSpec Pro FR) + cosine receptor for downwelling irradiance measurements
⇨ spectralon calibration panel
⇨ sun photometer
⇨ GPS

Ancillary data for the processing of the ground-based reflectance measurements to ground-based TOA radiance

⇨ **Bidirectional reflectance factor for the spectralon calibration panel as determined in the lab**

⇨ **Aerosol optical thickness**
This parameter is determined from sun photometer measurements and is input parameter of the Radiative Transfer Codes (e.g. 6SV) to convert ground-based reflectance measurements to TOA radiance.

⇨ **Angström coefficient**
This parameter is determined from sun photometer measurements and gives to a certain extent an indication of size distribution and thus the aerosol type. From the Angstrom coefficient the aerosol model is determined which is used in the Radiative Transfer Codes (e.g. 6SV) to convert ground-based reflectance measurements to TOA radiance.

⇨ **Water vapour content**
This parameter is determined from sun photometer measurements and is input parameter of the Radiative Transfer Codes (e.g. 6SV) to convert ground-based reflectance measurements to TOA radiance.

⇨ **Position**
Position of ground-based reflectance measurements from hand-held GPS measurement to localize the measurements in the PROBA-V image.

⇨ **Terrain height**
Terrain height (proxy for pressure) is an input parameter of Radiative Transfer Code (e.g. 6SV).

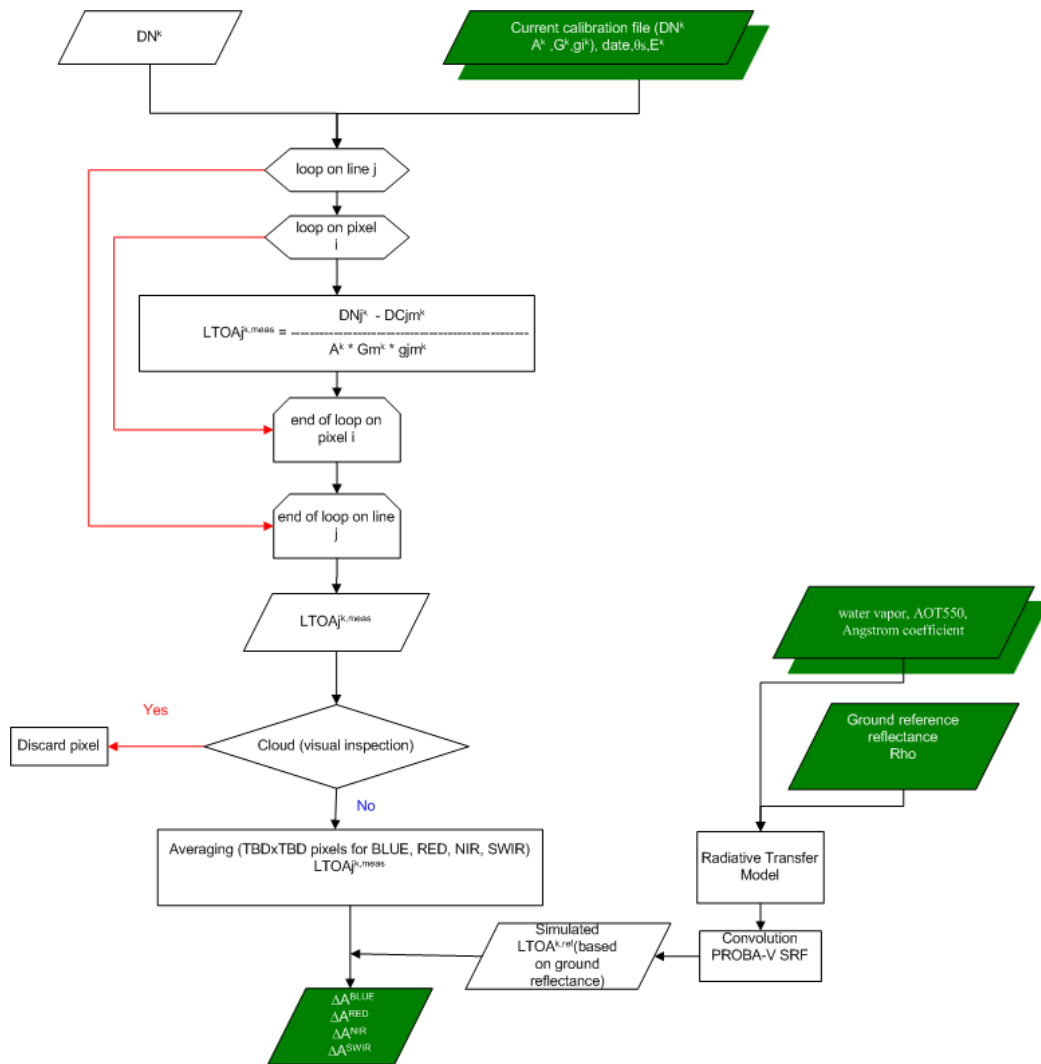#### 4.4.2.2.2.3 Summary of processing steps

Figure 9: Flowchart to calculate calibration coefficients

4.4.2.3   Error analysis

There are four basic areas of uncertainty in the method: (1) atmospheric characterization, (2) surface characterization, (3) radiative transfer code, and (4) computation of the site-average DNs (or radiance). The factors leading to uncertainties in determining the site average DN are an incorrect determination of the site's location in the image and the subsequent misregistration of the site's surface reflectance to DN (or radiance) (Thome 2001 [LIT19]).

The uncertainty has been estimated at 4.9% for the reflectance-based method and 3.5% for the improved reflectance based method (Dinguirard and Slater, 1999 [LIT20]; Biggar et al. 1994 [LIT21]). With improved equipment and techniques soon an uncertainty of 3.3% and 2.8% should become feasible.

Estimated measurement uncertainties for the reflectance-based and improved reflectance-based methods are listed in Table 10 (Dinguirard and Slater, 1999 [LIT20]; Biggar et al. 1994 [LIT21]). The error given is the error in the TOA radiance caused by the error source. All percentages are 1 σ. We assume the error sources are independent such that the total error is the root sum of squares of the errors caused by all listed error sources.

Error Sources	Error
Ground reflectance measurement	2.1
Optical depth measurements	1.1
Absorption computations	1.3
Choice of aerosol complex index	2.0
Choice of aerosol size distribution	3.0
Vertical distribution	1.0
Non-lambertian ground characteristics	1.2
Non-polarization vs. polarization code	0.1
Inherent code accuracy	1.0
Uncertainty in the value of µsum	0.2
Total error (root sum of squares)	**4.9**

Table 10: Error sources of reflectance-based method.

4.4.3 Radiance-based method: APEX underflights

4.4.3.1 Introduction

APEX, Airborne Prism Experiment, is an airborne (dispersive pushbroom) imaging spectrometer developed by a Swiss-Belgian consortium on behalf of ESA, (Itten et al., 2008 [LIT22]) to calibrate/validate and simulate future spaceborne missions. The main APEX specifications are listed in Table 11.

APEX main specifications	
Spectral range	VNIR: 380-970 nm
	SWIR: 940-2500 nm
Spectral bands	VNIR: default 114 bands, reprogrammable through customized binning pattern.
	Max. unbinned bands 334
	SWIR: 199 bands
Spectral sampling interval	VNIR: 0.55-8 nm over spectral range (unbinned)
	SWIR: 5-10 nm over spectral range
Spectral resolution (FWHM)	VNIR: 0.6-6.3 nm over spectral range (unbinned)
	SWIR: 6.2-11 nm over spectral range
Spatial pixels	1000
FOV (across track)	28°
IFOV	0.48 mrad
Spatial sampling interval (across track)	1.75 m @ 3500 m AGL
Sensor dynamic range	VNIR: CCD, 14 bit encoding
	SWIR: CMOS, 13 bit encoding

| Pixel size | VNIR : 22.5 μm x 22.5 μm |
| | SWIR: 30 μm x 30 μm |

Table 11: APEX main specifications

The APEX Science Center is located at the University of Zurich while the APEX Operation Center is located at VITO. Flight campaign planning is coordinated from VITO. The processing of the APEX data (geometric and atmospheric correction) is performed at VITO's Central Data Processing Center (CDPC) (Biesemans et al., 2007 [LIT23]).

The.in the CHB (Calibration Home Base) well-calibrated hyperspectral airborne APEX sensor can serve as an excellent instrument to carry out an in-flight spectral calibration of PROBA-V. The main advantages of using APEX are (Nieke, 2001 [LIT24])
1. the measured radiance of APEX and PROBA-V can be compared directly when both view the same ground pixel at the same time (cfr. Sampling problem of field spectroradiometers)
2. the uncertainties of the atmosphere can be minimized by flying well above the boundary layer of the atmosphere
3. in contrast to PROBA-V, APEX can be re-calibrated on the ground in the Calibration Home Base (based at DLR)
4. no calibration panel is required
5. APEX allows fast sampling over a large calibration site and thus can be used for calibration of low, medium as well as high resolution spaceborne sensors

This in-flight calibration experiment should be performed under stable atmospheric conditions (cloud free, small aerosol loading) above at least one of the prime large spatial uniform earth calibration targets (e.g. Tuz Gölü, Turkey). In case a suspicion of non-linearity of PROBA-V detectors exists, more calibration sites should be selected covering the full dynamic range (water, sand, ice,…). The combination of both lower-reflectance and higher-reflectance targets improves the quality of the calibration (Teillet et al., 2001 [LIT25]).

In the direct method, the radiance values measured by APEX at airborne level (e.g. at 7 km) in the wavelength range from 380 nm to 2500 nm are converted to TOA radiances using a radiative transfer code to take into account residual scattering and absorption between aircraft and satellite. The APEX-based TOA radiances are then spectrally resampled to the spectral response curves of PROBA-V and compared to the PROBA-V TOA measurements to check or compute the absolute calibration coefficients of PROBA-V.

In order to have the same illumination conditions, APEX acquisitions should be timed to coincide with the PROBA-V overpass. That means at Tuz Gölü at TBD (dependent on PROBA-V launch) LST (Local Solar Time). Furthermore, to have the same viewing conditions for PROBA-V and APEX, the nadir centre lines should coincide as well. In this configuration only the centre PROBA-V sensor can be calibrated. To be able to calibrate also the left and right sensor, the PROBA-V sensor will be tilted (roll manoeuvre) +17,5° which will allow nadir viewing of the left and centre sensor (overlapping pixels) and subsequently in a next PROBA-V overpass tilted (roll manoeuvre) -17,5° which will allow nadir viewing of the centre and right sensor (overlapping pixels).

At 7 km altitude above ground level (AGL), the APEX FOV (+/- 14°) results in a swath width of 3491 m and 3.5 m pixels. A swath width of 3491 m corresponds to approximately 34 100 m PROBA-V pixels.

Averaging of pixels (34x34 PROBA-V pixels for the BLUE, RED and NIR and 11x11 PROBA-V pixels for the SWIR) is required to reduce uncertainties due to inhomogeneities of the calibration site and mis-registration between APEX and PROBA-V.

Due to high operational costs, calibration on the basis of aircraft underflights cannot be considered as a fully operational method for the exploitation phase but will be performed as validation once or twice a year.

4.4.3.2   Algorithm

4.4.3.2.1   Physics of the algorithms

There are two methods to determine TOA radiance from APEX data. The indirect method and the direct method:

The **direct method** compares directly the TOA PROBA-V radiance to the APEX radiance corrected for the remaining atmospheric contribution between APEX and PROBA-V without using additional ground-truth data.

The **indirect comparison method** starts from APEX radiance (the sun-reference site-APEX geometry should be known) which is converted to surface reflectance using a radiative transfer model (MODTRAN, 6SV) taking into account the viewing and observation geometry and atmospheric properties.

The direct method without using ground-truth instruments may not reach the same accuracy as the indirect method (Hovis et al., 1985 [LIT26]). Therefore we propose to follow the indirect comparison method of which the physics is described below:

First the APEX scan lines of a segment l are averaged according:

$$\overline{L^{k,ref}}_{i,l}(\theta_{sl},\theta_v,\Delta\phi) = \frac{1}{J}\sum_{j=1}^{J} L^k{}_{i,j,l}{}^{ref}(\theta_{sl},\theta_v,\Delta\phi)$$

Equation 24

with θ_v view zenith angle, θ_s solar zenith angle, $\Delta\phi$ relative azimuth angle between solar azimuth and view azimuth direction, i image pixel, j image line, k spectral band index, l flight line segment and J total number of flight lines in an image segment.

Ground truth measurements of aerosol optical thickness and water vapour, reflectance and BRDF are taken to constrain the atmospheric correction and to characterize the calibration site.

For the atmospheric characterization the Langley method as already described in 4.4.2.2.2.1 is used to determine aerosol optical depth, Angström coefficient and water vapour content.

The average radiance measured by APEX ($\overline{L^{k,ref}}_{i,l}$) is then atmospherically corrected to obtain the average surface reflectance. This is done at VITO's Central Date Processing Center (CDPC) for airborne hyperspectral data (Biesemans et al., 2007 [LIT23]). The input parameters for the MODTRAN-based atmospheric correction performed in the CDPC are visibility or aerosol optical depth (AOT550), ozone and water vapour concentration, terrain elevation, aircraft altitude and sun-viewing geometry. After atmospheric correction (f^1) the surface reflectance averaged over the scan lines is obtained.

$$\overline{\rho^{k,ref}}_{i,l}(\theta_{sl},\theta_v,\Delta\phi) = f^{-1}\sum_{j=1}^{J} L^k{}_{i,j,l}{}^{ref}(\theta_{sl},\theta_v,\Delta\phi)$$

Note that the surface reflectance is still a function of bidirectional reflectance of the surface.

In a next step the surface reflectance is adjusted to nadir view angle and an average solar zenith angle during APEX data acquisition.

$$\overline{\rho^{k,ref}}_{i,l}(\overline{\theta}_s,0°,0°) = \overline{\rho^{k,ref}}_{i,l}(\theta_{sl},\theta_v,\Delta\phi)\left[\frac{\overline{\rho^{k,ref}}(\overline{\theta}_s,0°,0°)}{\rho^{k,ref}(\theta_{sl},\theta_v,\Delta\phi)}\right]_{BRDF}$$

Equation 25

Bidirectional reflectance factor adjustment can be determined from goniometer measurements of the calibration site.

The BRDF corrected pixels are then averaged to obtain a single reflectance for one flight line segment with I the total number of pixels in a scan line

$$\overline{\rho^{k,ref}}_{l}(\overline{\theta_{s}},0°,0°) = \frac{1}{I}\sum_{i=1}^{I}\rho^{k}_{i,l}{}^{ref}(\overline{\theta_{s}},0°,0°)$$

Equation 26

In case more than one flight line segment cover the calibration site, one has to average over the total number of flight line segments L to obtain a single averaged reflectance for the entire calibration site.

$$\overline{\rho^{k,ref}}(\overline{\theta_{s}},0°,0°) = \frac{1}{L}\sum_{l=1}^{L}\rho^{k}_{l}{}^{ref}(\overline{\theta_{s}},0°,0°)$$

Equation 27

Starting from the single averaged calibration site reflectance (standardized for nadir viewing and average solar zenith angle), one can estimate the TOA radiance that PROBA-V should see following three steps: i) BRDF adjustment of the standardized surface reflectance for the PROBA-V geometry; ii) conversion of reflectance to TOA radiance by adding atmosphere (inverse atmospheric correction; iii) convolution with PROBA-V spectral response function.

The BRDF adjustment of the standardized APEX-reference surface reflectance for the PROBA-V geometry (sat refers to the solar and viewing angles pertinent to PROBA-V imaging the calibration site) can be written as:

$$\overline{\rho^{k,ref}}(\theta_{s,sat},\theta_{v,sat},\Delta\phi_{sat}) = \overline{\rho^{k,ref}}(\overline{\theta_{s}},0°,0°)\left[\frac{\overline{\rho^{k,ref}}(\theta_{s,sat},\theta_{v,sat},\Delta\phi_{sat})}{\overline{\rho^{k,ref}}(\overline{\theta_{s}},0°,0°)}\right]_{BRDF}$$

Equation 28

The BRDF adjustment factor need to be determined for the different PROBA-V spectral bands.
The conversion of reflectance to TOA radiance using a Radiative Transfer Model is represented by

$$\overline{L^{k,ref}}(\theta_{s,sat},\theta_{v,sat},\Delta\phi_{sat}) = f\left(\overline{\rho^{k,ref}}(\theta_{s,sat},\theta_{v,sat},\Delta\phi_{sat})\right)$$

Equation 29

with the Radiative Transfer Model denoted with *f* for simplicity.
The same atmospheric parameters as for the APEX atmospheric correction are used while allowing a sensor altitude difference. (BRDF is taken into account in 6SV). This two-way use of the same aerosol optical depth for the APEX-based surface reflectance retrieval and the TOA radiance prediction results in a low sensitivity to aerosol optical depth (0.5% increase in TOA radiance for an aerosol optical depth which is double the amount on the APEX flight (Teillet et al., 2001 [LIT25]).
The final step is the convolution of the predicted TOA radiance with the PROBA-V spectral response function as follows:

$$L_{TOA}^{ref}(BLUE) = \int \overline{L^{k,ref}}(\theta_{s,sat},\theta_{v,sat},\Delta\phi_{sat})S^{BLUE}(\lambda)d\lambda$$

$$L_{TOA}^{ref}(RED) = \int \overline{L^{k,ref}}(\theta_{s,sat},\theta_{v,sat},\Delta\phi_{sat})S^{RED}(\lambda)d\lambda$$

$$L_{TOA}^{ref}(NIR) = \int \overline{L^{k,ref}}(\theta_{s,sat},\theta_{v,sat},\Delta\phi_{sat})S^{NIR}(\lambda)d\lambda$$

$$L_{TOA}^{ref}(SWIR) = \int \overline{L^{k,ref}}(\theta_{s,sat},\theta_{v,sat},\Delta\phi_{sat})S^{SWIR}(\lambda)d\lambda$$

Equation 30

The change in calibration coefficients for the BLUE, RED, NIR (SWIR) bands is calculated based on a comparison of the measured PROBA-V radiance averaged over all 34x34 (11x11) PROBA-V pixels and APEX-based TOA radiance as:

$$\Lambda A^{BLUE} = \frac{A_{BLUE}^{new}}{A_{BLUE}^{old}} = \frac{L_{TOA}^{meas}(BLUE)}{L_{TOA}^{ref}(BLUE)} \; ; \Lambda A^{SWIR} = \frac{A_{SWIR}^{new}}{A_{SWIR}^{old}} = \frac{L_{TOA}^{meas}(RED)}{L_{TOA}^{ref}(RED)}$$

$$\Lambda A^{SWIR} = \frac{A_{SWIR}^{new}}{A_{SWIR}^{old}} = \frac{L_{TOA}^{meas}(NIR)}{L_{TOA}^{ref}(NIR)} \quad \Lambda A^{SWIR} = \frac{A_{SWIR}^{new}}{A_{SWIR}^{old}} = \frac{L_{TOA}^{meas}(SWIR)}{L_{TOA}^{ref}(SWIR)}$$

Equation 31

4.4.3.2.2 Algorithm implementation

4.4.3.2.2.1 Processing

APEX processing

⇨ **Extract** reference site (segment) from georeferenced APEX image

⇨ **Clear pixel selection:** pixels affected by clouds, cloud shadow, haze are removed in the CDPC

⇨ **Average scan angle image**: the scan lines of the segment are averaged

⇨ **Atmospheric correction** with MODTRAN (CDPC) using AOT estimate, Angström coefficient and water vapour content from sun photometer measurements to retrieve surface spectral reflectance as a function of view angle

⇨ **BRDF correction**: to become reflectance for nadir view angle and average solar zenith angle

⇨ **Average surface reflectance** for all pixels in scan line

⇨ **Repeat** previous steps in case more than one APEX flight line is needed to cover the reference site

⇨ **BRDF correction** of standardized surface reflectance for averaged PROBA-V geometry

⇨ **Simulate atmosphere**: Conversion with MODTRAN of BRDF corrected surface reflectance to TOA radiance by adding atmosphere using same AOT estimate, Angström coefficient and water vapour content from sun photometer measurements as used for the APEX atmospheric correction and using the same solar irradiance.

⇨ **Convolution** with PROBA-V spectral response function

PROBA-V processing

⇨ **Extract** calibration site pixels

⇨ **Conversion of DN to** L_{TOA}^{meas}: The input DNs for all selected image pixels are converted to TOA radiance $L_{TOA}^{k,meas}$ following Equation 4.

⇨ **Clear pixel selection :** Visual inspection for clouds. The APEX-based method is only applied under optimal weather conditions (cloud-free).

⇨ **Averaging** PROBA-V radiance for near nadir calibration site pixels (34x34 pixels for BLUE, RED, NIR, 11x11 pixels for SWIR)

⇨ **Comparison** of averaged APEX-based TOA radiance with averaged nadir PROBA-V TOA radiance

4.4.3.2.2.2　Required ancillary data

Goniometer for BRDF measurements to determine BRDF correction factor for reference site (available from CEOS by 2012)

Sun photometer to determine Aorosol Optical Thickness, Angström coefficient and water vapour content

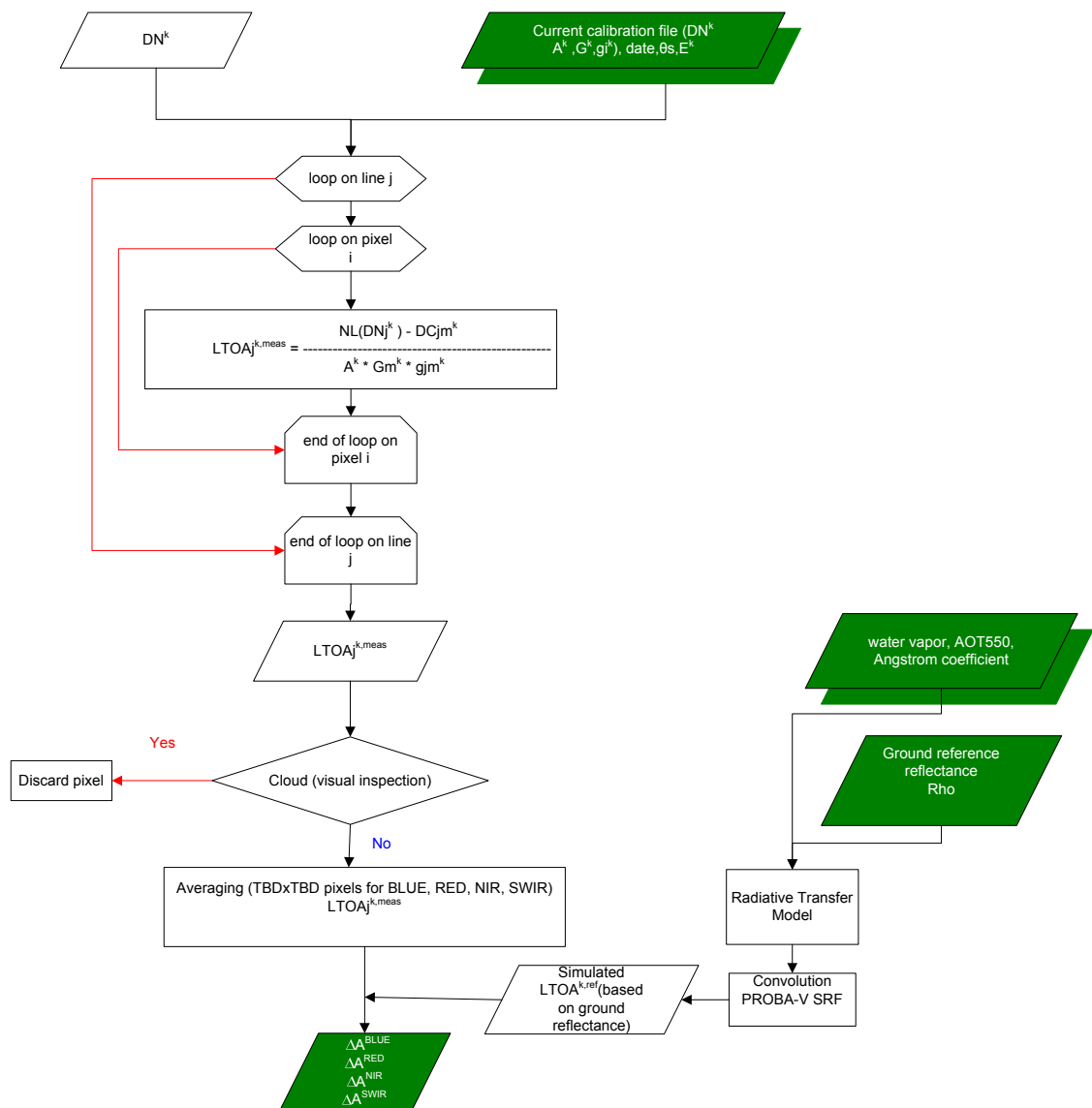#### 4.4.3.2.2.3　Summary of the processing steps

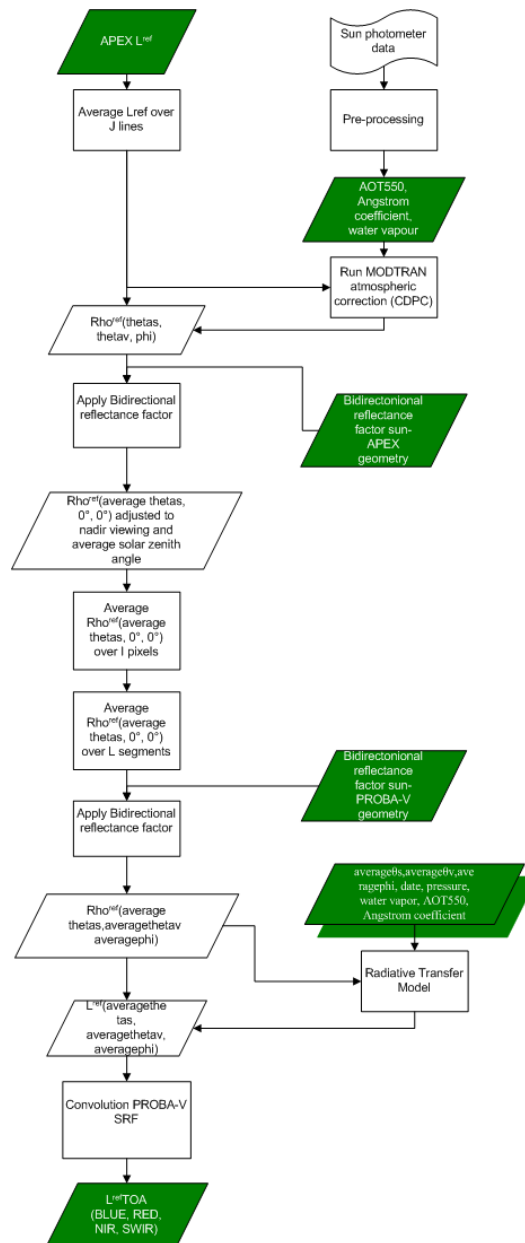**Figure 10: Flowchart to calculate calibration coefficients**

Figure 11: Flowchart for APEX-based TOA radiance for PROBA-V spectral bands

4.4.3.3 Error analysis

The uncertainty has been estimated at 2.8% for the radiance-based indirect method (Biggar et al., 1994 [LIT21]). A precision of 1.8% can be obtained with new instrumentation (Dinguirard and Slater, 1999 [LIT20]). The major contribution to uncertainty is related to the calibration of the airborne spectroradiometer. The error given is the error in the TOA radiance caused by the error source. All percentages are 1 σ. We assume the error sources are independent such that the total error is the root sum of squares of the errors caused by all listed error sources.

Error Sources	Error
Radiometer calibration	2.5
Measurement accuracy	1.3
Correction for altitude difference	<0.1
Total error (root sum of squares)	**2.8**

Table 12: Error sources for radiance-based method with reference to NIST standards.

4.4.4 Absolute calibration over stable deserts

4.4.4.1 Desert Sites selection

Deserts are well suited as test sites because they are usually very stable over time (good for multi-temporal calibration) and are seldom covered by clouds. Also they are spatially homogeneous.We compile a list of criteria based on Cosnefroy et al., 1996 [LIT38] and also note their requirements for suitable test sites next to them in . In line with these criteria, a set of 20 suitable test sites have been selected in North Africa and Saudi Arabia. They are shown on a map in (reproduced from (Cosnefroy et al., 1996 [LIT38]) and listed in .

Criterium	Requirement
Spatial homogeneity	2 or 3% dispersion threshold on TOA reflectance over 100x100 km area
Temporal stability	15- 20 % or better at seasonal scale, after correction for atmospheric effects
Low directional effects	< 15 %, based on AVHRR data
Low cloud coverage	> 50 % clear days annual
Low precipitation	< 10 mm /month

Table 13: Selection criteria and requirements for suitable desert sites

Country & number	Latitude	Longitude
Algeria 1	23,80	-0,40
Algeria 2	26,09	-1,38
Algeria 3	30,32	7,66
Algeria 4	30,04	5,59
Algeria 5	31,02	2,23
Mauritania 1	19,40	-9,30
Mauritania 2	20,85	-8,78
Mali 1	19,12	4,85

Country & number	Latitude	Longitude
Niger 1	19,67	9,81
Niger 2	21,37	10,59
Niger 3	21,57	7,96
Libya 1	24,42	13,35
Libya 2	25,05	20,48
Libya 3	23,15	23,10
Libya 4	28,55	23,39
Egypt 1	27,12	26,10
Sudan 1	21,74	28,22
Arabia 1	18,88	46,76
Arabia 2	20,13	50,96
Arabia 3	28,92	43,73

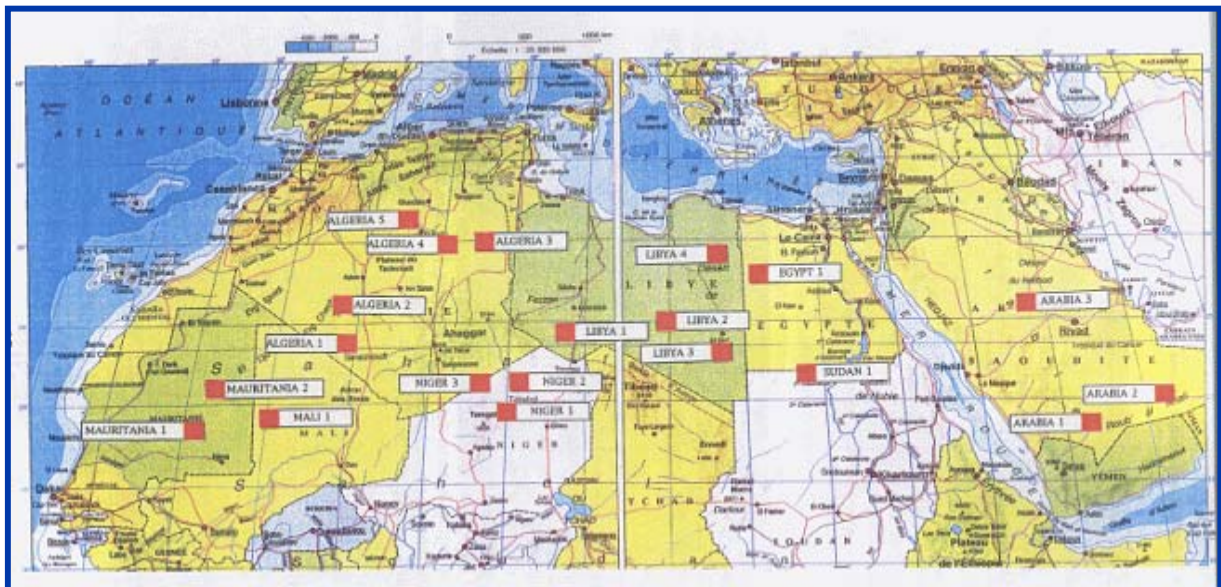**Table 14: Desert sites used for radiometric calibration**

Figure 12: Location of desert sites used for radiometric calibration,

The test sites are all covered by the normal operational imaging of PROBA-V. This has the advantage that they are imaged almost daily. No special settings are be used for their observation. Only clear pixels can be used for the analysis. If a substantial portion of the site is cloud covered, the observations for that site should not be used altogether for that day.

4.4.4.2   Desert Calibration Methodology

Desert calibration relies on the comparison between TOA reflectance as measured by the PROBA-V sensors ρ_{TOA}^{meas} and modelled TOA reflectances values ρ_{TOA}^{model} for these targets.

4.4.4.2.1 Calculation of modelled TOA reflectance values

Reference or modelled TOA reflectactance values (ρ_{TOA}^{model}) will be calculated using the radiative transfer code 6SV.

The modelled TOA reflectance values are determined by three types of factors:
- o   surface BRDF properties
- o   atmospheric conditions
- o   observation conditions including solar zenith angle, view zenith angle and relative azimuth angle.

4.4.4.2.1.1 Surface properties

The surface properties of desert sites can be described well with a simple BRDF model. We assume the surface properties to be stable over time, so they do not have to be updated. From these TOA radiances can be calculated for any given illumination and viewing condition.

The bi-directional reflectance (BRDF) of the surface of the desert sites can be modelled using a reflectance model. We use the standard Rahman-Pinty-Verstraete (RVP) model from Rahman et al., 1993 [LIT39]. It describes the reflectance in function of the direction of the illumination (θ_s, ϕ_s) and viewing (θ_v, ϕ_v), using only three parameters $(\rho_0, k$ and $\Theta)$:

$$\rho_s(\theta_s,\phi_s;\theta_v,\phi_v) = \rho_0 \frac{\cos^{k-1}\theta_s \cos^{k-1}\theta_v}{(\cos\theta_s + \cos\theta_v)^{1-k}}.F(g)(1+R(g)).$$

ρ_0 and k are two empirical surface parameters. ρ_0 characterizes the intensity of the reflectance of the surface, whereas k describes the anisotropy of the surface. F is the function:

$$F(g) = \frac{1-\Theta^2}{\left(1+\Theta^2 - 2\Theta^2\cos(\pi-g)\right)^{3/2}}$$

in which Θ controls the forward and backward scattering. The phase angle g is given by

$$\cos g = \cos\theta_s \cos\theta_v + \sin\theta_s \sin\theta_v \cos(\phi_s - \phi_v)$$

The hot spot effect is approximated by:

$$1 + R(G) = 1 + \frac{1-\rho_0}{1+G}$$

with

$$G = \sqrt{\tan^2\theta_s + \tan^2\theta_v - 2\tan\theta_s \tan\theta_v \cos(\phi_s - \phi_v)}$$

Reference reflectances should be available for every test site for a wide range of viewing angles. We make use of a descriptive database which accurately describes the 18 of the 20 test deserts sites (compiled by Govaerts Y., Eumetsat; not including Mauritania 1 and Arabia 3). For every desert, the database contains for all available angles the information:
1. wavelength
2. ρ_0 parameter
3. Θ asymmetry parameter
4. k parameter
5. hotspot parameter

4.4.4.2.1.2 Atmospheric properties

The main atmospheric parameter affecting the TOA reflectance are :
1. Atmopheric pressure
2. Ozone
3. Water vapour
4. Aerosol model and aerosol concentration

The first 3 will come from ECMWF meteo data.

The 6SV desert aerosol model is currently used. The AOT variability over the desert sites is mainly seasonal as can be seen in the few Aeronet sumphotometer stations nearest to the deserts sites (Figure 20). During 'winter' months (October to February) AOT values for all Aeronet site are significantly lower than the summer AOT values, similar to the monthly variation as used in Govaerts and Clerici 2004, [LIT1] (Cyan coloured line in figure). The team at CNES is however using in their calibration over deserts a fixed AOT value of 0.2 (Red coloured line in figure).

Both options i.e. a montly variable AOT value following Govaerts and Clerici 2004 and a fixed AOT value following CNES are currently being evaluated (Up to now prototyping results have indicated no major difference, but aerosol issues will be further investigated in collaboration with Y. Govaerts).
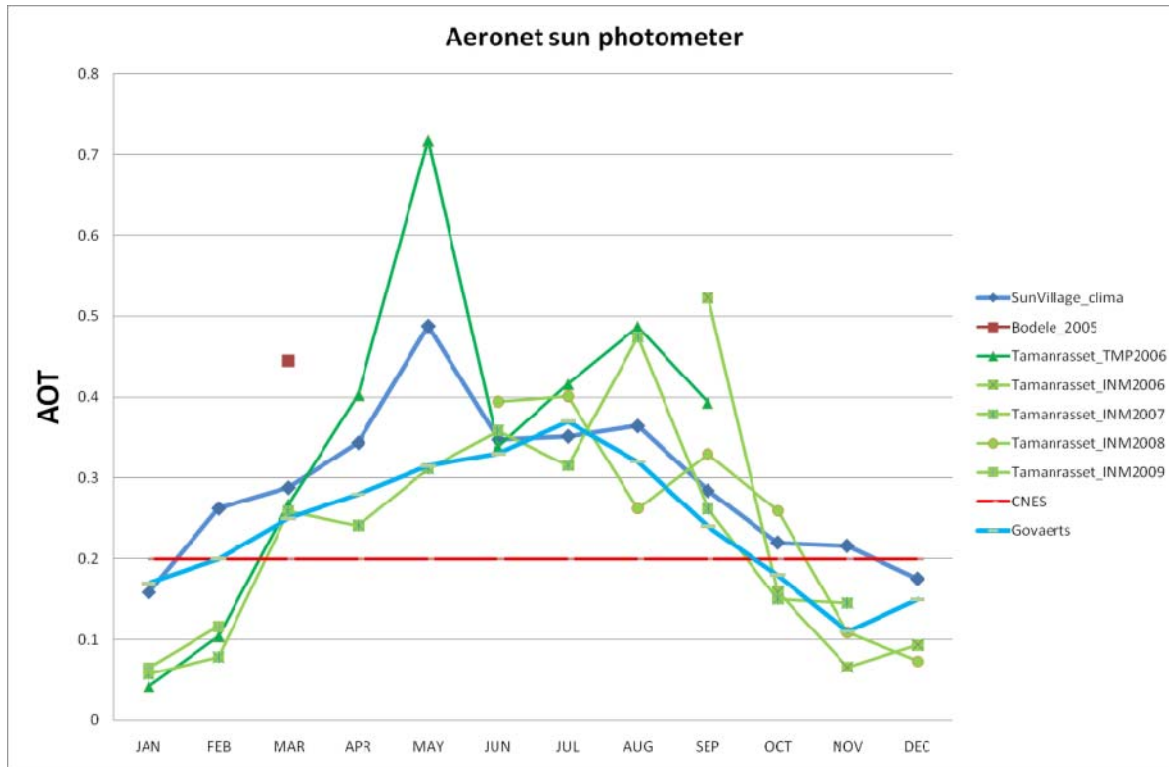

Figure 13: AOT seasonal variation

4.4.4.2.2 Calculation of measured TOA reflectance values

⇨ Conversion to DNs to TOA radiance L_{TOA}^{meas} by applying current calibration coefficients following Equation 4.

⇨ Conversion of TOA radiance L_{TOA}^{meas} to apparent TOA reflectance ρ_{TOA}^{meas} (Equation 8)

4.4.4.2.3 Cloud check

⇨ Conversion to DNs to TOA radiance L_{TOA}^{meas} by applying current calibration coefficients following Equation 4. The cloud masking is based on a threshold test, if one pixel in the ROI is cloudy, the whole ROI is discarded.

$$\text{if } (\rho_{TOA}^{meas,NIR} - \rho_{TOA}^{meas,blue}) < threshold * (\rho_{TOA}^{meas,NIR} + \rho_{TOA}^{meas,blue}) \text{ than pixel = cloudy.}$$

We only proceed with desert sites that are completely cloud-free. This is less complex and is justified as the desert sites are expected to be cloud-free for a sufficient large portion of the time.

4.4.4.2.4 Averaging over the ROI

All TOA reflectance values for all pixels in the ROI are averaged to get one single value for the ROI for each image. This is justified as the ROI is relatively small and homogeneous.

4.4.4.2.5 Check on VZA

As the uncertainty of the BRDF model increases with VZA, scenes obtained with a VZA larger than 30° are removed.

4.4.4.2.6 Comparison of TOA reflectance values

The TOA reflectance values as measured by the sensor ρ_{TOA}^{meas} can now be compared to the modelled values ρ_{TOA}^{model} for e   ach desert site.   A new estimate of the calibration coefficient for that site and day is then calculated as :

$$A^{new} = A^{old} \; \frac{\rho_{TOA}^{meas}}{\rho_{TOA}^{model}}$$

4.4.4.2.7 Outlier selection and daily averaging

A daily average is calculated by averaging the results obtained over the different sites after outlier removal. A site is removed if it is detected as an outlier in at least one of the spectral bands. A robust outlier selection procedure based on the median and standard deviation from the median is used for this (see also 4.6.2.2).

4.4.4.2.8 Seasonal correction

The absolute calibration approach as described above and applied to a large time series of SPOT-VGT data have shown a seasonal trend as depicted in Figure 23 for the RED band. This necessitates the use of a seasonal correction function to remove these unwanted seasonal artifacts. At least during the first year of PROBA-V this seasonal correction function will be based on the SPOT-VGT data analysis. A 4th degree polynomial function fits the seasonal variation well (black lines in figures for the different years) and is reasonable similar for the different years. An average 4th degree polynomial function (in function of day number) will be used for the seasonal correction.
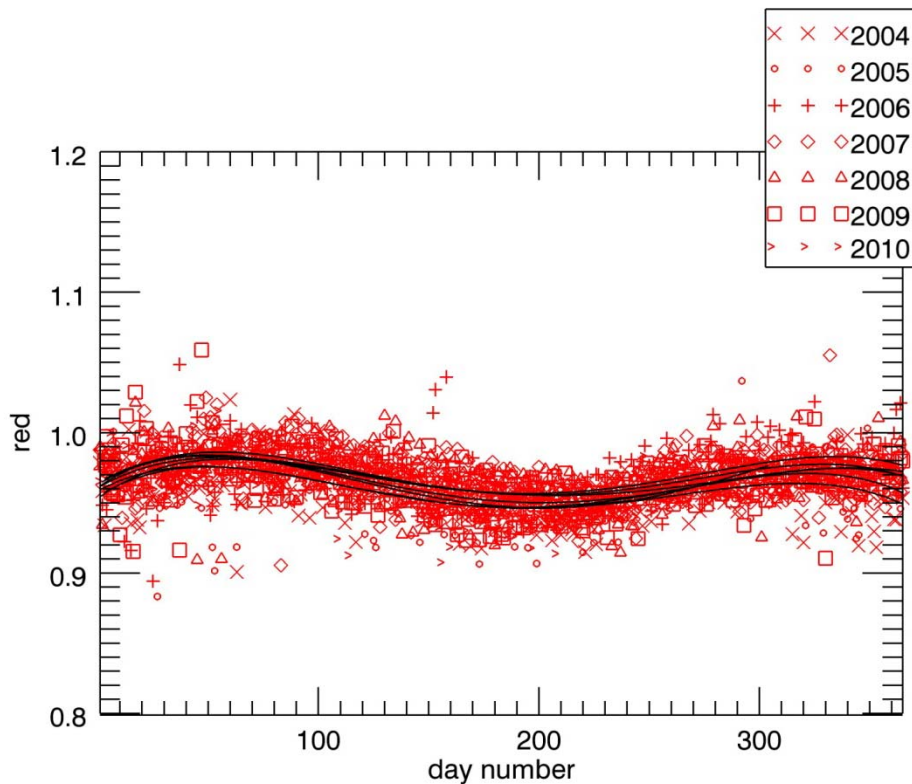
Figure 14: Seasonal variation of absolute calibration over stable deserts on the basis of SPOT-VGT2

4.4.4.3   Error sources

The determination of the calibration coefficient for individual ROIs pixels is affected by a number of variables, each of which is prone to random and/or systematic errors. The contributions to the errors come mainly from the following sources, which we will describe briefly:

Properties of the target: The BRDF surface properties of the desert sites are assumed to be constant over time. Even when maximally stable targets are selected, this assumption is only approximately true, therefore it is expected to contribute significantly to the errors.

Accuracy of the BRDF model: The BRDF model derived by Govaerts and Clerici 2004, [LIT1] dates from 2004 and has been compiled on the basis of inversion of satellite data (which have their own uncertainties) and other datasources available at that moment. The BRDF dataset contains therefore some intrinsic uncertainties. A BRDF data set with improved accuracy compiled on the basis of MODIS data may become available in the near future (personal communction Yves Govaerts).

Aerosol model: The standard 6SV desert aerosol is currently used. This model (i.e. its scattering, absorption ,asymmetry parameters) may deviate from the actual aerosol.

Aerosol optical thickness: Aerosol optical measurements in these deserts sites are rare and therefore assumptions have been made on the used AOT (i.e. monthly variable or fixed AOT) which may deviate from the actual aerosol optical thickness. It is expected that after averaging a lot of measurements over sites and over time, that the aerosol affect will be more a random error (noise) than a fixed bias/systematic error.

Radiative transfer code: The intrinsic uncertainty of the 6SV radiative transfer code may cause systematic uncertainties in the absolute calibration results.

Seasonal variation : The 4th degree seasonal polynomial correction function is derived on the basis of SPOT-VGT data analysis (only after at least one year of PROBA-V acquisitions, this can be replace by a PROBA-V derived function). Hereby it is assumed that the observed seasonal variation in the SPOT-VGT data analysis is only due to deserts related effects and not to the sensor itself. Furthermore, it is assumed that the seasonal variation pattern is similar over the years. Possible small violation of both assumptions will give rise to errors in the absolute calibration on the basis of stable deserts.

Uncertainties in ECMWF meteo information: About 5-10 mbars is a reasonable accuracy for the atmospheric pressure. An accuracy of about 10-20 mAtm-cm (Dobson Units, DU) is a typical accuracy for the total ozone amount of the atmosphere. An uncertainty of 20 % is often used for the water vapour content.

4.5   Relative radiometric calibration

4.5.1   Interband: Sun glint

4.5.1.1   Introduction

This method uses the specular reflection of the sun on the ocean surface. This sun glint reflection is high and spectrally flat and is used to transfer the absolute calibration of one reference band to other spectral bands (inter-band calibration) (Hagolle et al., 2004 [LIT27]; Fougnie et al, 2007 [LIT4]). The size of sun glint spot is variable as it depends on the ocean surface roughness which is controlled by wind speed. The range of angles from which the sun glint can be observed is larger for an agitated sea. The sun glint spot observed by a satellite at an altitude of 800 km often exceeds 100 km. The main advantage of the sun glint calibration approach is that it is one of the rare methods that can provide calibration of the SWIR band. Due to the chosen local time (around 10h30) of the descending node in the sun-synchronous orbit of PROBA-V, sun glint is always observed in eastern direction. It can only be observed by the eastern and middle looking cameras in normal operating mode (depending on location and day of the year) because their viewing direction is close to the exact specular direction. Observation of sunglint by the western looking camera is not possible without platform manoeuvres.

4.5.1.2   Algorithm

4.5.1.2.1   Physics of the algorithm

4.5.1.2.1.1   Conversion to TOA reflectance

See section 4.4.1.2.1.1

4.5.1.2.1.2   TOA reflectance signal decomposition

The TOA reflectance ρ_{TOA}^{c} corrected for gaseous transmittance, over oceans in specular (sun glint) conditions can be decomposed as (omitting spectral band and angles for simplicity):

$$\rho_{TOA}^{c} = \frac{\rho_{TOA}}{Tr_{gas}} = \rho_{path} + \rho_{spe} Tr_{tot,s} Tr_{tot,v} + \frac{\rho_{w} Tr_{tot,s} Tr_{tot,v}}{\left(1 - s\rho_{w}\right)}$$

Equation 32: Sun glint TOA reflectance

with

ρ_{spe}: the specular reflectance at the ocean surface, for the other terms see 4.4.1.2.1.2.

We ignore here the surface foam reflectance, which is negligible for surface wind speeds under 10 m/s (wind speed mask applied in processing). Compared to equation Equation 9 of section 4.4.1.2.1.2 Equation 32 includes explicitly the sun glint contribution.

For a flat sea surface (zero wind speed) the specular reflectance ρ_{spe} or directly reflected light can be computed 'exactly' using the Snell-Fresnel laws. For a rough sea surface, the reflection is conditioned by the wind and therefore the sun glint reflectance of the sea surface can only be described on statistical basis. Cox and Munk [LIT28] took many photographs of sun glitter patterns on the ocean surface under different conditions of wind speed/direction and sun angles. From these observations they derived an ocean wave slope probability distribution function (PDF) that can be described as a Gaussian curve plus higher-order skewness and kurtosis terms.

A first approximation of the Cox-Munk model uses an isotropic Gaussian slope distribution (isotropic rough surface, independent of wind-direction) to represent the oceanic wave slopes. Adopting this isotropic form, the probability of a spatial sample being contaminated by sun glint is given by :

$$P_{sg} = \frac{1}{\pi\sigma^2}\exp(-\frac{2(1+\cos(\theta_v)\cos(\theta_s)+\sin(\theta_v)\sin(\theta_s)\cos(\Lambda\phi))-(\cos(\theta_v)+\cos(\theta_s))^2}{\sigma^2(\cos(\theta_v)+\cos(\theta_s))^2}$$

where θ_S is the sun zenith angle (SZA) at the viewed spatial sample

θ_v is the view zenith angle (VZA) at the viewed spatial sample

$\Lambda\varphi$ is the relative azimuth angle (RAA) (sun azimuth angle (SAA)-view azimuth angle (VAA)) at the viewed spatial sample

σ^2 is the mean surface slope which is function of the wind speed ws

$\sigma^2 = 0.003 + 0.00512 ws$

This isotropic wave slope PDF is often used in remote sensing applications when wind direction is not accurately known or not uniform.

In 6SV the slope distribution is considered anisotropic: the distribution of the slope components depends on the wind direction. The wave slope PDF in 6SV is expressed with Gram-Charlier expressions as :

$$P_{sg}(Z'_x, Z'_y) = \frac{G_4(\xi,\eta)}{2\pi\sigma_c\sigma_u}\exp\left(-\frac{\xi^2+\eta^2}{2}\right)$$

with

ξ and η the normalized x and y slopes defined as

$$\xi = \frac{Z'_x}{\sigma_u}, \quad \eta = \frac{Z'_y}{\sigma_c}$$

σ_c and σ_u are the facet slope standard deviations in the crosswind and upwind :

$$\sigma_c^2 = 0.003 + 0.00192\cdot ws \pm 0.004, \quad \sigma_u^2 = 0.00316\cdot ws \pm 0.002$$

$G_4(\xi,\eta)$ the Gram-Charlier expansion :

$$G_4(\xi,\eta) = 1 - \frac{1}{2}c_{21}(\xi^2-1)\eta - \frac{1}{6}c_{03}(\eta^3-3\eta)$$
$$+\frac{1}{24}c_{40}(\xi^4-6\xi^2+3)+\frac{1}{4}c_{22}(\xi^2-1)(\eta^2-1)+\frac{1}{24}c_{04}(\eta^4-6\eta^2+3)$$

with c_{21} and c_{03} the skewness coefficients defined as

$c_{21} = 0.001 - 0.0086\,ws \pm 0.03$ and $c_{03} = 0.004 - 0.0033\cdot ws \pm 0.004$

and the kurtosis coefficients (c_{22}, c_{40}, c_{04}) are

$c_{40} = 0.40 \pm 0.23$, $c_{22} = 0.12 \pm 0.12$, $c_{04} = 0.23 \pm 0.41$

and

Z'_x and Z'_y are functions of Z_x and Z_y the crosswind and upwind directions of the slope (see Figure 15) given by

$$Z_x = \sin\alpha\tan\beta, \quad Z_y = \cos\alpha\tan\beta$$

α is facet azimuth angle (clockwise from the sun) and β is the facet zenith angle (tilt). Let χ be the wind direction in the local frame (related clockwise from the North by ϕ_w, then

$\chi = \phi_s - \phi_w$) and *ws* the wind speed in m/s (at a height of 10 m). If the sun system (*x,y*) is rotated through an angle χ to a new system (*x',y'*) related to the wind direction, then the facet slopes Z'_x and Z'_y in this wind system are

$$Z'_x = \sin \alpha' \tan \beta \ , \ Z'_y = \cos \alpha' \tan \beta \ , \ \alpha' = \alpha - \chi$$

therefore

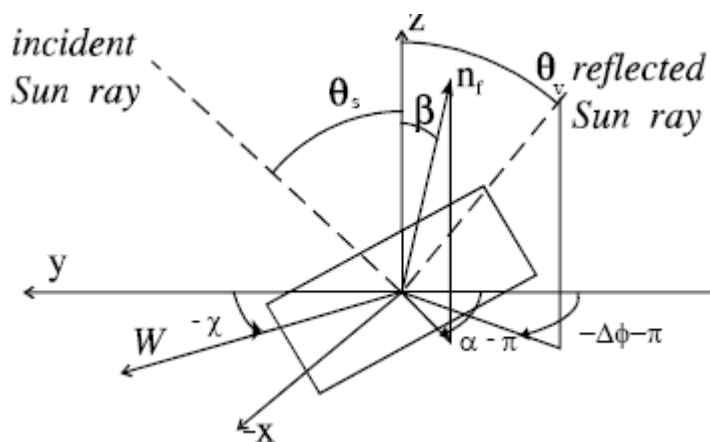$$Z'_x = \cos \chi \cdot Z_x + \sin \chi \cdot Z_y, \ Z'_y = \cos \chi \cdot Z_y - \sin \chi \cdot Z_x$$

Figure 15: Sun glint geometry

In Figure 15 θ_s is the sun zenith angle, θ_v is the view zenith angle, $\Lambda\varphi$ is the relative azimuth angle, α is facet azimuth angle, β is the facet zenith angle, W wind speed and $\chi = \phi_s - \phi_w$.

The uncertainties in the Cox and Munk parameters are quite large. For a windspeed of 10 m/s, the relative error or uncertainty in σ_c^2 and σ_u^2 is about 10% and 50 % for $c_{21}, c_{03}, c_{22}, c_{40}$. The most uncertain value is c_{04} which has an error of 200 %.

In order not to considerably complicate the sun glint calibration approach by including wind direction and because accurate information of wind direction just above the sea surface is often unavailable for the time of observation, it is decided to modify 6SV slightly by either taking the average ρ_{spe} obtained by looping over the wind azimuth from 0° and 360° or by replacing the PDF in 6SV by the isotropic formulation.

The sun glint (specular) reflectance is given by:

$$\rho_{spe} = \frac{\pi r(n,\theta_s,\theta_v,\phi_s,\phi_s)}{4\cos(\theta_s)\cos(\theta_v)\cos^4(\beta)} P_{sg}$$

Equation 33: Sun glint reflectance

where　　　　$r(n,\theta_s,\theta_v,\phi_s,\phi_s)$ is the Fresnel reflection coefficient (with *n* complex index of refraction of sea water)
β is the angle formed by the reflecting facet normal and the local normal defined by

$$\cos(\beta) = \frac{\cos(\theta_v) + \cos(\theta_s)}{\sqrt{2 + 2\cos(2\omega)}}$$

where ω is the specular reflection angle defined by

$$\cos(2\omega) = \cos(\theta_v)\cos(\theta_s) + \sin(\theta_v)\sin(\theta_s)\cos(\Lambda\phi)$$

The Fresnel reflection coefficient (r) describes the proportion of light hitting the surface that is reflected back. It can be calculated taking into account the refraction indices of sea water and air and the angles of incidence and refraction. In 6SV the fresnel reflectance is computed according to (Born & Wolf, 1975 [LIT29] taking into account both the real and imagery index of refraction. The refractive index of water varies with wavelength. In 6SV the complex index of refraction of sea water is deduced from the complex index of refraction of pure water, specified by Hale & Querry (1973) [LIT30].An additional correction of +0.006 is added to the real component due to the salinity and chlorinity of typical seawater. The small variation of the refraction index in function of the sea water temperature is neglected. In Table 15 the real and imagery part of the index of refraction are given for the PROBA-V wavelengths. Uncertainties in the index refraction are taken into account in the error budget (see section 4.5.1.3).

Band	nr (real component index of refraction)	nr (imagery component index of refraction)
BLUE	1.342	1E-09
RED	1.337	2.03E-08
NIR	1.335	2.68E-07
SWIR	1.323	8.55E-05

Table 15: Sea water index of refraction for the PROBA-V bands

4.5.1.2.1.3   Retrieval of the wind speed from the RED band

Because of the uncertainty on wind from ECMWF global models (typically 2 m/s on wind speed) and the error bars of the Cox and Munk model, there is an uncertainty in the determination of ρ_{spe}. Therefore the sun glint calibration approach can't be used with enough accuracy for absolute calibration of all bands. However it is adequate for inter-band calibration, using a well-calibrated band as reference band to derive the wind speed from the image pixel itself by comparing image data with simulated data.

The reference is preferably chosen between the bands that are calibrated with the Rayleigh calibration method, i.e. the BLUE and RED band. The RED band is the preferred reference band. In the BLUE ρ_{TOA}^c varies less with wind speed as there the relative contribution of ρ_{spe} to ρ_{TOA}^c is lower. Therefore wind speed retrieval from the data itself will work best with the RED band. More specifically, the wind speed will be derived based on a LUT of $\rho_{TOA}^c(RED)$ versus wind speed generated with 6SV (see section 4.5.1.2.2.1). The wind speed value for which the measured $\rho_{TOA}^{c,meas}(RED)$ agrees best with the modelled $\rho_{TOA}^{c,\text{model}}(RED)$ is selected

As described in the technical note on Sun Glint [PVDOC-611], due to the difference in viewing geometry between the different bands, especially between VNIR and SWIR detectors, the uncertainty in the Cox-Munk model is not fully cancelled for the case of PROBA-V. The uncertainty in the ratio of sun glint reflectances for two different relative azimuth angles $\rho_{sp}(RAA_{RED}) \big/ \rho_{sp}(RAA_{SWIR})$ introduces still an error in the interband sun glint calibration approach (see section 4.5.1.3)..

4.5.1.2.1.4   Retrieval of the calibration coefficients for the BLUE, NIR and SWIR bands

Once the wind speed has been determined from the observations in the RED band, this wind speed value is then used to model, with 6SV,

$$\rho_{TOA}^{c,\text{model}}(BLUE), \rho_{TOA}^{c,\text{model}}(NIR), \rho_{TOA}^{c,\text{model}}(SWIR).$$

The change in calibration coefficients for the Blue, NIR, SWIR is then calculated as :

$$\Lambda A^{BLUE} = \frac{A_{BLUE}^{new}}{A_{BLUE}^{old}} = \frac{\rho_{TOA}^{c,meas}(BLUE)}{\rho_{TOA}^{c,\text{model}}(BLUE)}$$

$$\Lambda A^{NIR} = \frac{A_{NIR}^{new}}{A_{NIR}^{old}} = \frac{\rho_{TOA}^{c,meas}(NIR)}{\rho_{TOA}^{c,\text{model}}(NIR)};$$

$$\Lambda A^{SWIR} = \frac{A_{SWIR}^{new}}{A_{SWIR}^{old}} = \frac{\rho_{TOA}^{c,meas}(SWIR)}{\rho_{TOA}^{c,\text{model}}(SWIR)}$$

4.5.1.2.2   Algorithm implementation

4.5.1.2.2.1   Generation of LUTs

For the generation of the LUTs 6SV is used. 6SV takes into account coupling effect between ocean and atmosphere (including Cox Munk model), polarization and multiple-scatttering which are necessary to accurately calculate $\rho_{TOA}^{c,\text{model}}$. To calculate these LUTs of $\rho_{TOA}^{c,\text{model}}$ the following parameter settings are used:

- the aerosol model and aerosol optical thickness are fixed. The Shettle and Fenn Maritime aerosol with 98% humidity (denoted as M98, see section 4.4.1.2.1.3) is used with a fixed AOT of 0.08 at 850 nm. The spectral dependency of AOT ($\lambda^{-\alpha}$)for the M98 aerosol, expressed by the angstrom coefficient *a*, is 0.1. This results in an AOT of approximately 0.0836 at 550 nm (which is the wavelength to express AOT in 6SV). Sensitivity studies by Hagolle et al (2004) [LIT27] have shown that for this aerosol model the calibration method is quite tolerant to a bad knowledge of AOT. To discard observation with too high aerosol loading or an aerosol type very different from M98, the MODIS Terra Aerosol Products (or equivalent sensor if MODIS is not available) will be checked, containing both AOT and aerosol size distribution. The local equatorial crossing time of the Terra satellite is approximately 10:30, which is very close to the PROBA-V overpass.

- The water leaving reflectance ρ_w will be modelled in 6SV in function of chlorophyll concentration according to the Morel bio-optical model. As the same oligotrophic sites (see Table 6) as used for the Rayleigh calibration are selected for the sun glint calibration, also the same monthly mean chlorophyll concentration will be used. Same sites are used to minimize the uncertainty in chlorophyll concentration. Furthermore by taking monthly average values errors due to seasonal chlorophyll variations are minimized.

For the different PROBA-V bands LUTS are created for the apparent TOA reflectance, corrected for gaseous transmittance for an atmosphere bounded by fresnel reflecting wind roughened oceanic surface with a chlorophyll concentration taken from
. These LUTs are a function of sun zenith angle, view zenith angle, relative azimuth angle and windspeed.

Two options for the generation of the LUTs with 6SV are considered: (a) a global pre-calculated LUT and (b) an *on-the-fly* calculated LUT. The global LUT will be valid for all imagery and contains ρ_{TOA}^{c} for a variety of sun-view geometries. The *on-the-fly* calculated LUT is much smaller and only valid for the image under consideration.

4.5.1.2.2.2 Processing steps

⇨ Conversion to DNs to TOA radiance L_{TOA}^{meas} by applying current calibration coefficients following Equation 4.

⇨ Conversion of TOA radiance L_{TOA}^{meas} to apparent TOA reflectance ρ_{TOA}^{meas} (Equation 8)

⇨ Correct for the gaseous absorption (conversion of ρ_{TOA}^{meas} to $\rho_{TOA}^{c,meas}$) based on predefined exponential variation of gaseous transmittance with airmass and gaseous amount for each band (SMAC approach).

⇨ Visual cloud screening: A visual cloud inspection is considered to give higher performance than an automatic cloud detection. It the sun glint spot is cloudy, the sun glint scene not be used

⇨ White caps masking: Remove all pixels, probably contaminated by surface white caps based on wind speed threshold (5 m/s) (derived from the nearest meteo data)

⇨ Sun glint test: Automatically select sunglint spot based on a wave angle threshold θn. All pixels for which θn < 4° are kept with θn defined as :

$$\theta_n = ar\cos\left(\frac{\cos\theta_s + \cos\theta_v}{2\cos\left(\frac{\theta_p}{2}\right)}\right) \text{ with } \theta_p = ar\cos(\cos\theta_s\cos\theta_v + \sin\theta_s\sin\theta_v\cos\Lambda\phi)$$

⇨ Homogeneity test : remove pixels with large local variation as this may be due to the presence of some clouds not detected by the visual cloud screening algorithm : remove pixels for which stdev($\rho_{TOA}^{c,NIR}(5x5\,pixels)) \geq 0.1 * avg(\rho_{TOA}^{c,NIR})$. An extra test based on the raito of $\dfrac{\rho_{TOA}^{c,SWIR}}{\rho_{TOA}^{c,NIR}}$ used for SPOT-VGT to indicate the presence of undetected clouds is not applicable for PROBA-V as due to the view angle differences between VNIR and SWIR the specular reflectance ratio is signifcantly different from one even for uncloudy conditions.

⇨ NIR reflectance test: remove all pixels for which $\rho_{TOA}^{c,NIR} < 0.2$ to select only those pixels for which the sun glint reflectance is high enough to minimize perturbations linked to ocean surface or atmospheric effects;
Wind speed estimation : Use global LUT of $\rho_{TOA}^{c,k}$ or on-the-fly calculated LUT of $\rho_{TOA}^{c,k}$ in function of wind speed VZA, SZA,RAA for the chlorophyll concentration taken from

⇨ and parameter ranges valid for the selected pixels. For all LUTS AOT is fixed at 0.08 and M98 aerosl is used. For each pixel find windspeed (ws^{est}): the simulated $\rho_{TOA}^{c,\mathrm{model}}(RED)$ (in the global LUT or the on-the-fly calculated LUT) are interpolated on the angles from each pixel to obtain $\rho_{TOA}^{c,\mathrm{model}}(RED)$ corresponding to the geometry of the observation. Then $\rho_{TOA}^{c,\mathrm{model}}(RED, ws_i)$ and $\rho_{TOA}^{c,\mathrm{model}}(RED, ws_{i+1})$ that surround $\rho_{TOA}^{c,meas}(RED)$ are found and assuming a linear relationship the wind speed (ws) corresponding to $\rho_{TOA}^{c,meas}(RED)$ is estimated.

⇨ For each pixel find $\rho_{TOA}^{c,\mathrm{mod}el}(Blue, NIR, SWIR)$ corresponding to ws^{est} : $\rho_{TOA}^{c,\mathrm{mod}el}(Blue, NIR, SWIR, ws)$ is derived from a linear interpolation between $\rho_{TOA}^{c,\mathrm{mod}el}(Blue, NIR, SWIR, ws_i)$ and $\rho_{TOA}^{c,\mathrm{mod}el}(Blue, NIR, SWIR, ws_{i+1})$ at the estimated wind speed ws^{est}

⇨ Calculate for each pixel the change in calibration coefficients for the Blue, NIR, SWIR as :

$$\Lambda A^{BLUE} = \frac{A_{BLUE}^{new}}{A_{BLUE}^{old}} = \frac{\rho_{TOA}^{c,meas}(BLUE)}{\rho_{TOA}^{c,\mathrm{mod}el}(BLUE)} ; \Lambda A^{NIR} = \frac{A_{NIR}^{new}}{A_{NIR}^{old}} = \frac{\rho_{TOA}^{c,meas}(NIR)}{\rho_{TOA}^{c,\mathrm{mod}el}(NIR)} ;$$

$$\Lambda A^{SWIR} = \frac{A_{SWIR}^{new}}{A_{SWIR}^{old}} = \frac{\rho_{TOA}^{c,meas}(SWIR)}{\rho_{TOA}^{c,\mathrm{mod}el}(SWIR)}$$

⇨ Discard scenes for which MODIS Terra (if available after 2012) AOT is higher than 0.15 and angstrom exponent is higher than 0.3

4.5.1.2.2.3   Required ancillary data

Some exogenous data are required to accurately calculate $\rho_{TOA}^{c,\mathrm{mod}el}$, to correct ρ_{TOA}^{meas} for gaseous transmittance or in the masking processing steps. These are :

⇨ Wind speed at sea level to mask white caps: this parameter can be obtained from ECMWF with an accuracy of about 2 m/s
⇨ Total ozone amount to calculate the ozone absorption: this parameter can be retrieved from ECMWF or TOMS with an accuracy of 10-20 mAtm-cm
⇨ The water vapour content obtained from ECMWF
⇨ MODIS Terra Aerosol product   (or equivalent if not available e.g. MERIS)

Other 'internal' ancillary data (assumed attached to the input image) : time, date, sun zenith angles, solar zenith angles, relative azimuth angles, cloud mask (calculated from the image)
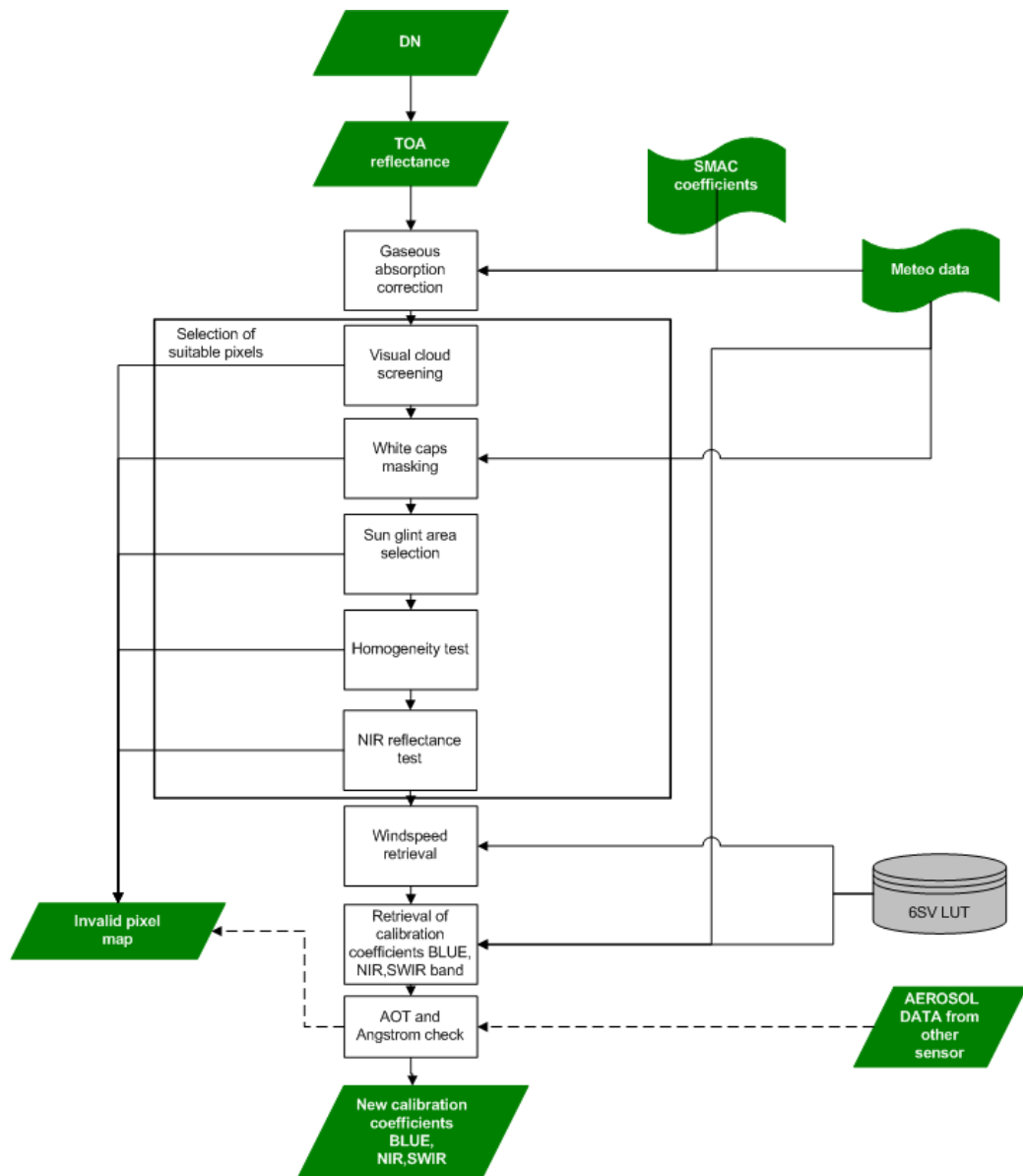
4.5.1.2.2.4 Summary of the processing steps

Figure 16: Overview Flowchart DCC

4.5.1.3 Error analysis

In Hagolle et al. (2004) [LIT27] a detailed error analysis has been performed for absolute calibration of SPOT-Vegetation using the sun glint calibration method.

The considered error sources are :

1) absolute calibration error in the reference RED band. When considering absolute aspects, i.e., to propagate the absolute calibration to the other bands, the calibration error of the reference band should be considered. The RED band is assumed to be calibrated with an accuracy of 3 %

2) atmospheric pressure: an error of 15 hpa is considered

3) sea water refraction index: this directly effects the sun glint reflectance through Equation 33. It varies slightly with salinity and temperature. Especially for SWIR wavelengths there still exists some uncertainty in the value of the sea water refraction index. An

uncertainty of 0.3% in this parameter is assumed for the SWIR band and 0.1% for the other bands

4) chlorophyll content: as the water leaving reflectance is directly calculated from the chlorophyll content an error in the chlorophyll content affects the reflectance in the BLUE and RED bands. For NIR and SWIR bands the water leaving reflectance is 0 (independent of chlorophyll) for deep oligotrophic oceans. For the BLUE end RED bands an uncertainty in the water leaving reflectance of 20% is taken into account the error budget.

5) Aerosol model and content. The error budgets in Hagolle et al. (2004) [LIT27] is made assuming that C70 cases and cases with high AOT are discarded

6) Gaseous transmittance: An error in the ozone amount and water vapor of respectively 5% and 20% is used in the error budget

7) Polarization sensitivity : Errors due to polarization differences between bands were considered by Hagolle et al. (2004) [LIT27] for SPOT-VGT, however they can be neglected in the case of PROBA-V due to low polarization sensitivity in the different bands.

8) Specific for PROBA-V: The relative uncertainty in the Cox-Munk model. This uncertainty should not be taking into account for sensors with the same viewing geometry for all bands like SPOT-VGT. It is however an error that has to be taken into account for PROBA-V due to the difference in viewing angles, especially in azimuth angles between the VNIR and SWIR bands. A detailed analysis can be found in the technical note on sun glint [PVDOC-611]. A 5% relative uncertainty is considered in this study.

The linear interpolation that will be needed to intermediate between the entries of the lookup tables should not introduce significant errors, provided that each entry of the lookup tables has been adequately sampled (2° for θs and θv, and 5° for $\Delta\varphi$, 0.5 m/s for wind speed, TBC).

In Table 16 the error budget is given for the sun glint method (partly taken from Hagolle et al. (2004) [LIT27]). Errors are 3σ values expressed in percent. The error sources are supposed to be non corelated and thus the total error is the quadratic sum of all errors. As the spectral response curves of PROBA-V are almost identical to those of SPOT-VGT, errors in the sun glint calibration introduced by most of the uncertain parameters will be similar. Once the exact spectral response curves for PROBA-V are defined, this error budget will be re-evaluated.

In section 0 it is explained how the uncertainty calculation is used in the determining the final error budget of the vicarious calibration.

Error Sources	BLUE	NIR	SWIR
calibration error 3% in RED band	1.7	3.2	3.3
Water reflectance	2	0.1	0.1
uncertainty sea water refraction index	0.3	0.6	2
ozone (5%)	0.3	0.5	0.3
water vapor (20 %)	0.1	0.8	0.1
Aerosols	1.5	1	2
5% relative uncertainty Cox-Munk	0	0	5
Total	**3.1**	**3.5**	**6.6**

Table 16: Summary of sun glint absolute calibration error budget

4.5.2   Interband: deep convective clouds

4.5.2.1   Introduction

This approach (Lafrance, et al., 2002 [LIT31]; Henry and Meygret, 2001 [LIT32]; Sohn et al., 2009 [LIT33]) makes use of large, bright, thick, high altitude, convective clouds over oceanic sites, called deep convective clouds (DCC). Their reflective properties are spectrally flat in visible and near-infrared and the only significant contributions to the observed signal are from the cloud reflectance, molecular scattering and ozone absorption which can be modelled with RTF. Using the RED band as reference the BLUE and NIR band can be inter-calibrated. The method is not suited for the SWIR band as the reflectance is no longer invariant over this spectral region.

4.5.2.2   Algorithm

4.5.2.2.1.1   Conversion to TOA reflectance

See section 4.4.1.2.1.1.

4.5.2.2.1.2   TOA reflectance signal decomposition

The TOA reflectance of deep convective clouds (DCC) over oceans can be decomposed as :

$$\rho_{TOA} = Tr_{gas} \cdot \rho_c \left(\tau_c^n + \tau_a^n + \tau_r^n \right)$$

with Tr_{gas} the total gaseous transmittance, ρ_c the reflectance at the top of the cloud/atmosphere system and τ_c^n, τ_a^n, τ_r^n respectively the clouds, aerosol and rayleigh optical thickness in the different atmospheric layers.

DCC clouds are good bright calibration targets as they have a predictable reflectance. The amount of cloud reflectance at the top of the atmosphere is reduced due to ozone absorption. DCC are at the tropopause level and hence effects of water vapor and tropospheric aerosol absorption are minimized. After correction of the ozone absorption DCC have almost a perfect white spectral behaviour in VNIR bands and therefore the reflectance in one band can be extrapolated to an other band to evaluate the accuracy of interband calibration coefficients. For PROBA-V , we will implement a refinement of this method proposed by Lafrance et al. (2002) [LIT31] where TOA reflectance over these clouds are modelled using radiative transfer calculations (RTC). This makes it possible to take into account small spectral dependencies in the TOA cloud reflectance.
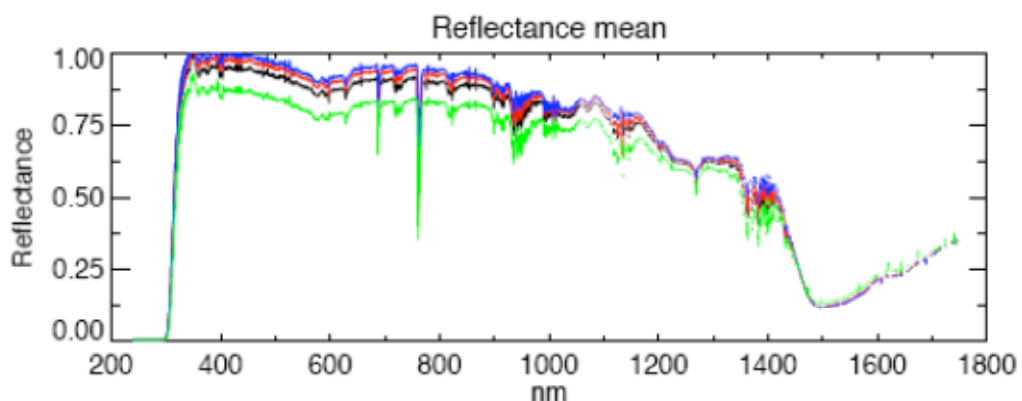

Figure 17: SCIAMACHY TOA reflectance spectra over DCC

The data used in Figure 17 has not been corrected for gaseous absorption, and has been prepared at SCIAMACHY (courtesy of Dave Doelling).

4.5.2.2.1.3　Retrieval of the cloud optical thickness from the RED band

Because of the uncertainty in the absolute values of the TOA reflectance over DCC (see variation in Figure 17) due to variations of cloud optical thickness τ_c, DCC can't be used for absolute calibration . However due to the almost flat spectral signature DCC are adequate for inter-band calibration , using a well-calibrated band as reference band to derive the cloud optical thickness τ_c from the image pixel itself by comparing image data with simulated data. The cloud reflectance in the non-absorbing VNIR bands is mainly sensitive to the cloud optical thickness (Figure 18), while in the absorbing SWIR bands it is more sensitive to the droplet effective radius (Figure 16).
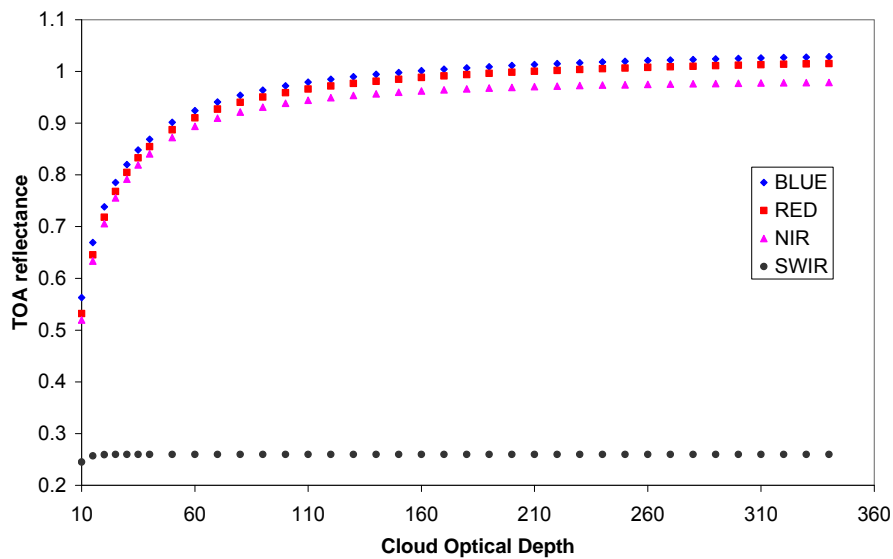

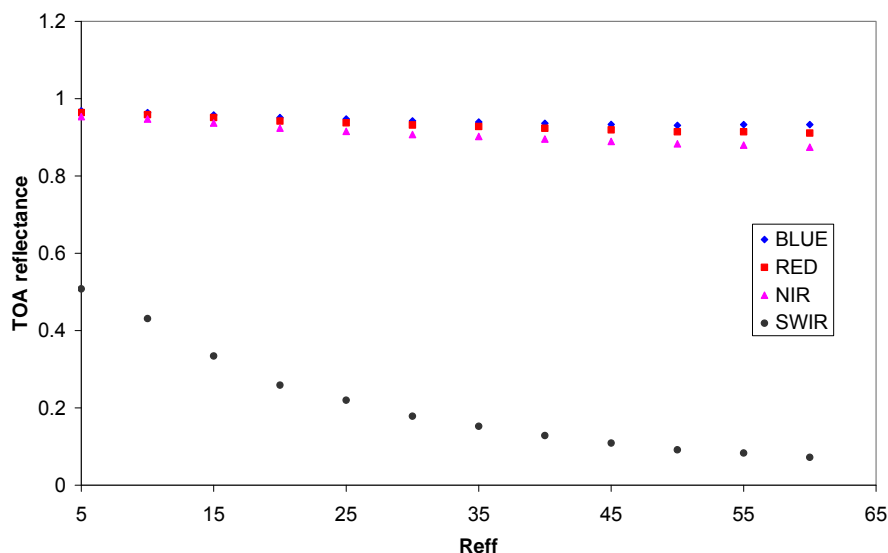**Figure 18: DCC TOA reflectance for in function of cloud optical depth.**

Figure 19: DCC TOA reflectance in function of cloud effective radius.

Figure 18 and Figure 19 have been calculated for SZA=0°, SAA=40°, VZA=40° and VAA=30°. In Figure 18 a cloud effective radius of 20 μm is assumed. For Figure 19 a cloud optical depth of 80 is used.

The method uses the TOA reflectance in the RED band corrected for ozone absorption to derive the cloud optical thickness by inversion of a LUT of TOA reflectance in function of cloud optical thickness assuming a fixed ice particle model.

4.5.2.2.1.4   Retrieval of the calibration coefficients for the BLUE and NIR bands

The cloud optical thickness estimated from the RED band is then used to model the TOA reflectance in the other bands ($\rho_{TOA}^{c,\text{mod}el}(BLUE), \rho_{TOA}^{c,\text{mod}el}(NIR)$) through a radiative transfer LUT.

The change in calibration coefficients for the Blue and NIR band is then calculated as :

$$\Lambda A^{BLUE} = \frac{A_{BLUE}^{new}}{A_{BLUE}^{old}} = \frac{\rho_{TOA}^{c,meas}(BLUE)}{\rho_{TOA}^{c,\text{mod}el}(BLUE)} \; ; \Lambda A^{NIR} = \frac{A_{NIR}^{new}}{A_{NIR}^{old}} = \frac{\rho_{TOA}^{c,meas}(NIR)}{\rho_{TOA}^{c,\text{mod}el}(NIR)}$$

4.5.2.2.2   Algorithm implementation

4.5.2.2.2.1   Generation of LUTs

The generation of LUTs of TOA reflectance above Deep Convective Clouds is performed with LibRadtran RTC. LibRadtran has been successfully validated in several model intercomparison campaigns and by direct comparison with observations. LibRadtran takes into account cloud phase, micro-physical properties as well as a complete description of the background atmosphere and surface. Both water and ice clouds models are included. The microphysical properties of water clouds are converted to optical properties either according to the Hu and Stamnes (1993) [LIT34] parameterization or by Mie calculations. For the optical properties of ice clouds calculations from Baum et al. (2005) [LIT35] are used.

Table 17 gives the properties of the cloudy atmosphere and the surface that are used to create the LUTs with LibRadtran. For the on-the-fly calculated LUT the minimal and maximal values of the angles are determined from the image itself.

The four most common ice crystals shapes are: bullet rosettes, aggregates, hollow columns, and plates. Each particle type is characterized by its single scattering albedo, the extinction cross-section and the scattering phase function which determine the interaction of light with the cloud particle. As a result, for a given cloud optical thickness and sun/viewing geometry the LUT will therefore depend on the microphysical properties of the ice particles. The ice particle model from Baum et al. (2005) [LIT35] is used to create the LUTs. The Baum model is also employed in the MODIS operational ice cloud optical depth retrieval (Zhang et al.,2009 [LIT36]) and by Sohn et al. (2009) [LIT33] for calibration over DCC. The Baum model is based on the use of in-situ observations of ice particle sizes and habits to compute optical properties for a realistic ensemble of theoretical particles (Figure 20: Mixing scheme according to Baum et al (2005) [LIT35]).

As cloud reflectance for the VNIR bands is rather insensitive to the effective particle radius, the effective radius is assumed fixed for the calibration. According to Sohn et al. 2009 [LIT33] MODIS effective particle radii for DCCs from one month of data show a narrow distribution with maximum frequency at 20 μm. LUT calculations will be performed for an effective radius of 20 μm.
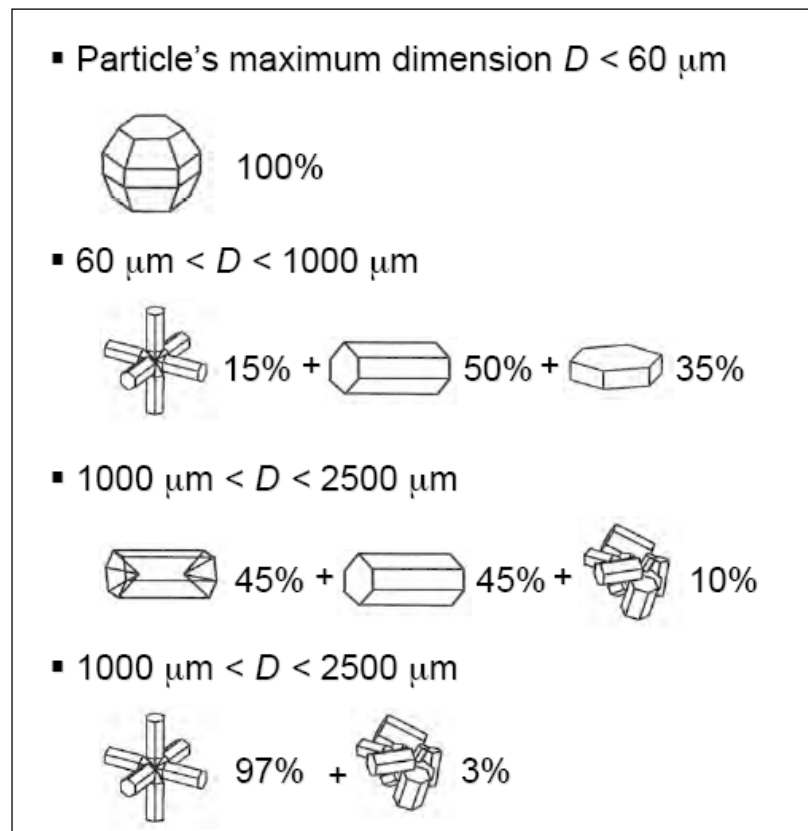
Figure 20: Mixing scheme according to Baum et al (2005)

As deep convective clouds are usually thicker than 10km, the cloud-top and cloudbase heights are assumed to be 15 km and 1 km, respectively (Sohn et al., 2009) [LIT33].

To calculate the Rayleigh scattering the pressure profiles from the tropical profile are used. Gaseous absorption is not taking into account in the LUT calculations as PROBA-V measurements will be corrected for ozone absorption

The ocean reflectance is assumed lambertian with a chlorophyll content of 0.1 mg/m³.

Parameter	LUT
Atmospheric profile	Tropical profile
Aerosol Model (from 0 to 2 km)	Maritime profile
Stratospheric aerosol	Background aerosols
Solar irradiance file	Taken from 6SV
Aerosol Optical depth	0.08
Gaseous absorption	No molecular absorption
Solar zenith angles	From 10° to 40°
View zenith angles	From 0° to 30° °
Relative azimuth angles	From 0° to 180°
Surface albedo (ocean)	BLUE: 0.02; RED: 0.002; NIR: 0 (lambertian)
RTF solver	DISORT2
Cloud optical depth	20 values from 40 to 200 (logaritmically scaled)
Ice particle radius	20 μm
Ice cloud optical properties	Baum detailed
Location ice cloud	From 1 to 15 km
Water cloud layer	NO
Location water cloud	N/A
Water cloud optical properties	N/A

Table 17: Properties of the cloudy atmosphere and surface for DCC LUTs

4.5.2.2.2.2 Processing steps

Conversion to TOA reflectance ρ_{TOA}^k

- ⇨ convert the raw DNs of the clouds calibration image to TOA radiance, following Equation 4
- ⇨ convert TOA radiance to apparent TOA reflectance, following Equation 8

Correction for gaseous absorption

- ⇨ Correct for the gaseous transmittance of O_3 (conversion of ρ_{TOA} to $\rho_{TOA}^{c,meas}$) based on predefined exponential variation with airmass and ozone content from ECMWF or TOMS data or climatology. The LUTs of TOA reflectance are calculated without gaseous absorption, therefore the PROBA-V measurements have to be corrected for gaseous absorption. As for convective clouds observations water vapour and oxygen gases lie below the cloud level, their absorption can be neglected. The ozone layer is however located mainly above the clouds and therefore ozone absorption can't be neglected.

Automatical selection of suitable clouds for deep convective clouds calibration (DCC)

- ⇨ Suitable deep convective clouds develop over subtropical warm oceans in inter-tropical latitudes between 30°N and 30°S. In PROBA-V Calibration Plan [PVDOC-615] three zones based on experience with SPOT-VGT and personal discussions with Dave Doelling (NASA, expert in DCC) are selected for daily acquisition remove all pixels

for which solar zenith angles > 40° or viewing zenith angles > 30° to avoid possible shadowing effects

⇨ use only pixels for which relative azimuth is between 30 and 150° to reject observations corresponding to viewing geometries near the specular direction.

⇨ remove all pixels for which $\rho_{TOA}^{NIR,c} < 0.8$ (cloud threshold) to ensure that thick clouds are selected

⇨ remove all pixels for which $\text{RMSE}(\rho_{TOA}^{NIR,c}(N_p x N_p)/\rho^{NIR,c}) > 0.03$ to select only homogenous clouds (the exact size expressed in number of pixels shall be evaluated during commissioning phase based on real PROBA-V data over DCC)

⇨ remove central pixels if $\rho_{TOA}^{NIR,c}(N_p x N_p) notall > 0.8$ to select only pixels with cloudy backgrounds

Retrieval op Cloud optical thickness

⇨ For each pixel the cloud optical thickness(τ_c^{est}): the simulated $\rho_{TOA}^{c,model}(RED)$ (in the global LUT or the on-the-fly calculated LUT) are interpolated on the angles from each pixel to obtain $\rho_{TOA}^{c,model}(RED)$ corresponding to the geometry of the observation. Then $\rho_{TOA}^{c,model}(RED,\tau_{c,i})$ and $\rho_{TOA}^{c,model}(RED,\tau_{c,i+1})$ that surround $\rho_{TOA}^{c,meas}(RED)$ are found and assuming a linear relationship the cloud optical thickness(τ_c^{est}) corresponding to $\rho_{TOA}^{c,meas}(RED)$ is estimated.

Calculate ΛA^{BLUE} and ΛA^{NIR}

⇨ For each pixel find $\rho_{TOA}^{c,model}(Blue, NIR)$ corresponding to τ_c^{est} : $\rho_{TOA}^{c,model}(Blue, NIR, \tau_c^{est})$ is derived from a linear interpolation between $\rho_{TOA}^{c,model}(Blue, NIR, \tau_i)$ and $\rho_{TOA}^{c,model}(Blue, NIR, \tau_{i+1})$ at the estimated cloud optical thickness(τ_c^{est})

⇨ Calculate for each pixel the change in calibration coefficients for the BLUE and NIR bands as :

$$\Lambda A^{BLUE} = \frac{A_{BLUE}^{new}}{A_{BLUE}^{old}} = \frac{\rho_{TOA}^{c,meas}(BLUE)}{\rho_{TOA}^{c,model}(BLUE)} ; \Lambda A^{NIR} = \frac{A_{NIR}^{new}}{A_{NIR}^{old}} = \frac{\rho_{TOA}^{c,meas}(NIR)}{\rho_{TOA}^{c,model}(NIR)}$$

4.5.2.2.2.3 Required ancillary data

The only 'external' ancillary data needed in the processing are the total ozone amount to calculate the ozone absorption and MODIS Terra Temperature images (or equivalent sensor if MODIS not available) for proper cloud selection.

Other 'internal' ancillary data (assumed attached to the input image) : time, date, sun zenith angles, solar zenith angles and relative azimuth angles.

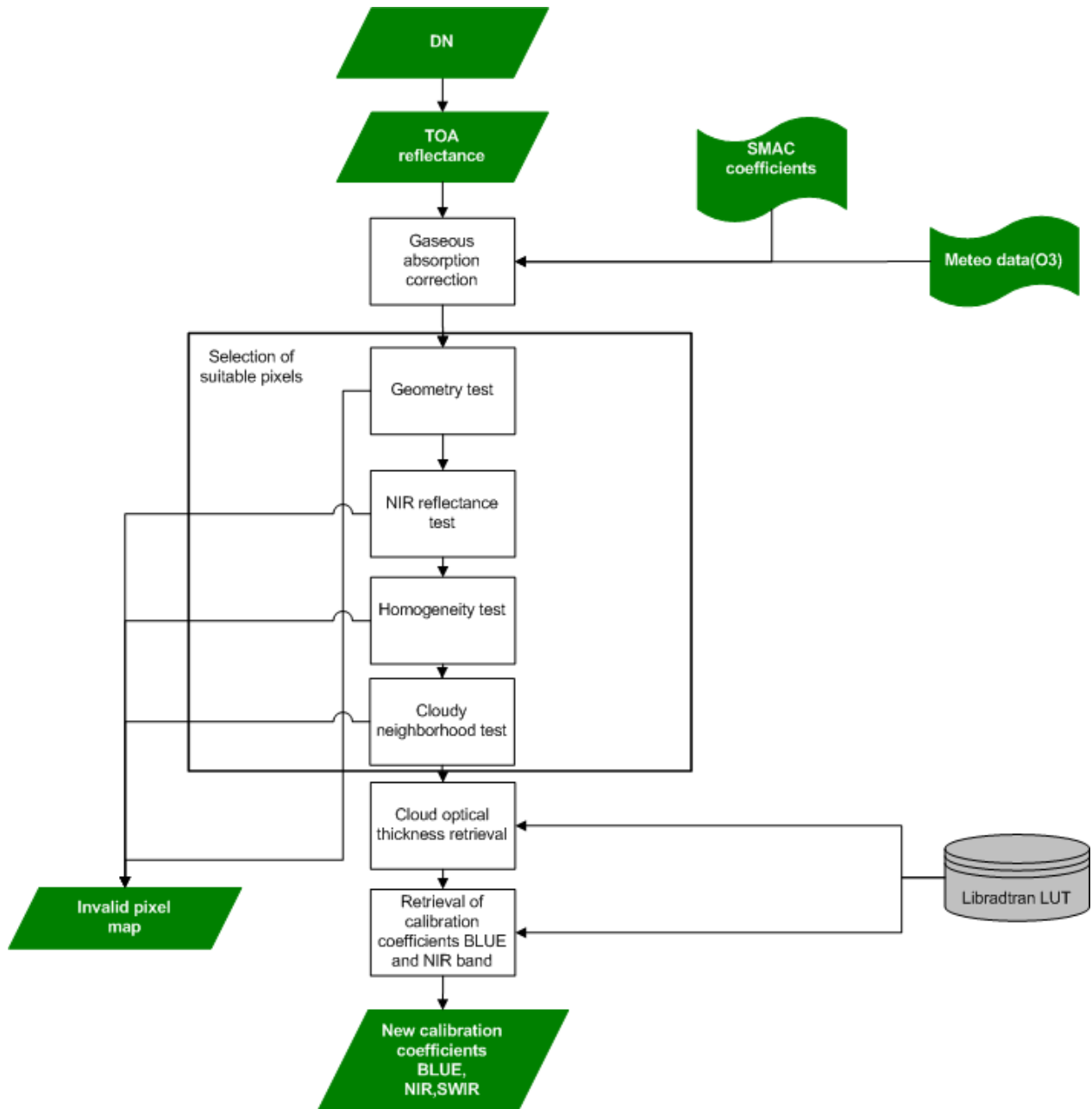#### 4.5.2.2.2.4   Summary of the processing steps

Figure 21: Flowchart DCC calibration

4.5.2.3   Error analysis

The error sources are :

1. Cloud effective radius: an error of 10 μm is considered in the error analysis

2. Microphysical properties model: Baum mixture of particles compared to pure crystal shape clouds such as plates, hexagonal column, hexagonal crystals. Calibration is performed with the Baum mixture of particles which may differ from the real microphysical model The degree to which the calibration coefficient is dependant on the model was estimated by carrying out the calibration process with a LUT calculated with the Baum mixture on an artificial image generated using the plates model .

3. Cloud top height: the uncertainty in the cloud altitude leads to an uncertainty of the Rayleigh scattering contribution above the clouds. In the error analysis a 3 km error in cloud top altitude is considered.

4. Cloud geometrical depth: an uncertainty of 4 km in the cloud geometrical depth is used for the error analysis

5. Ozone: an error of 20 % in the ozone concentration is considered in the sensitivity analysis

6. Atmospheric profile: uncertainties are assessed by using a mid-latitude summer profile instead of the tropical profile

The error analysis is performed by using a LUT generated according to the specifications in Table 17. This LUT is then used to perform a DCC calibration on an artificial image generated according to the same specification except for the parameter of interest (e.g. for case 1 cloud effective radius: images were created with a cloud effective radius of 10 μm and 30 μm instead of 20 μm). In the error analysis we considered four different view zenith angles (0°, 10°, 20°, 30°), six cloud optical thickness values (50, 60, 70, 80, 100, 120) and four different sun zenith angles (0°, 10°, 20°, 30°).

Table 18 gives both the relative (interband) error budget and the absolute error for the DCC method for both BLUE and NIR band. The table contains the average error, the error at 1-sigma and at 2-sigma The error sources are assumed to be non-correlated and thus the total error is the quadratic sum of all errors. For the absolute error the uncertainty in the RED band calibration is also considered.

Error Sources	BLUE			NIR		
	average error (%)	1-sigma error (%)	2-sigma error (%)	average error (%)	1-sigma error (%)	2-sigma error (%)
Cloud effective radius (10 μm)	0.300	0.531	0.761	0.886	1.124	1.363
Microphysical model	0.218	0.358	0.499	0.758	0.984	1.210
Cloud top height	0.095	0.133	0.172	0.011	0.018	0.024
Cloud geometrical depth	0.040	0.043	0.046	0.002	0.004	0.005
Ozone (20%)	0.359	0.379	0.399	0.397	0.429	0.460
Atmospheric profile	0.003	0.005	0.006	0.001	0.002	0.003
Red calibration error (3%)	*2.912*	*2.929*	*2.945*	*2.704*	*2.882*	*3.061*
Total interband	**0.526**	**0.757**	**1.009**	**1.231**	**1.554**	**1.880**
Total absolute	*2.959*	*3.025*	*3.113*	*2.971*	*3.275*	*3.592*

Table 18: Calibration error budget for DCC

The method inaccuracy is mostly due to uncertainty in the cloud effective radius, the microphysical properties model and ozone content. The other uncertain parameters have only a very small effect on the accuracy of the DCC calibration method. Interband calibration can be performed over DCC with an accuracy of 1% (2-sigma) for the BLUE band and better than 2% for the RED band.

In section 0 it is explained how the uncertainty calculation is used in the determining the final error budget.

4.5.3   Multi-temporal Calibration over stable deserts

The goal of multi-temporal calibration is to monitor the stability and variations of the sensors responses over time. This results in information about the long-term behaviour of the sensor which can be compared with the temporal variations in the coefficients determined with the absolute calibration methods. Multi-temporal calibration can be achieved by regular monitoring of targets that are stable over time. Due to the uncertainties related to the seasonal artifacts in the deserts, at least almost one year of PROBA-V data are needed to get accurate   multi-temporal calibration results.

4.5.3.1   Introduction

The multi-temporal calibration of deserts doesn't rely on extern BRDF data sources, but on the PROBA-V desert data itselves. It assumes temporal stability of the surface, andlow variability of overlying atmosphere. All new acquired data are compared to comparable data of the same desert site in this reference database. Comparable means they have **approximately corresponding** geometries. More specifically a PROBA-V desert archive dataset over a period of almost one year. The angles defining the geometry are the sun zenith angle (SZA), the view zenith angle (VZA) and the relative azimuth angle (RAA).

The comparison is performed on BOA reflectance, meaning that all data are atmospherically corrected data with SMAC considering ozone, water vapour, pressure (from ECMWF) and AOT.

A large reference PROBA-V reference database is needed in order to find acquisitions fulfilling this condition and to remove/correct for seasonal effects.

4.5.3.2   Algorithmic implementation

The approach is schematically given in Figure 22 and described in more detail in the next paragraphs.
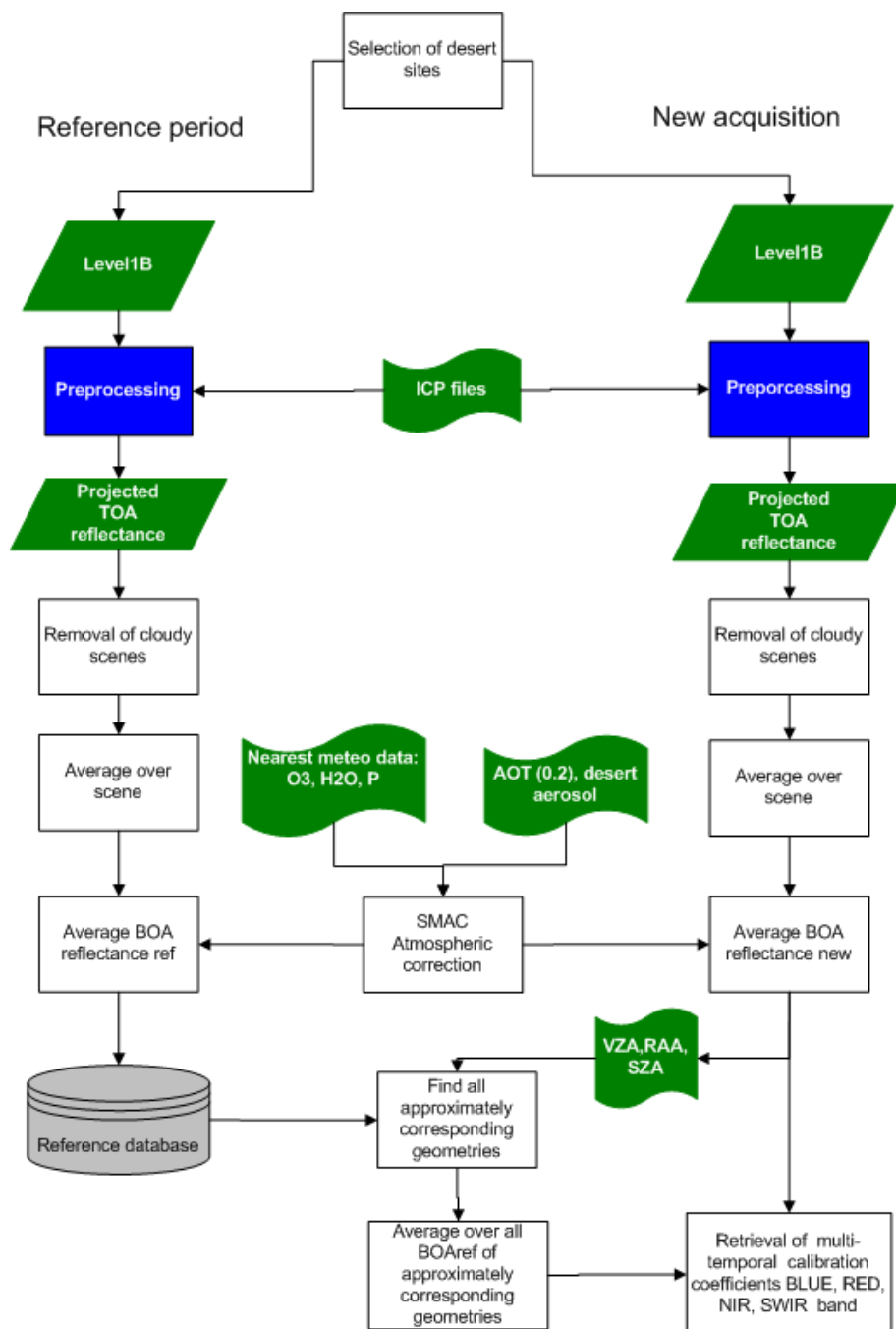
Figure 22: Flowchart multi-temporal calibration over deserts

4.5.3.2.1 Generation of reference database

For a sufficiently large time period a database of PROBA-V BOA reflectance data over the different deserts sites () needs to be compiled. For this, each Level1B image over a desert site has to be processed in the following way:

a. Preprocessing of the L1B data to projected TOA reflectances:

⇨ Conversion to DNs to TOA radiance $L_{TOA}^{meas,ref}$ by applying current calibration coefficients following Equation 4.

⇨ Conversion of TOA radiance $L_{TOA}^{meas,ref}$ to apparent TOA reflectance $\rho_{TOA}^{meas,ref}$ (Equation 8)

⇨ Projection of the the data

b. ROI extraction and remval of cloudy scenes according procedure described under 4.4.4.2.3

c.　Averaging of $\rho_{TOA}^{meas,ref}$ over the scene, which gives $\overline{\rho}_{TOA}^{meas,ref}$

d.　Atmospheric correction using SMAC, considering O3, H2O, Pressure, AOT (= 0.2) and the desert aerosol model which results in the average bottom of atmosphere reflectance $\overline{\rho}_{BOA}^{meas,ref}$

e.　Storage of $\overline{\rho}_{BOA}^{meas,ref}$ together with the sun and viewing geometry for the observation ((SZAref, VZAref, RAAref) in reference database

4.5.3.2.2　Finding comparable acquisitions

First, for each new acquisition, the above described processing steps (a to d) have to be applied to the data to retrieve the average bottom of atmosphere reflectance of the new acquisition $\overline{\rho}_{BOA}^{meas,new}$.

Next, the reference database is searched for comparable acquisitions over the desert site. Such a pair consists of one PROBA-V and one PROBA-V reference observation of the same desert site which are expected to show no differences in result induced by geometry.

Comparable means they have either **approximately identical** or **approximately corresponding** geometries.

The angles defining the geometry are the sun zenith angle (SZA), the view zenith angle (VZA) and the relative azimuth angle (RAA).

Identical geometry means that these 3 angles are the equal for both observations. Then the TOA reflectance can be assumed the same:

$$\rho^{TOA}_{REF}(SZA_{REF}, VZA_{REF}, RAA_{REF}) = \rho^{TOA}_{NEW}(SZA_{NEW}, VZA_{NEW}, RAA_{NEW})$$

Corresponding angles are pairs of angles that yield the same reflectance due to the reciprocity principle. This states that if SZA and VZA are exchanged, the same result is obtained:

$$\rho^{TOA}_{REF}(SZA_{REF}, VZA_{REF}, RAA_{REF}) = \rho^{TOA}_{NEW}(VZA_{NEW}, SZA_{NEW}, RAA_{NEW})$$

If we also assume that the reflectance behaves symmetrical with respect to the principal plane, we also obtain corresponding angles for a change from + RAA tot -RAA:

In practice, pairs of angles will normally never match exactly. However, an exact match is also not necessary: similar angles will still lead to comparable reflectances. Therefore we relax the requirement to **approximately** comparable angles.

A angle pair is considered approximately matching if :

$$(SZA_{REF} - SZA_{NEW})^2 + (VZA_{REF} - VZA_{NEW})^2 + (RAA_{REF} - RAA_{NEW})^2/4 < tol^2$$

where a sensible value for the tolerance is: tol = 10

A angle pair is considered approximately matching if :

$$(SZA_{ref} - SZA_{new})^2 + (VZA_{ref} - VZA_{new})^2 + (RAA_{ref} - RAA_{new})^2/4 < tol^2$$

where a sensible value for the tolerance is: tol = 10.

All reference acquisition fulfilling this conditions are averaged to retrieve the reference value $\overline{\rho}_{BOA}^{ref}$.

4.5.3.2.3   Comparison of new acquisitions to its reference

Finally, an estimate of th the multi-temporal calibration coefficient is calculated as the ratio of $\overline{\rho}_{BOA}^{meas,new}$ to $\overline{\rho}_{BOA}^{ref}$.

4.5.3.2.4   Outlier selection and daily averaging

A daily average is calculated by averaging the results obtained over the different sites after outlier removal. A site is removed if it is detected as an outlier in at least one of the spectral bands. A robust outlier selection procedure based on the median and standard deviation from the median is used for this.

4.5.3.3   Error analysis

The main error sources are :

-   **Aerosol (model and AOT) variation** between new acquisition and reference acquisition
-   **Stability of the site** reflectance between new acquisition and reference acquisition due to stability of the site itself or due to small difference in sun and view geometry
-   Small errors may arise due to **uncertainties in the meteo data** used to perform the atmospheric correction.

A quantification of the uncertainty has been performed by Hagolle and Cabot, 2002 [LIT51] and Hagolle and Cabot, 2003 [LIT52]; The uncertainty (expressed as RMSE) ranged from 3.4 % for blue bands to 1.8 % for NIR bands.These errors are however reduced by averaging over sites and time.

Prototype activities an SPOT-VGT (see PVDOC-647) have indicated that by averaging over sites and time long term multi-temporal calibration uncertainties less than 1% can be achieved for RED, NIR and SWIR bands.

4.5.3.3.1   Interpretation of long term time series

The coefficients obtained per day are in turn used in the statistical trending analysis (see section 4.6.2.3). This analysis uses statistical procedures to derive the best estimate for the current coefficients, based on present and previous data. It includes a short term linear model of the evolution of the coefficients, which is used as an estimation tool.

The long term evolution of the coefficients however merits a separate investigation to aid our understanding of the process and the underlying physics. We plot the results over a sufficiently long time period (> 1 year). An example for SPOT-VGT using monthly averages is shown in Figure 23. Seasonal variations are clear from the plot, but also the longer term downward trend is obvious.
That trend, as expected, appears as an exponential decay. It is possible to describe this by fitting a logarithmic model to the data using classical least squares minimization:

$$A\ (t) = a.ln(t) + b.t + c$$

The obtained curve, (also shown for the example in Figure 23), represents the overall sensitivity decay, with short term variations and seasonal effects filtered out. The decay curve can be computed regularly and so the evolution of the model can also be monitored. The obtained trend will correspond to the results of absolute calibration curve. It also permits to calculate indirectly a calibration coefficient, or even predict it for coming months.

As the decay curve of PROBA-V is expected to be different from these of SPOT-VGT, decay curves derived on the basis of SPOT-VGT can't be used for PROBA-V. Furhermore it can be noticed that the slope of the decay curve of SPOT-VGT2 is much steeper in the months after launch that several monhts later. All this implicates that a long time series of PROBA-V data (> 1 year) is needed before sufficiently accurate decay curves on the basis of deserts can be derived.
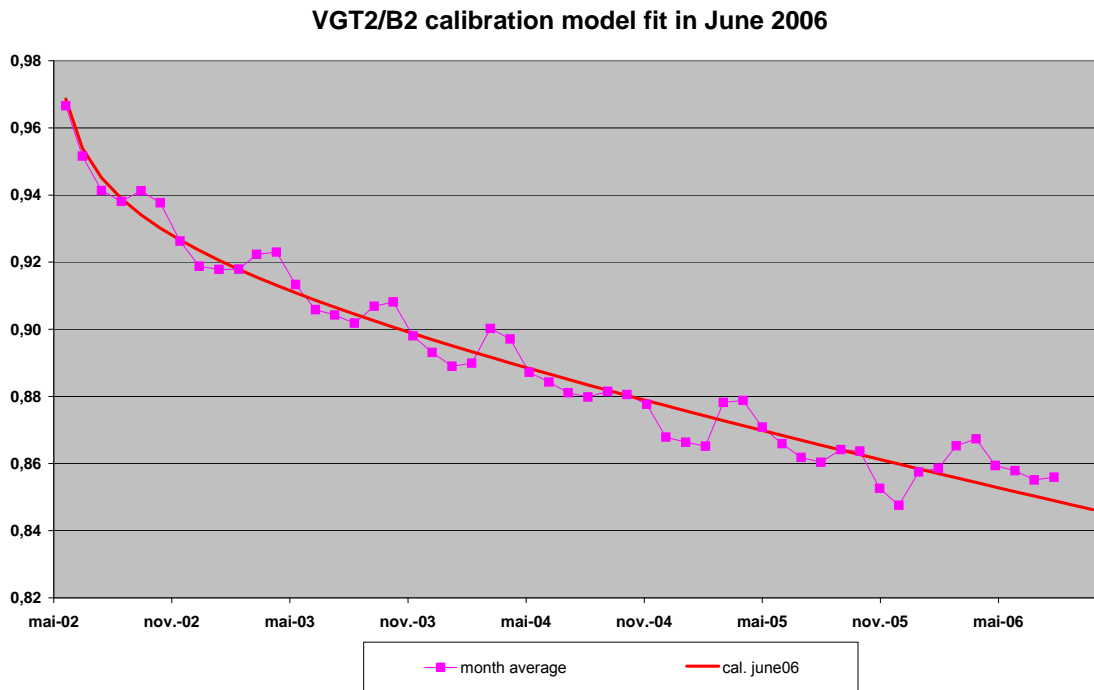
VGT2/B2 calibration model fit in June 2006

Figure 23: example of multi-temporal variation (taken from SPOT-VGT2)

4.5.4 Multi-temporal Antarctica

4.5.4.1 Introduction

Multi-temporal calibration over Antarctica has the same goal than that over desert sites, to monitor the stability of the sensors response over time.

4.5.4.1.1 Advantages

The use of test site on Antarctica has several advantages compared to desert test site, we list them here:
- very uniform targets
- very stable targets (also very bright in VNIR)
- high accessibility: there are 6 or 7 overpasses, so several images can be acquired in 1 day.
- high altitude sites (no aerosol)

4.5.4.1.2 Disadvantages

However, it also as some disadvantages:
- only possible during summer months at Antarctica (December/January)
- special acquisition required
- necessary to change integration time change to prevent saturation
- BRDF effects for snow and ice are substantial, proper BRDF model is needed if observations are made under a different sun-viewing geometry

Because of all the previous, the use of a test site on Antarctica is a valuable addition to the calibration plan, especially to validate the results of the calibration over deserts (multi-temporal and cross sensor calibration)

4.5.4.1.3 Calibration area

We will use the well known "Dome C" area, its location on Antarctica is shown in Figure 24. It is about 716 x 716 km² large. The area is divided into 36 grid boxes of 120 x 120 km². Dome C station is located in grid box 15. The calibration is done on 4 of these grid boxes where spatial studies have indicated that the area within grid box is sufficient homogenous.
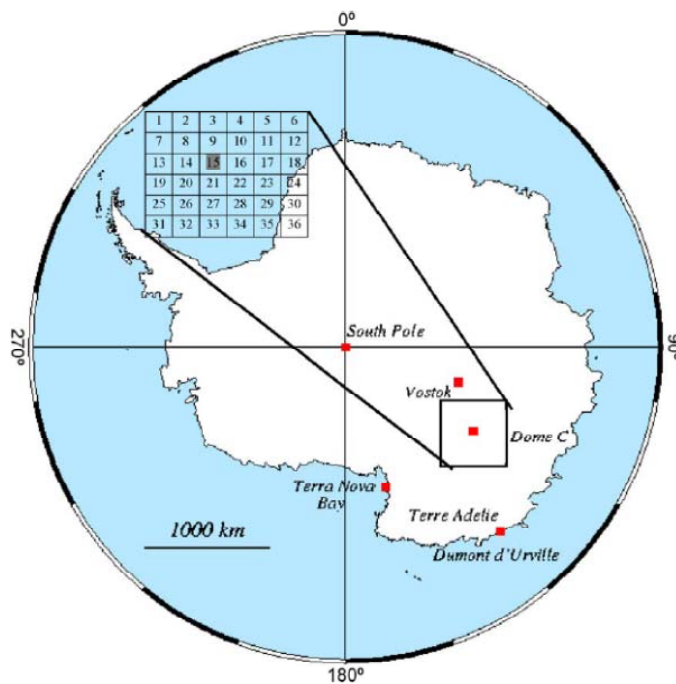
Figure 24: Location of Dome C calibration site (75°s, 123°E)

4.5.4.2   Algorithm

4.5.4.2.1   Data collection

Antarctica is not part of the normal operational imaging of PROBA-V. This means that no daily routine acquisitions are available. Calibration can only be achieved from a dedicated acquisitions. Dedicated acquisitions are needed also for another reason: the targets observed are so bright that they would saturate under normal operational settings. Therefore special settings are necessary: Images should be taken with low integration time settings.

4.5.4.2.2   Data processing

Data processing can be performed in the same way as for the multi-temporal calibration over desert sites (using BRDF and aerosol conditions relevant for Antarctica).

4.5.4.3   Error analysis

Earlier studies by CNES reported accuracy in the range of 2 to 3%.

4.5.5   Multi-temporal Moon

4.5.5.1   Introduction

The surface of the moon is stable over thousands of years. Although brightness of the moon varies with illumination and viewing geometry, the photometric stability of the lunar surface enables to characterise these cyclic variations with high precision. For these reasons the CEOS WGCV has endorsed the Moon as a reference standard for calibration stability (Stone, 2008 [LIT40]).

Through a pitch manoeuvre lunar calibration images will be acquired once per month at a phase angle near 7 degrees. This phase angle is preferred as it maximizes the illuminated surface of the moon while avoiding increased uncertainty by minimizing the opposition effect. For each lunar calibration the radiances observed by PROBA-V are integrated over the lunar image images. Although the surface of the moon remains unchanged over the lifetime of PROBA-V, the observed radiance varies due to :

⇨ Variations in Sun-Moon distance
⇨ Variations in PROBA-V-Moon distance

⇨ The phase angle differences
⇨ The libration angle differences
⇨ Variation in oversampling of the lunar images in the along track direction

The complexity of these dependencies mandates the use of a lunar radiometric model. The USGS lunar calibration program has developed such an operational lunar model based on more than 85000 images acquired by the ground-based Robotic Lunar Observatory (ROLO).

4.5.5.2 Procedure

The lunar calibration procedure involves interfacing with the lunar calibration program at USGS.
The raw lunar images (in DN) are first calibrated to radiometric quantities. Then the integrated irradiance attributed to the Moon is determined by summing all pixels on the lunar disk including the unlit portion. This is done for all spectral bands.

For each spectral band the irradiance, the time of observation (UTC) of geometric center of the moon and the instrument location are provided to the lunar calibration program. The lunar calibration system generates the precise location of the sun and the moon, the distances and photometric geometries and the modelled lunar irradiances. These modelled irradiances are interpolated to the spectral bands of PROBA-V and corrected to the observation distances.

These modelled lunar irradiance values can then directly be compared to the PROBA-V measurements. The monthly measurements/model comparisons are then used in a time series analysis in order to track the radiometric stability.

4.5.5.3 Performance evaluation

 The achievable accuracy of the lunar calibration depends on the lunar irradiance model predictive precision , underpinned by the inherent stability of the Moon and the random errors associated with calculation of the irradiance values from the PROBA-V lunar observations (Stone, 2008 [LIT40]).

The USGS lunar irradiance model fits the ROLO observations with an average residual over all bands just under 1%. This value effectively represents the 'relative' precision of the model's predictive capability (Stone, 2008 [LIT40]). Stability monitoring can be achieved with sub-percent per year precision.

The main advantage of lunar multi-temporal calibration over desert sites is that calibration results can obtained immediately while for the desert calibration data over at least one year are needed to correct for seasonal variations.

Due to uncertainties in the 'absolute' lunar irradiances, the moon can not be used as an absolute radiometric standard.

4.6　Statistical analysis on calibration coefficients

4.6.1　Introduction

Let us assume that we have (different operational methods to estimate the absolute calibration coefficient (A^k) for the different spectral bands (k). The operational methods in use are currently:

⇨　Rayleigh:　　　　　estimate A^k for BLUE, RED, needs A^{NIR} as input
⇨　Deserts:　　　　　estimate A^k for all bands: BLUE, RED, NIR and SWIR
⇨　Sun Glint:　　　　estimate A^k for BLUE, NIR and SWIR, needs A^{RED} as input
⇨　Clouds　　　　　　estimate A^k for BLUE and NIR, needs A^{RED} as input

For each method PROBA-V images are acquired over a number of sites during several acquisition days. For all the suitable pixels in the image an absolute calibration coefficient is calculated. The topic we address here is how to calculate the best estimate of A^k at the current day t_c based on all these different estimates of A^k?

The approach to calculate the best estimate of A^k is graphically illustrated in Figure 25 and explained in detail in the following sections. For statistical analysis we follow roughly the approach of Govaerts et al., 2004 [LIT41] . The trend analysis and the final reconciliation of the different methods are similar to the MISR approach (Bruegge et al., 1999 [LIT42]). In the next paragraph we will omit the index k for the spectral band.
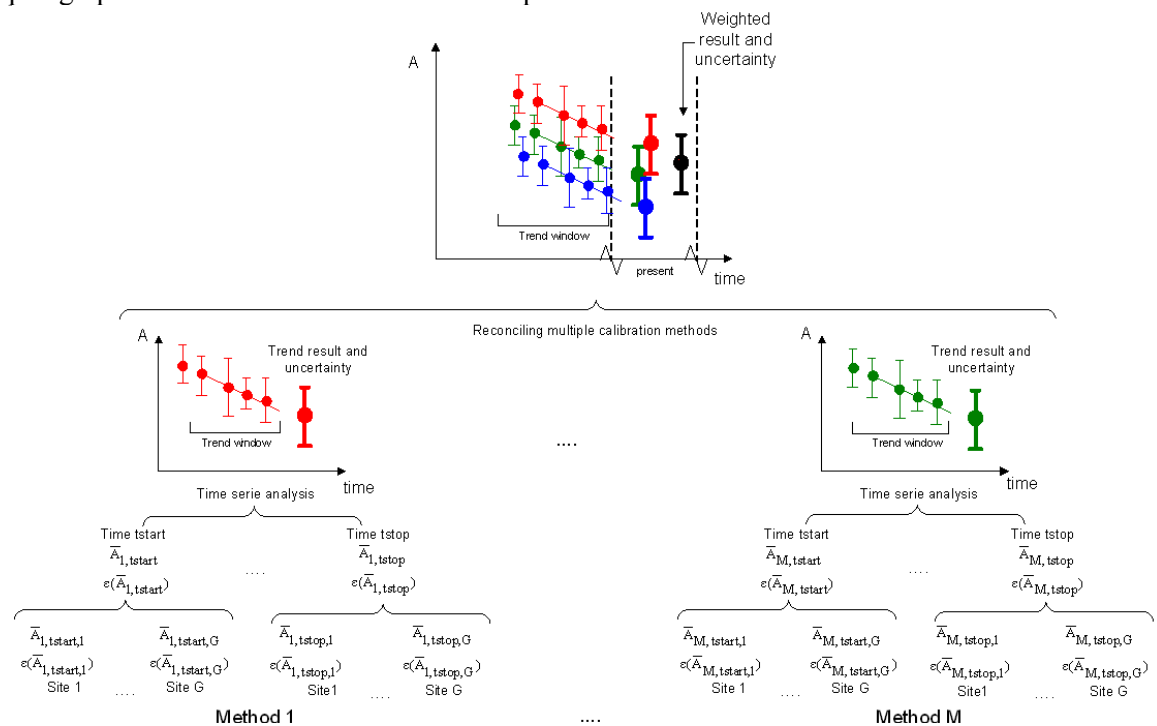

Figure 25: Calculation of best estimate of A^k

The following notations are used in this chapter (Table 19):

t	Time index expressed in days
m	Method index
g	Site index
p	Pixel index
P	Number of pixels
M	Number of methods
G	Number of sites
T	Number of acquisition days

Table 19 : Notations

4.6.2 Approach

4.6.2.1 An individual image (1 method, 1 site, 1 acquisition day)

First, we consider only one site of one method at one acquisition day. Following the calibration method specific pre-processing steps P 'suitable' calibration pixels are selected in the image. For all these suitable pixels an absolute calibration parameter is calculated:

$$A_{m,t,g}(p) \text{ with } p \text{ from 1 to P}$$

4.6.2.1.1 Outlier detection and handling

A statistical analysis is performed on the N_p absolute calibration coefficients to remove outlier values. This outlier selection method uses the median (MED) and the Median Absolute Deviation (MAD) instead of the mean and standard deviation. While the mean and standard deviation can be affected by a few extreme values or by even a single extreme value, the median and MAD are minimally effected by the outliers. $MED_{m,t,g}$ and $MAD_{g,m,t}$ are calculated as

$$MED_{m,t,g} = median\left(A_{m,t,g}(p)\right)_{p=1\ldots P}$$

and

$$MAD_{m,t,g} = median\left(\mid A_{m,t,g}(p) - MED_{m,t,g} \mid\right)_{p=1\ldots P}$$

When the MAD value is scaled by a factor of 1.483, it is similar to the standard deviation in a normal distribution:

$$S_{MAD_{m,t,g} = 1.483 \cdot MAD_{m,t,g}}$$

Pixels with an absolute calibration value outside the 3-sigma confidence interval are removed. The selected pixels have therefore to obey the following condition:

$$MED_{m,t,g} - 2.56 \cdot S_{MAD_{m,t,g}} \leq A_{g,m,t}(p) \leq MED_{m,t,g} + 2.56 \cdot S_{MAD_{m,t,g}}$$

After removing the outliers the site-averaged calibration parameter is calculated for the remaining Pc values as

$$\overline{A}_{m,t,g} = \frac{1}{N_{pc}} \sum_{p=1}^{P_c} A_{m,t,g}(p)$$

4.6.2.1.2 **Error assessment**

This associated relative error $\varepsilon(\overline{A}_{g,m,t})$ is calculated as the square root of the quadratic sum of all error contributions which can be assumed uncorrelated. These error contributions are :

1. Errors due to uncertainties in atmospheric parameters (ε_{atm}) (e.g. the relative uncertainty introduced in the absolute calibration coefficient due to for instance the uncertainty in meteo-data)
2. Errors due to uncertainties in surface characterization (ε_{surf}) (e.g. uncertainty in reference BRDF)
3. Errors due to 'calibration errors' in reference bands (ε_{cal})
4. Errors due to intrinsic uncertainties in RTF model (6SV, Libradtran,modtran) (ε_{rtf})
5. Errors due to noise (due to both nstrument noise and target non-uniformity) (ε_{noise})

Therefore the total relative error for $\overline{A}_{g,m,t}$ can be written as :

$$\varepsilon(\overline{A}_{m,t,g}) = \sqrt{\varepsilon^2_{atm_m} + \varepsilon^2_{surf_m} + \varepsilon^2_{cal_m} + \varepsilon^2_{rtf_m} + \varepsilon^2_{noise_{m,t,g}}}$$

The first three errors ($\varepsilon_{atm}, \varepsilon_{surf}, \varepsilon_{cal}$) are included in the error analysis performed for the different calibration methods. A distinction can be made between random and systematic errors. Random errors ($\varepsilon_{atm}, \varepsilon_{surf}$) can be reduced by spatially averaging over several sites (see next section).

$\varepsilon_{noise_{m,t,g}}$ is estimated from the image at a confidence interval of 95 % and assuming a normal distribution as :

$$\varepsilon_{noise_{m,t,g}} = \frac{1.96 \cdot S_{\overline{A}_{m,t,g}}}{\overline{A}_{m,t,g} \cdot \sqrt{P_c}}$$

with

$$S_{\overline{A}_{m,t,g}} = \sqrt{\frac{1}{P_c - 1} \sum_{p=1}^{P_c} \left[\overline{A}_{m,t,g}(p) - \overline{A}_{m,t,g} \right]^2}$$

This analysis results in an average absolute calibration parameter $\overline{A}_{m,t,g}$ and associated relative error $\varepsilon(\overline{A}_{m,t,g})$ calculated based one site, from one method and one acquisition day.

4.6.2.2 Spatial averaging (all sites for one method, one acquisition day)

Calibration coefficients derived over all calibration sites for one method and one moment in time are spatially averaged to reduce random errors . These random errors can be reduced by the square root of the number of sites assuming that these errors are not correlated in space.
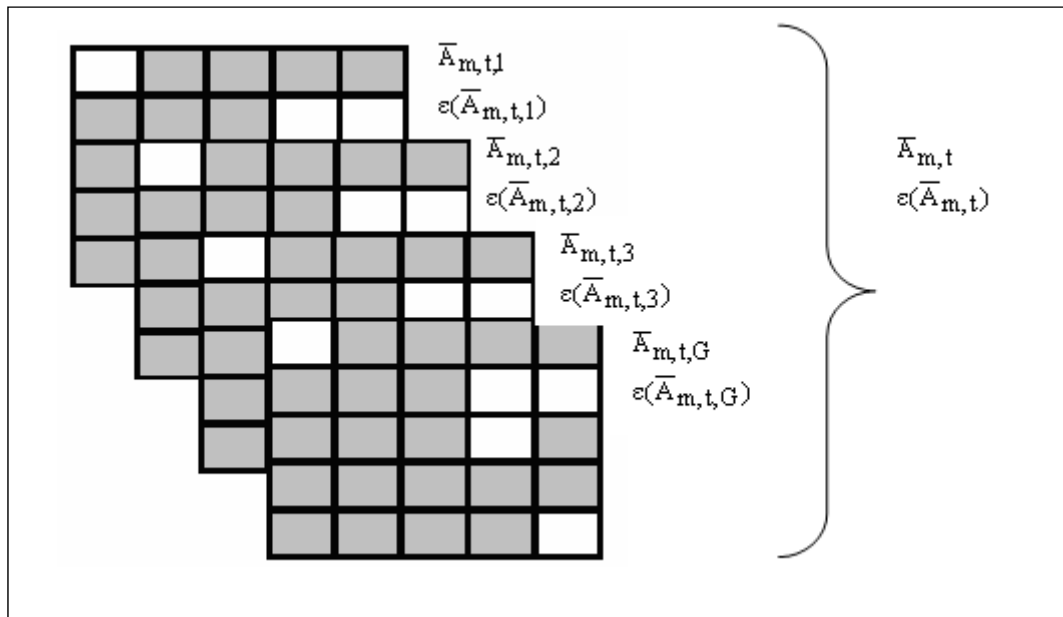
Figure 26: Spatial averaging

A robust outlier detection test using median and S_{MAD} estimates is performed similar to the one in section 4.6.2.1.1. Sites with calibration coefficients that fall outside the confidence interval are assumed outliers and are disregarded.

When a site is often indicated as an outlier, it should be investigated if this systematic bias is due to for instance an erroneous surface characterization (eg. marine reflectance not valid for that site).

Once the outliers are removed the weighted mean $\overline{A}_{w_{m,t}}$ over the Gc remaining sites is calculated:

$$\overline{A}_{w\,m,t} = \sum_{g=1}^{Gc} w_{m,t,g} \cdot \overline{A}_{m,t,g}$$

The weights for each site calculated using normalized weights inversely proportional to the site-average calibration error $\varepsilon(\overline{A}_{m,t,g})$ as :

$$w_{m,t,g} = \left(\frac{1}{\varepsilon(\overline{A}_{m,t,g})}\right)^2 \Bigg/ \sum_{g=1}^{Gc}\left(\frac{1}{\varepsilon(\overline{A}_{m,t,g})}\right)^2$$

The associated relative error $\varepsilon(\overline{A}_{m,t})$ at 2-sigma is calculated as :

$$\varepsilon(\overline{A}_{m,t}) = \sqrt{\frac{\varepsilon_{atm_m}^2}{Gc} + \frac{\varepsilon_{surf_m}^2}{Gc} + \varepsilon_{noise_{m,t}}^2 + \varepsilon_{cal_m}^2 + \varepsilon_{rtf_m}^2}$$

with

$$\varepsilon_{noise_{m,t}} = \frac{t_{\alpha/2,Gc-1} \cdot S_{\overline{A}_{w_{m,t}}}}{\sqrt{Gc-1} \cdot \overline{A}_{w_{m,t}}}$$

and $S_{\overline{A}_{w_{m,t}}}$ the standard deviation of the weighted mean .

4.6.2.3   Trending analysis (all sites for one method, different acquisition days)

The greatest change in sensor response is expected immediately following launch. However after a few months in orbit the responsivity of each camera is expected to change more slowly in time. The characterisation of this responsivity change require a large number of observations

over time due to the uncertainty with which a single observation is made. A trending analysis is performed on the time series of coefficients obtained per method. Each newly generated coefficient $\overline{A}_{w_{m,t}}$ will be combined with previous generated coefficients and the best trend line is calculated. This procedure is explained in this paragraph. The important things to be determined in the trending analysis are: (1) the trending model, (2) time scale, (3) the weighting of the different observations.

4.6.2.3.1 Linear Model

We choose a linear model. Then we can use linear regression, which is performed using the classical least squares optimisation. For every acquisition day t we have calculated absolute calibration coefficient $\overline{A}_{w_{m,t}}$. The set of T (t, $\overline{A}_{w_{m,t}}$) pairs for the time interval [t+1-T,t] is used to fit a linear model

$$Model_{[t+1-T\ldots t]}(\overline{A}_{w_{m,t}}) = a_0 + b \cdot t$$

The offset a_0 and the slope b of the model are computed from the data so that the sum of the squared difference between $\overline{A}_{w_{m,t}}$ and their model values $Model_{[t+1-T\ldots t]}(\overline{A}_{w_{m,t}})$ is minimized or using the notation:

$$< X > = \frac{1}{T} \sum_{\tau=t+1-T}^{t} X_\tau$$

We can express the solution of the linear regression as:

$$b = \frac{< \overline{A}_{w_{m,t}} \cdot t > - < \overline{A}_{w_{m,t}} > . < t >}{< t^2 > - < t >^2}$$

$$a_0 = < \overline{A}_{w_{m,t}} t > - b < t >$$

The result of the linear regression is shown as the middle red line in Figure 27.
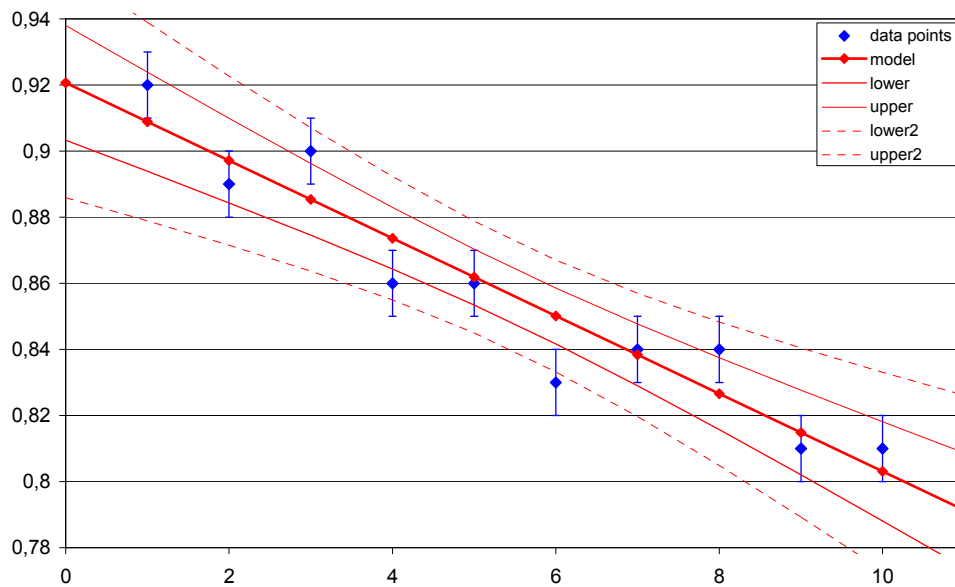

Figure 27: Result of linear regression, with 1 and 2 sigma confidence intervals

4.6.2.3.2 Linear Weighted Model

The previous model assumed equal importance of all data points. However we want to assign weights to individual data points. This has two reasons:

⇨ every data point was determined with a different accuracy $\varepsilon(\overline{A}_{m,t})$; for simplicity denoted as ε_t. These are accounted for by weighting with a factor : $1/\varepsilon_t^2$

⇨ the data points closer to the current time are assumed to be more important than the earlier points. We propose a time window with weights that linearly increase from 0 at the starting time t_{start} to 1 at the end time t_{stop}. :

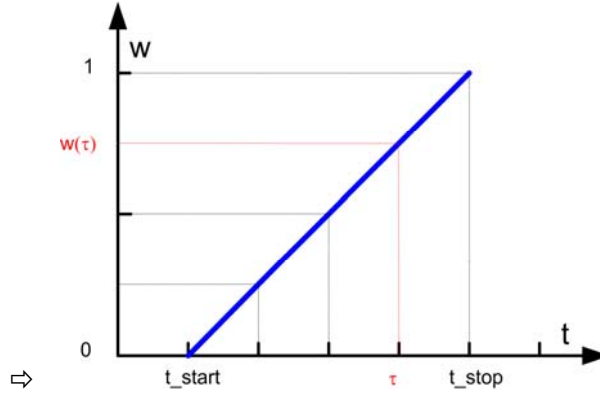$$w''_{\tau} = \frac{\tau - t_{start}}{t_{stop} - t_{start}}$$

Figure 28: time window with linearly increasing weights

⇨ For the time window of size T, with $t_{stop} = t$ and $t_{start} = t+1-T$, we obtain:

$$w''_{\tau} = \frac{\tau - t + (T-1)}{T-1}$$

Both weights can be combined into a single weighting factor:

$$w'_{\tau} = \frac{\tau - t + (T-1)}{(T-1)\varepsilon_{\tau}^2}$$

If we divide by the average weight <w'>, we obtain weights which sum equal to T:

$$w_{\tau} = \frac{w'_{\tau}}{<w'>}$$

The weights are taken into account in the linear regression model by using weighted averages:

$$<wX> = \frac{1}{T}\sum_{\tau=t+1-T}^{t} w_{\tau} X_{\tau}$$

Using these we derive:

$$b_w = \frac{<w\overline{A}_{w_{m,t}} t> - <w\overline{A}_{w_{m,t}}> \cdot <wt>}{<wt^2> - <wt>^2}$$

$$a_{w0} = \frac{<w\overline{A}_{w_{m,t}}> \cdot <wt^2> - <wt> \cdot <w\overline{A}_{w_{m,t}} t>}{<wt^2> - <wt>^2}$$

The results of weighted linear regression are shown as the middle red lines in Figure 29 and Figure 30. In Figure 29, only temporal weights are used. Compared to the previous result, this follows more closely the last (more recent) points in time.
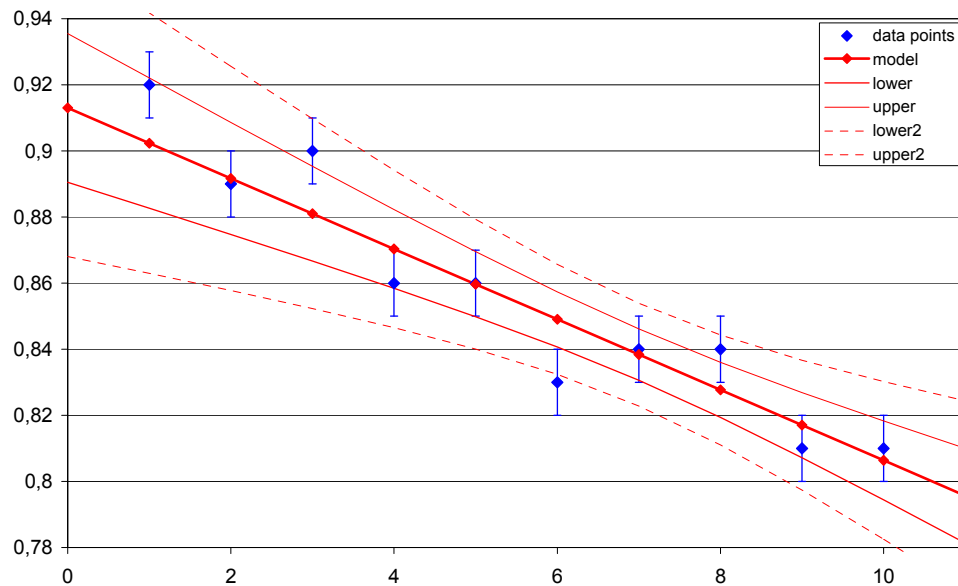
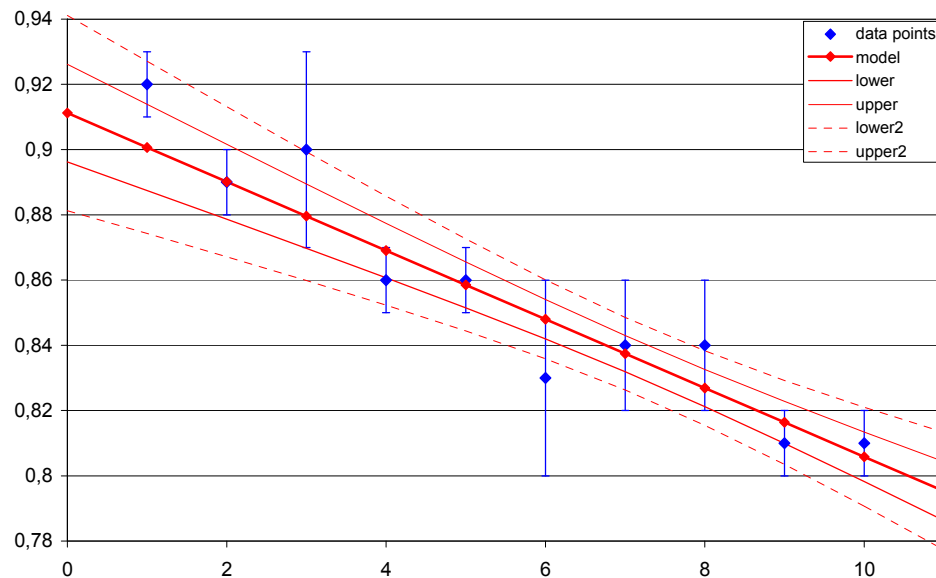**Figure 29: Result of linear regression, including temporal weighting.**

Figure 30: Result of linear regression, including temporal weighting and individual accuracies

4.6.2.3.3   Accuracy of the unweighted model

The standard deviation about the regression (S_r) is given by

$$S_r = \sqrt{\frac{S_{AA} - \left(b^2 \cdot S_{TT}\right)}{(T-2)}}$$

with

$$S_{AA} = T\left(< \overline{A}_{w_{m,t}}^{\;2} > - < \overline{A}_{w_{m,t}} >^2\right), \; S_{TT} = T\left(< t^2 > - < t >^2\right)$$

The standard deviation for the predicted or modelled $Model_{[t+1-T...t]}(\overline{A}_{w_{m,t}})$ value at time τ is given by

$$S_A(\tau) = S_{wr}\sqrt{1 + \frac{1}{T} + \frac{(\tau - <t>)^2}{S_{TT}}}$$

The 95 % confidence interval on the modelled value $Model_{[t+1-T...t]}(\overline{A}_{w_{m,t}})$ is then given by +/-

$1.96\, S_A(t)$

Logically, the model will yield the smallest errors for values of τ close to the average value $<t>$ used to generate the model. Further away, the error will be larger. The confidence intervals are also plotted for the example in Figure 27. The intervals are small in the middle of the observations, and larger near the sides.

4.6.2.3.4   Accuracy of the weighted model

For the weighted regression the formulae become:

$$S_{wr} = \sqrt{\frac{S_{wAA} - \left(b_w^{\;2} \cdot S_{wTT}\right)}{(T-2)}}$$

with

$$S_{wAA} = T\left(< w\overline{A}_{w_{m,t}}^{\;2} > - < w\overline{A}_{w_{m,t}} >^2\right), \quad S_{wTT} = T\left(< wt^2 > - < wt >^2\right)$$

The standard deviation for the predicted or modelled $Model_{[t+1-T...t]}(\overline{A}_{w_{m,t}})$ value for the weighted model at time τ is given by

$$S_{wA}(\tau) = S_{wr}\sqrt{1 + \frac{1}{T} + \frac{(\tau - <wt>)^2}{S_{wTT}}}$$

The 95 % confidence interval on the modelled value $Model_{[t+1-T...t]}(\overline{A}_{w_{m,t}})$ is then given by +/-

$1.96\, S_{wA}(\tau)$

The last equation was use to determine the confidence intervals in Figure 29 and Figure 30. The intervals are smaller near the end. In Figure 30, individual accuracies are given: some points get a larger error and are used less in the regression. As a result; the confidence intervals become narrower.

4.6.2.3.5   Result of the trending analysis

Every day t, a new coefficient $Model_{\tau=t+1-T...t}(\overline{A}_{w_{m,t}})$ is obtained. The model from the previous day gives the best estimate for the coefficient of the present day, without using actual value of that day $\overline{A}_{w_{m,t}}$:

$$Model_{\tau=t-T...t-1}(\overline{A}_{w_{m,t}}) = a_{0,\tau=t-T...t-1} + b_{\tau=t-T...t-1} \cdot t$$

We can also determine a (99%) confidence interval around the estimated value by adding $\pm (2{,}56)S_A(t)$

We mark $Model_{\tau=t+1-T...t}(\overline{A}_{w_{m,t}})$ as a ***potential outlier*** if it falls outside the confidence interval. It is not used in further models, unless it is unmarked at a later moment in time.

Every day, the new estimate $Model_{\tau=t+1-T...t}(\overline{A}_{w_{m,t}})$ is computed from the model by adjusting the time window. The new estimates together constitute the time evolution. Values marked as potentials outliers are not used in the model. After the model is set, all potential outliers are rechecked against the criterion. If they now fall into the interval they are unmarked and then no longer treated as outliers.

The uncertainty in $Model_{\tau=t+1-T...t}(\overline{A}_{w_{m,t}})$ (at 2-sigma) is calculated as follows :

$$\varepsilon\left(Model_{\tau=t+1-T\ldots t}(\overline{A}_{w_{m,t}})\right)=\sqrt{\frac{\varepsilon^2_{m,random}}{T}+\varepsilon^2_{m,systematic}+\varepsilon^2_{m,fit}}$$

with $\varepsilon_{m,fit}=\dfrac{1.96\cdot S_A(t)}{Model_{\tau=t+1-T\ldots t}(\overline{A}_{w_{m,t}})}$

Note that the random and systematic errors are treated separately, as explained in the previous section. It is important that a critical assessment is made to estimate systematic errors (bias) for every method. E.g. if a method (e.g. desert calibration) shows substantially different values than other methods in other calibration systems, it is likely that this method contains some unknown source of systematic error.

4.6.2.4   Combining different methods

The previous analyses are performed for each calibration method separately. Now the calibration coefficient from the trending analysis of the M different methods will be combined in a single calibration parameter. Not all methods yield coefficients for all different bands.

4.6.2.5   Combined coefficients: combining function F_{comb}

The $Model_{\tau=t+1-T\ldots t}(\overline{A}_{w_{m,t}})$ coefficients from the M different methods are combined in a single $\overline{A}_{w_t}$ for day t. The is done by computing the weighted average as :

$$\overline{A}_{w_t}=\sum_{m=1}^{M}w_{m,t}\cdot Model_{\tau=t+1-T\ldots t}(\overline{A}_{w_{m,t}})$$

with $\quad w_{m,t}=\left.\left(\dfrac{1}{\varepsilon\left(Model_{\tau=t+1-T\ldots t}(\overline{A}_{w_{m,t}})\right)}\right)^2\right/\sum_{m=1}^{M}\left(\dfrac{1}{\varepsilon\left(Model_{\tau=t+1-T\ldots t}(\overline{A}_{w_{m,t}})\right)}\right)^2$

This combining function will be denoted in the next section as F_{comb}. The use of a weighted average ensures that the more accurate results contribute more to the final result.

4.6.2.5.1   Combined accuracy

The relative uncertainty of the combined coefficient $\overline{A}_{w_t}$ should reflect the individual uncertainties $\varepsilon\left(Model_{\tau=t+1-T\ldots t}(\overline{A}_{w_{m,t}})\right)$, which include systematic errors. However, even if systematic errors for individual methods have been assessed, this does not guarantee that all bias between methods has been covered.

From the collection of individual coefficients $\overline{A}_{w_{m,t}}$, we can make an estimate of the in-between method bias. Since only a few coefficients are available, estimating the bias in the classical statistical way does not lead to useful results. Instead we use the method as proposed in Levenson et al 2000 [LIT43]. This assumes a reasonable value for the bias, and describes the bias with a rectangular distribution with extreme values $\pm$ b, which has a standard uncertainty of $\varepsilon=b_m/\sqrt{3}$.

A sensible assumption is that the in-between method bias equals the largest difference between the values for individual methods. We then obtain the following for the uncertainty caused by the in between method bias:

$$\varepsilon^2_{inbetween(m:1...M)}(\overline{A}_{w_{m,t}}) = \frac{1}{\sqrt{3}}\left(MAX_{m:1...M}(\overline{A}_{w_{m,t}}) - MIN_{m:1...M}(\overline{A}_{w_{m,t}})\right)$$

The combined accuracy can be written as the weighted average of the individual uncertainties plus the in between method bias:

$$\varepsilon_t = \sqrt{\sum_{m=1}^{M}\left(w_{m,t}\,\varepsilon\left(Model_{\tau=t+1-T...t}(\overline{A}_{w_{m,t}})\right)^2\right) + \varepsilon^2_{inbetween(m:1...M)}(\overline{A}_{w_{m,t}})}$$

Taking into account the definition of $w_{m,t}$, we can rewrite this to:

$$\varepsilon_t = \sqrt{\frac{M}{\sum_{m=1}^{M}\left(\dfrac{1}{\varepsilon\left(Model_{\tau=t+1-T...t}(\overline{A}_{w_{m,t}})\right)}\right)^2} + \varepsilon^2_{inbetween(m:1...M)}(\overline{A}_{w_{m,t}})}$$

4.6.2.5.2   Interband dependencies

An additional difficulty arises: some methods (Rayleigh, Sun glint) need the value of the coefficient of one band to estimate the other bands. This causes following dependencies:

input A^{NIR}:   Rayleigh method yields estimates: $A^{BLUE}_{Rayl}(A^{NIR})$, $A^{RED}_{Rayl}(A^{NIR})$

no input: Deserts method yields estimates: A^{BLUE}_{Des}, A^{RED}_{Des}, A^{NIR}_{Des}, A^{SWIR}_{Des}

input A^{RED}:   Sunglint method yields estimates: $A^{BLUE}_{Gl}(A^{RED})$, $A^{NIR}_{Gl}(A^{RED})$, $A^{SWIR}_{Gl}(A^{RED})$

input A^{RED}:   Cloud method yields estimates: $A^{BLUE}_{Cl}(A^{RED})$, $A^{NIR}_{Cl}(A^{RED})$

Only the desert method works without input from other estimates. Since simultaneous estimation using different methods is not practically feasible, we propose following flow:
Assume that coefficients have been reliably estimated at time **t-1**, by the combining function F_{comb} that uses the estimates obtained from the different methods (omitting the notation $Model_{\tau=t+1-T...t}$):

$$A^{BLUE}(t-1) = F_{comb}\left(A^{BLUE}_{Rayl}(t-1), A^{BLUE}_{Des}(t-1), A^{BLUE}_{Gl}(t-1), A^{BLUE}_{Cl}(t-1)\right)$$

$$A^{RED}(t-1) = F_{comb}\left(A^{RED}_{Rayl}(t-1), A^{RED}_{Des}(t-1)\right)$$

$$A^{NIR}(t-1) = F_{comb}\left(A^{NIR}_{Des}(t-1), A^{NIR}_{Gl}(t-1), A^{NIR}_{Cl}(t-1)\right)$$

$$A^{SWIR}(t-1) = F_{comb}\left(A^{SWIR}_{Des}(t-1), A^{SWIR}_{Gl}(t-1)\right)$$

Due to the dependencies, the estimates at time **t** can be obtained only if we use initial estimates $A^{RED,init}(t)$, $A^{NIR,init}(t)$. Several option can be considered:

1. The simplest solution is to take:

$$A^{RED,init}(t) = A^{RED}(t-1)$$

$$A^{NIR,init}(t) = A^{NIR}(t-1)$$

This ignores the fact that the desert method already yields results at time **t**.

2. We can incorporate these results by writing:

$$A^{RED,init}(t) = F_{comb}\left(A^{RED}_{Rayl}(t-1), A^{RED}_{Des}(t)\right)$$

$$A^{NIR,init}(t) = F_{comb}\left(A_{Cl}^{NIR}(t-1), A_{Gl}^{NIR}(t-1), A_{Des}^{NIR}(t)\right)$$

3. A more advanced approach would be to predict the change in the other methods, e.g.:

$$\Delta A_{Rayl}^{RED}(t) = \left(A_{Rayl}^{RED}(t) - A_{Rayl}^{RED}(t-1)\right)$$

by assuming that it is proportional to the change in the desert method

$$\Delta A_{Des}^{RED}(t) = \left(A_{Des}^{RED}(t) - A_{Des}^{RED}(t-1)\right)$$

Then we predict:

$$A_{Rayl}^{RED,init}(t) = A_{Rayl}^{RED}(t-1) + \Delta A_{Rayl}^{RED}(t) = A_{Rayl}^{RED}(t-1) + \Delta A_{Des}^{RED}(t) \cdot \frac{A_{Rayl}^{RED}(t-1)}{A_{Des}^{RED}(t-1)}$$

Which then leads to:

$$A^{RED,init}(t) = F_{comb}\left(A_{Rayl}^{RED,init}(t), A_{Des}^{RED}(t)\right)$$

The other coefficients can be handled in the same way.

The initial estimates can be used as input into the applicable methods in order to obtain first iteration estimates ($A^{RED,1}(t)$) for time **t**. In general the estimates are not exactly equal to the initial estimates: $A^{RED,1}(t) \neq A^{RED,init}(t)$, …

Therefore we can iterate the calculations:

$$A^{RED,init}(t) = F_{comb}\left(A_{Rayl}^{RED,init}(t), A_{Des}^{RED}(t)\right)$$

This iteration can be repeated until the values converge. In practice, this should happen after only a few iterations. If this is not the case, it points to a severe problem. Then, the coefficient of the previous day is used, while the cause of the problem should be investigated by an expert.

4.6.3　Updating the operational coefficient

The true calibration coefficients are expected to vary only slowly over time. A new estimate of them is obtained daily. The estimates show small variations from day to day. Only the variations caused by true physical changes should result in updates of the coefficients. Variation caused by the limited accuracy of the estimates should be ignored. This raises the question when operational coefficients need to be updated.

4.6.3.1.1　Update Strategy

We propose to use an update strategy scheme in which an update is possible daily, but is only performed if a significance criterion is satisfied (see below) Such a scheme is is preferably applied over fixed update schemes because:

o compared to a daily update scheme, many unnecessary updates and possible spurious fluctuations are thus omitted.

o compared to update schemes with longer intervals the reaction time to real changes is shorter. This also avoids that the choice of the intervals influences the results (a change occurring in the middle of a month should be treated the same as the same change occurring at the end of a month).

4.6.3.1.2　Significance Criterion

It is best practice to update the coefficients only when it *makes sense*. This notion is translated into a significance criterion. A(t), the new best estimate of the coefficient at time t, is compared to the coefficient at the previous update A(t$_{update}$). The difference between the two is regarded as significant if we are *reasonably confident* that the update reflects a real change and is not a variation due to the estimation.

This is evaluated using a statistical test. Assuming large sample size, we can use the classical z-test for two independent samples. Using the relative errors ε(t) and ε(t$_{update}$) as accuracies, we obtain:

$$z = \frac{\left(A(t) - A(t_{update})\right)}{1,96.\sqrt{\varepsilon^2(t).A^2(t) + \varepsilon^2(t_{update}).A^2(t_{update})}}$$

The z-score must be evaluated by comparing it against its critical value at the suitable confidence level.. For high confidence levels (e.g. 95% or 99%), it answers the question "*are we almost certain that the values are different*".

In our case, if it is unclear whether the values are different or not, we do not want to assume that they are the same, and therefore we still want to update. Thus in fact we have to evaluate the opposite: "*are we confident that the values are the same*". This is obtained by using a z-score critical value for a lower confidence level (e.g. at 5 %, 20 % or even 50 %).
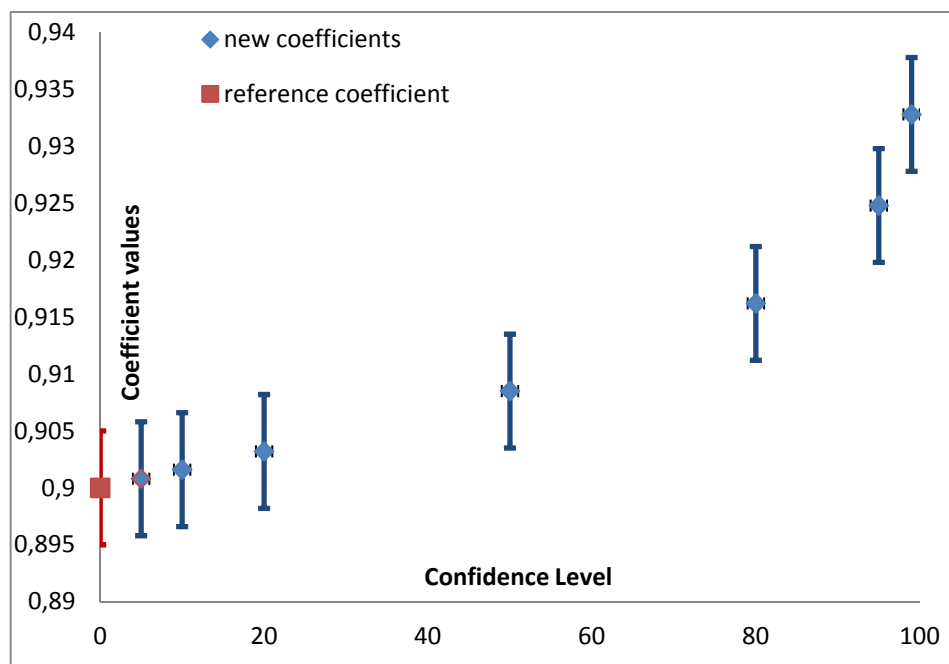

Figure 31: Values for which the difference is just significant at the given confidence level

This concept is illustrated in Figure 31: For a previous coefficient of 0,9, various new values are plotted that correspond to the critical value at various confidence levels. For a chosen confidence level, the value at the plot will be the smallest difference which will be seen as significant.

The choice of the confidence level is critical in this process. Its optimal value will be determined based on calibration experiments, and will be monitored and optimized during commissioning.

4.6.3.1.3   Post monitoring of operational coefficients

The coefficients at time t are also estimated at time t. However when more time has passed, a more accurate estimation can be performed. This is clear from the linear regression graphs in Section 4.6.2.3. Logically,the uncertainty about the linear model is smallest near the middle of the points used. Some cases where future data clearly helps the estimation are:

- if calibration is (partially) missing at time t, but available at time t - 1 and t + 1, interpolating between them is more accurate than using only the results at time t-1.

- If unusual variation is observed at time t, the processing will detect this as an outlier and ignore it. Future data will confirm the data as an outlier or as a new trend, in the latter case including the result is more accurate.

To test if the temporal model is performing well, it is good practice to recalculate the coefficients for time t at a later time so that t lies in the middle of the temporal interval. Both estimations can be plotted together for an additional monitoring of the time evolution estimates.

4.6.4 Dealing with season-dependent errors

Both CNES and Govaerts and Clerici 2004 [LIT1] reported a seasonal trend in desert calibration data. If these seasonal trends are not corrected for it can give erroneous results. These seasonal trends will become only visible when we have more than one year of PROBA-V data. Seasonal trends can be analysed with autocorrelation correlograms.

These seasonal effects will be analyzed with the SPOT VGT data over deserts from different years. If these seasonal trends are consistent over the years, the seasonal trend curve will be used to correct the desert calibration coefficients during the first year in orbit in order to minimize sensor-independent seasonal variation. After one year in orbit these seasonal trend curves can be replaced by PROBA-V derived curves.

4.7   Camera to camera calibration

4.7.1   Introduction

In previous chapters the three different cameras are treated separately. This may result in biases between cameras. To minimize inter-camera deviations a camera to camera calibration method is used based on the overlap area between two adjacent cameras. This method allows also to transfer calibration coefficients from the centrr camera to the outer cameras. This may be needed to calibrate the SWIR band of the western looking camera for which the sun glint spot can't be observed.

PROBA-V has 3 cameras in order to fit the swath requirement. The field of view (FOV) of every camera is 34.6 degrees. Since the outer cameras are pointed off-nadir for about 34.0 degrees, there is a zone of overlap (Figure 32). The camera to camera radiometric calibration method exploits the information delivered in the camera overlap zone. Since pixels in this zone are seen by different cameras but with the same solar azimuth, solar zenith, view azimuth, view zenith and approximately at the same recording time, BRDF effects (atmospheric BRDF, topographic BRDF and target BRDF) have no influence in this calibration.

The camera to camera radiometric calibration methods will be used for:

(a) Continuous checks in the IQC using the "overlap-intermediate-products" delivered by the PF to the IQC. Here, we continuously perform a regression between the TOA radiances of one camera against the TOA radiances of the adjacent camera and perform (1) hypotheses tests to detect if one or another camera starts to drift with respect to radiometry and (2) produce time-dependent plots of the bias. This potentially enables the detection of time dependent effects due to the orbital motion and/or seasonal effects. As such, these checks can deliver a trigger to the IQC to actualize the radiometric calibration parameters supported by the other radiometric calibration results.

(b) Discrete checks in the IQC: if one or another radiometric calibration method delivers a good calibration result for a certain spectral band for a certain camera, this result can be transposed to the other cameras using the information delivered by the camera-to-camera tie-points.

Camera to camera calibration uses the measurements of a limited part of the camera (the overlap pixels) to draw conclusions about the calibration coefficients for the whole camera. Therefore it critically depends on the validity of the equalisation coefficients of the individual pixels.
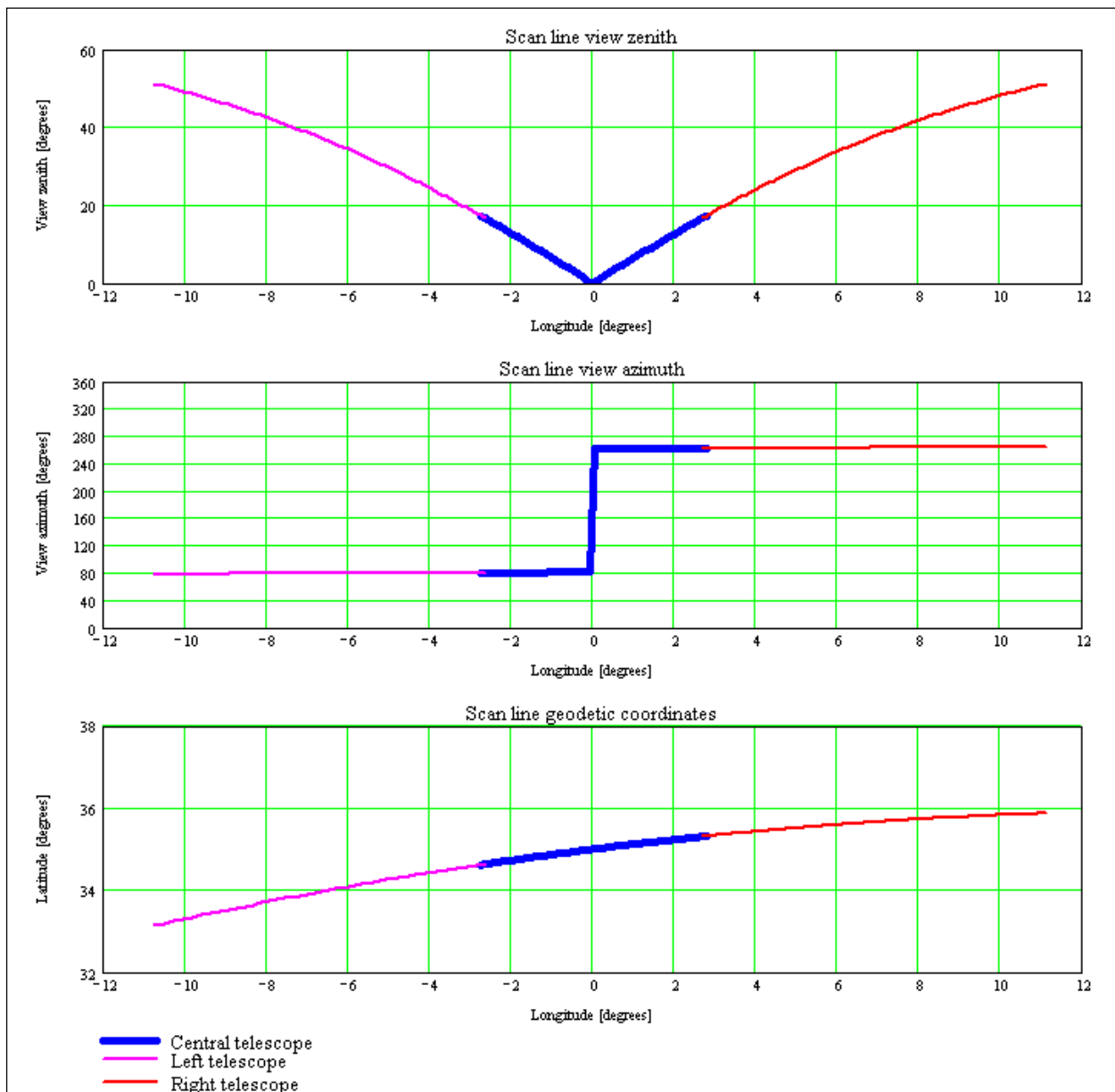
Figure 32: Overview of the viewing geometry for one scan line.

In Figure 32, the settings are: platform position X, Y, Z, roll, pitch, yaw: 0.0°, 35.0°, 820km, 0°, 0°, -8.69°. FOV of one camera equals 34.6°. Outer cameras are pointed off-nadir for 34.0°.

4.7.2 Algorithm

4.7.2.1 Continuous checks

The DNs in overlap-intermediate-products (raw geometry) are first converted to TOA radiances following Equation 4.

Next, the data are projected (see Figure 33) using a distance weighted interpolation technique because this technique produces the least errors (Galbraith et al [LIT44]).
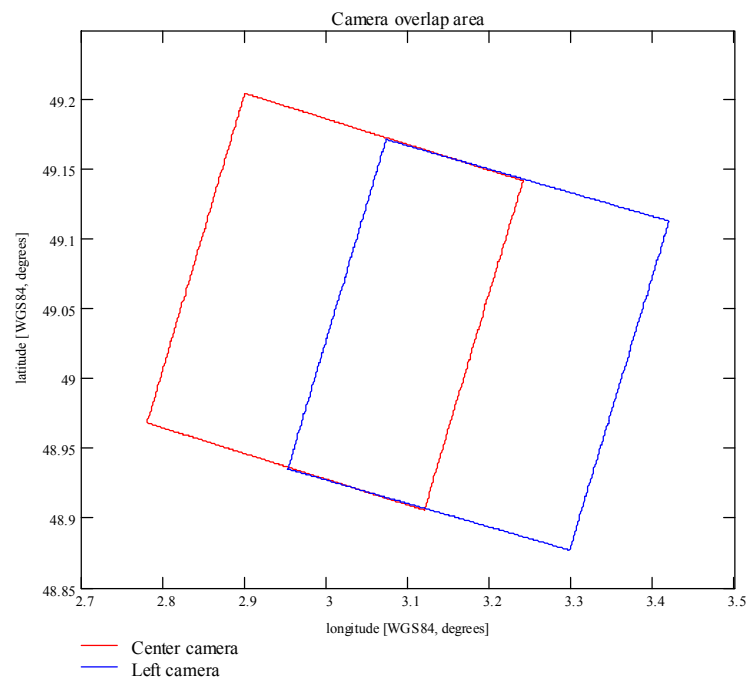
Figure 33 Camera overlap zone

An ASCII file containing TOA radiances for the overlapping pixels is produced using a mosaic-generation application and for each band separately a linear regression between the TOA radiances of one camera against the TOA radiances of the adjacent camera is then performed (Figure 34).

If measurements are comparable all points will be scattered about the 1:1 line. The slope of the regression is close to 1.0 and an intercept close to 0.0.

An alternative way of presenting the results is plotting the differences in TOA radiances between pairs of overlapping points against their mean (Figure 35). This is called the Bland-Altman plot. If the measurements are comparable, the difference should be small centred around 0 without systematic variation with the mean value of pair of pixels.
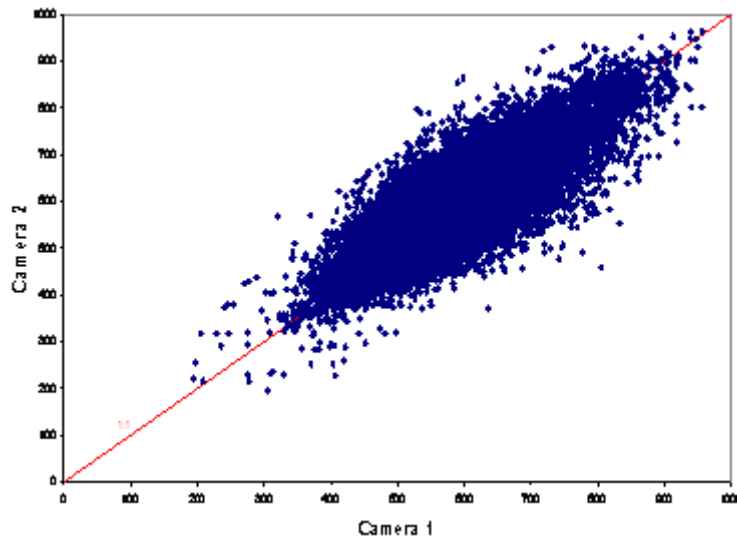
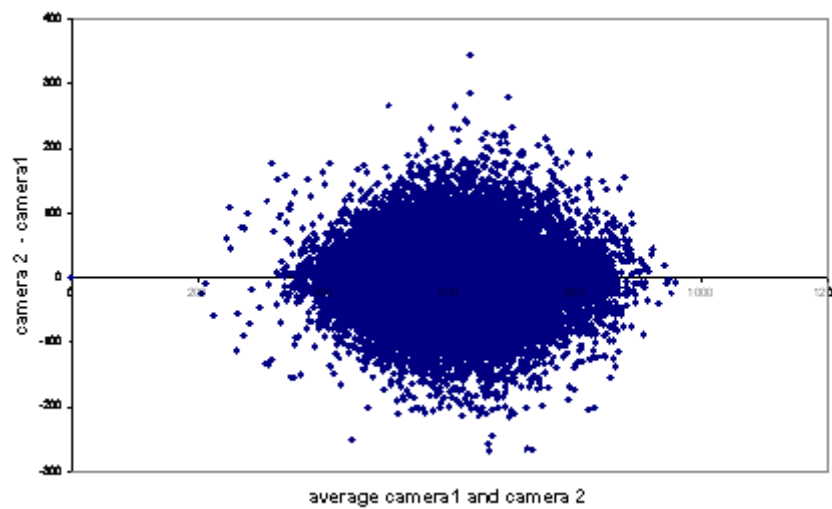**Figure 34: Regression of TOA radiances camera 1 versus camera 2**

Figure 35: Regression of the differences in TOA radiances against their mean

These graphs are supplemented with formal statistical analysis (t-test for paired samples). Under the circumstances that there is no obvious relation between the difference and the mean, agreement between the TOA radiance values of both cameras can be tested with the following statistics.

First, the mean relative difference $\bar{d}$ and the standard deviation S is calculated as

$$\bar{d} = \frac{\sum_{1..N}\left(\left(L^k_{TOA,cam2} - L^k_{TOA,cam1}\right)/L^k_{TOA,cam1}\right)}{N}$$

$$\text{and } S = \sqrt{\frac{1}{N-1}\sum_{1..N}\left[\left(\left(L^k_{TOA,cam2} - L^k_{TOA,cam1}\right)/L^k_{TOA,cam1}\right) - \bar{d}\right]^2}$$

with N the number of overlapping pair of pixels.

The 95 % confidence interval of agreement for individual differences between two cameras is given by :

$$d \pm 1.96S$$

Finally, the 95% confidence interval for the bias is calculated as :

$$\bar{d} \pm 1.96\sqrt{\frac{S^2}{N}}$$

If this confidence interval doesn't contain the value '0.0', there consists a significant bias between the two cameras.

Finally, time series plots $(\bar{d} \pm 1.96\sqrt{\frac{S^2}{N}}$, t) are plotted in order to monitor the bias between cameras over time.

4.7.2.2   Discrete checks

The purpose is to transfer absolute calibration coefficients from one camera to an other camera. This may be needed when a significant bias between cameras is detected with continuous checks on overlap zones and no (good) calibration imagery exist for one of the cameras.

One camera, which we assume to be well calibrated, is used as the reference camera. The absolute calibration coefficients for this reference camera are denoted as A_{ref}^k. The calibration coefficients for the camera which has to be calibrated are denoted as $A_{cal}^{k,old}$ and $A_{cal}^{k,new}$. With $A_{cal}^{k,old}$ the current calibration coefficient and $A_{cal}^{k,new}$ the calibration coefficient to be retrieved based on the overlap zone with the reference camera.

The DNs in overlap-intermediate-products (raw geometry) for both cameras are converted to TOA radiances following Equation 4 using the current calibration coefficients.

$$L_{ref}^k = \frac{DN_{i,acquired}^k - NL_g^k(DN_{i,acquired}^k) - off_{i,g}^k - dc_{i,g,T}^k(IT + dIT^k)}{A_{T,ref}^k \cdot g_{i,g}^k(IT + dIT^k)}$$

$$L_{cal}^{k,old} = \frac{DN_{i,acquired}^k - NL_g^k(DN_{i,acquired}^k) - off_{i,g}^k - dc_{i,g,T}^k(IT + dIT^k)}{A_{T,cal}^{k,old} \cdot g_{i,g}^k(IT + dIT^k)}$$

The set of N (L_{ref}^k, $L_{cal}^{k,old}$) pairs is used to fit a linear model through the origin (assuming correct dark current calibration for both cameras):

$$Model(L_{cal}^k) = b \cdot L_{ref}^k$$

The least square estimators of b in the regression is obtained by minimizing

$$Q = \sum_{i=1}^{N}\left(L_{cal,i}^k - bL_{ref,i}^k\right)^2$$

This leads to the following estimator for b :

$$b = \frac{\sum\limits_{i=1}^{N} L_{cal,i}^{k} L_{ref,i}^{k}}{\sum\limits_{i=1}^{N} (L_{ref,i}^{k})^2}$$

The unbiased estimator of the error variance for the regression is

$$MSE = \frac{\sum\limits_{i=1}^{N} (L_{cal,i}^{k} - model(L_{cal,i}^{k}))}{N-1}$$

The 95% confidence interval for b is given by

$$b \pm 1.96 \sqrt{\frac{MSE}{\sum\limits_{i=1}^{N} (L_{ref,i}^{k})^2}}$$

Following Equation 4 the new estimate for the calibration coefficient $A_{cal}^{k,new}$ is then calculated, as

$$A_{cal}^{k,new} = \frac{A_{ref}^{k}}{b}$$

4.8 Multi-angular/Equalization

4.8.1 Introduction

The sensitivity of the detector response is not constant over the complete field of view. In order to correct for the sensitivity variations, they first have to be accurately characterized. This is the goal of multi-angular calibration and equalization.

The variations in detector response have two main causes:
1. variations in the sensitivity of individual pixel responses. This is a well known phenomenon, typical for all solid state detectors.
2. variations over the field of view: the optical transmission which slightly decreases for larger viewing angles;

They manifest themselves as different effects on different spatial frequencies. The concept is illustrated in Figure 36. Therefore they can studied in separate components:
1. a high frequency component (HF)
2. a low frequency component (LF)

The LF corresponds to the variations in optical transmission, which can be described by a polynomial. The HF only refers to the variations over individual pixels.
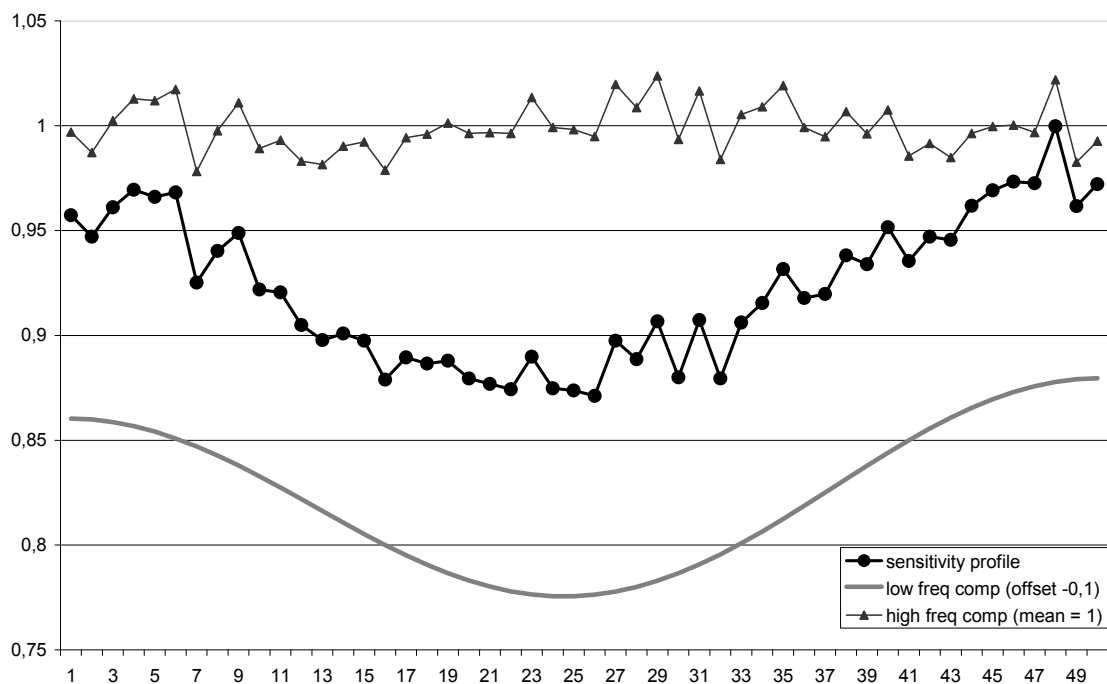

Figure 36: Sensitivity profile decoupled into high and low frequency components

The general approach to estimate the sensitivity variations is to image targets that are very uniform so that observed variations reflect sensitivity variations rather than target variations.

Target uniformity is never perfect: the uniform reflectance of the targets is disturbed which can be described as consisting of random noise and some structure. A measurement will always show the non-uniformity of the targets combined with the sensitivity variations. This is depicted in Figure 37: the same surface imaged by 2 different parts of a detector (with if non-uniformity profile) yields different results.

To even out the non-uniformity, averaging over many measurements is performed on two levels.: By summing over all pixels obtained sequentially in the along –track direction, we have **within target averaging**. This decreases the noise of the target and the structural non-uniformity in the along-track direction. However structural non-uniformity in the across track

direction will persist despite the averaging. To alleviate this; **averaging over multiple targets** will be performed. The structural target non-uniformity will then also be averaged out.
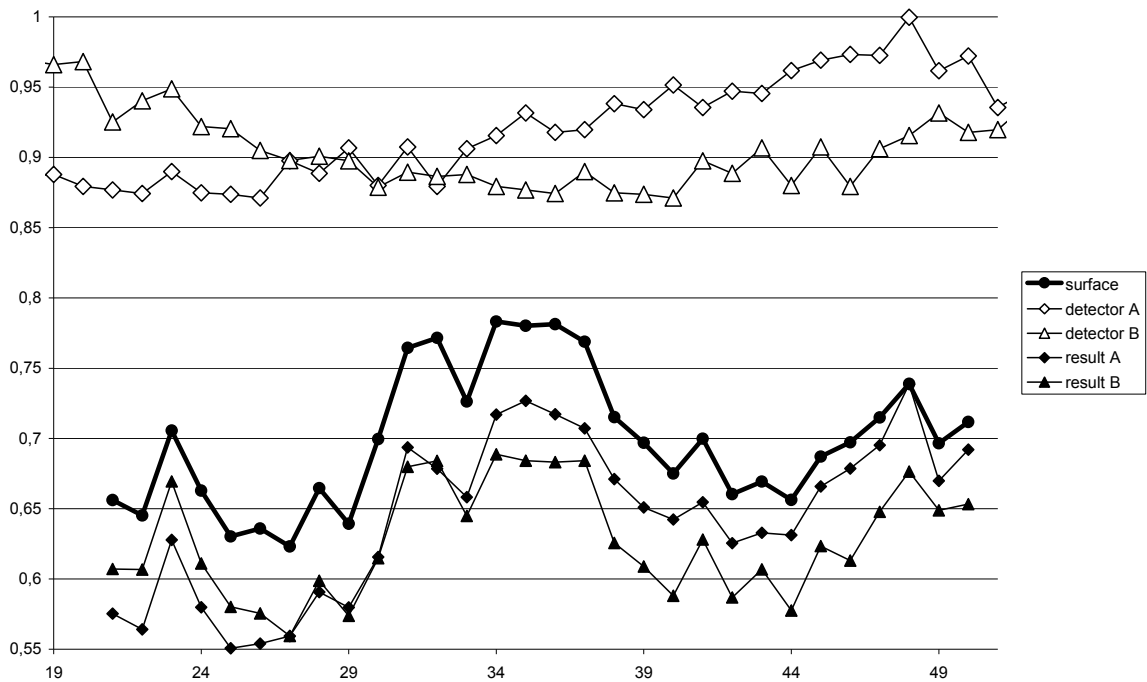

Figure 37: Surface profile, two detector sensitivity profiles and the combined results results

The best estimates for the different frequency contributions (LF, MF, HF) are obtained by a combination of different methods. The LF can be reliably obtained using desert sites because for those sites, accurate directional reference data can be obtained using BRDF models. The MF and HF components will be estimated from measurements obtained over Antarctica.

4.8.2 Theoretical background

4.8.2.1 Sensitivity profiles

The sensitivity variations can be noted as: **g(n)** , where **n** represents the sensor pixel number. The **g(n)** are normalized so that over the profile they have an average value of 1:

$$\sum\nolimits_{(n\,=\,0,N-1)} \mathbf{g(n) = N}$$

For images acquired with the imaging system, any observed image line: **f(n),** is in fact the product of the image line for a perfectly flat sensitivity profile **f'(n)** and the sensitivity profile **g(n):**

$$\mathbf{f(n) = g(n) \,.\, f'(n)}$$

f'(n) is assumed to contain no variations explicitly related to the pixel index **n**, only variations coming from the image content.

4.8.2.2 Low and high frequency variations

The estimation of the complete function **g(n)** will be more difficult as it consists of different contributions. Physically it is the result of several different causes: optical effects which cause slow variations over the FOV and properties of individual pixels, which vary from one pixel to

the next. It is therefore justified to split up the sensitivity profile in to a low frequency and a high frequency part:

$$g(n) = g\_low(n) \cdot g\_high(n)$$

The separation between the two can be made by a suitable frequency filter. If we define a low pass filter **LOW().** We can then divide the components as follows:

$$g\_low(n) = LOW (g(n))$$
$$g\_high(n) = g(n) / g\_low(n)$$

The filter should be chosen in a way as to facilitate the estimation of the separate parts, each using their own techniques and images.

We can use a simple convolution filter in the spatial domain. Then the filter is as follows:

$$LOW (g(n)) = g(n) \otimes \prod (a,b)$$

in which $\prod (a,b)$ represents a boxcar function which equals 1/(b-a) inside the given interval, and 0 outside of the interval. Such a filter, a convolution of the profile with a flat function of 17 pixels wide, was used in the experiments using Antarctica further on.

However, such a filter has some drawbacks. Therefore, it would be better to use a well designed frequency space filter (as known from digital signal processing) such as the Hanning filter. This will result in a more favourable splitting of high and low frequency components.

4.8.2.3 Estimating sensitivity profiles

The estimations of **g(n)** will be based on observed image lines. For the estimations, only the pixel index **n** is of importance, so the estimation can be worked out one-dimensionally.

Since image content and sensitivity are inevitably combined, the **g(n)** cannot be retrieved from a single line or a single image. However, if a collection of images and image lines is used, the image content variations can be averaged out. The **g(n)** variations however are tied to pixels so they do not average out.

For the estimation of the sensitivity profile **g(n)** we use a large collection of **k** image lines (collected from a set of images):

$$\{ f(n) \}\_k \qquad or \qquad \{ g(n) \cdot f'(n)\}\_k$$

The difficulty is that the sensitivity variations **g(n)** can only be observed together with image content variations **f'(n)**

A successful estimation of **g(n)** w will need to cancel out the effects of image content. It is preferably based on a combination of two aspects:

- avoiding image content variations by imaging homogeneous areas
- averaging out remaining variations in a scheme in which many independent images are combined.

Because of the different frequency components in **g(n),** it is best to perform its estimation using two separate methods and separate imagery for the high frequency variations **g_high(n)**, and for the low frequency variations **g_low(n).** Then, images can be used with properties which are better suited for the estimation of one type. Finally the results of both estimations need to be combined as to achieve one estimate for the complete sensitivity profile:

In the following we assume a perfect filter: Estimation of **g_high(n)** starts from:

$$f(n) = g\_high(n) \cdot g\_low(n) \cdot f'(n)$$

We take the low pass part of this:

$$\text{LOW} \; (\; f(n) \;) \; = \; \text{LOW} \; \big(\; g\_high(n) \, . \; g\_low(n) \, . \; f'(n) \; \big)$$

For a perfect filter, this results in:

$$\text{LOW} \; (\; f(n) \;) \; = g\_low(n) \, . \; \text{LOW} \; \big(f'(n) \; \big)$$

And the complementary high pass signal:

f(n) / LOW (f(n)) =

$$= (\; g\_high(n) \, . \; g\_low(n) \, . \; f'(n) \; \;) \; / \; g\_low(n) \, . \; \text{LOW} \; \big(f'(n) \; \big)$$

$$= g\_high(n) \, . \; f'(n) \; \; / \; \text{LOW} \; \big(f'(n) \; \big)$$

Thus the signal we intend to estimate is:

g_high(n) = $(\; f(n) \, /) \, . \; (\text{LOW} \; \big(f'(n) \; \big) \; / \; \; \text{LOW} \; (\; f(n) \;))$

or:

g_high(n) = $(\; f(n) \; / \; \text{LOW} \; (\; f(n) \;)) \; \;) \; \; . \; \; (\text{LOW} \; \big(f'(n) \; \big) \; / \; \; f'(n) \; \;)$

Now if the collection of images areas can be chosen in such a way that for after overall averaging,

f'(n) $\approx$ **LOW** $\big(f'(n) \; \big)$

This means that if the images either have to have no sifgnificant high frequency features or they need to be canceled out by averaging. This is much easier to achieve than having all features cancelling out.

If this is achieved, a good estimation of **g_high(n)** can easily obtained by averaging out the **f(n) / LOW (f(n)))** over the available collection of image lines.

A similar estimation can be made for the low frequency components using images with very little low frequency content.

4.8.2.4 Choice of images

The method explained above allows estimation of the high frequency part of a sensitivity profile using suitable images. Ideal targets for this can be over the DOME-C site on Antarctica. The extensive snow fields are contain only minimal high frequency content.

However, these images are completely unsuitable for the estimation of the low frequency variations, as the images over Antarctica exhibit very strong BRDF effects. For the low frequencies, we will therefore use different image types. Most suitable for this will be either images of Deep convective clouds or Rayleigh scattering images

4.8.3 Algorithms

4.8.3.1 Sensor data collection

The multi-angular calibration will use data acquired from the desert sites for the determination of the LF component. For the HF and MF components, data acquired over Antarctica will be used.

The calibration requires a good characterization of directional variation of the TOA reflectance. During a period of about one month most, of the deserts sites will be viewed by all the detectors. For each camera a polynomial function will be fit through the ratio of measured TOA

reflectance to modelled TOA reflectance of a given desert site as a function of viewing angle. This approach has been applied by CNES for Polder (Hagolle et al., 1999 [LIT3]) and VGT. We will now describe in detail the steps of the algorithm.

4.8.3.1.1 Data collection

The desert sites listed in Table 14**Error! Reference source not found.** are the areas of interest. For each of them, the image data needs to be collected from the image segment, as digital numbers as captured by the sensor for the different spectral bands.

Additionally, some ancillary data will be stored. This includes:
1. identification of the segment
2. applicable gain
3. absolute calibration coefficient.
4. average altitude

Some information about the atmospheric and meteorological conditions of the sites are also needed. Therefore it is necessary to collect for (the centre of) every site following measurements:
5. water content
6. ozone content

Every desert is defined as a rectangular area described by the precise geographic coordinates of the four corners. For every spectral band; the coordinates are converted to pixel coordinates on the segment .In general they do not form a regular rectangle. We construct an **enclosing rectangle** in pixel coordinates, as depicted in Figure 38 and store that for convenient access.
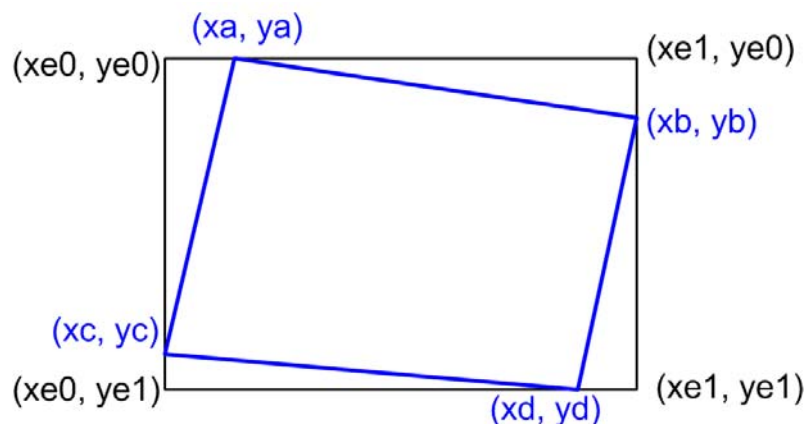
Figure 38: enclosing rectangle in image coordinates for a rectangle in geographic coordinates

4.8.3.1.2 Data processing

1. **Clean up data:**

Unusable pixels need to be identified. A pixel is unusable if it is saturated or potentially cloudy. If a site contains too many cloudy pixels, it is discarded completely.

2. **Average Data:**

For every detector (pixel along the line of the sensor) with coordinate falling into the enclosing rectangle, calculate the **line segment to average.** These can be obtained by calculating the intersection points between the lines that form the rectangle of the site, and the lines imaged by a single detector. Different cases of such line segments are shown in Figure 39.
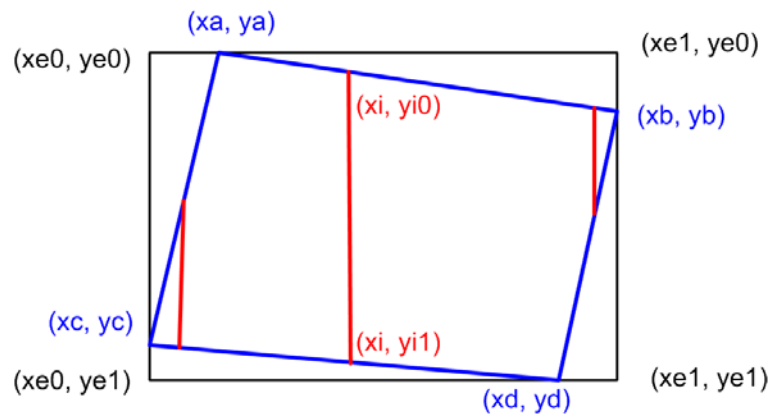
Figure 39: line segments to average within the rectangle of interest

Once the line segments have been defined, the averaging is performed by simple summation over the line segments (with x= i as line number, and y running from y_{i0} to y_{i1}

$$\langle DN_i \rangle = \frac{1}{(y_{i1} - y_{i0})} \sum_{y=y_{io}}^{y_{i1}} DN(i, y)$$

The average results are stored, together with the number of lines over which is averaged.

4.8.3.1.3 Radiance computation

The DN values can be converted radiance using the standard inverse sensor radiometric model (cfr. section 4.2.2), using the following relation :

$$L_{TOA,i}^k = \frac{DN_{i,acquired}^k - NL_g^k(DN_{i,acquired}^k) - off_{i,g}^k - dc_{i,g,T}^k\left(IT + dIT^k\right)}{A_T^k \cdot g_{i,g}^k\left(IT + dIT^k\right)}$$

4.8.3.1.4 Conversion between radiance and TOA reflectances

The relation between the TOA reflectances $\rho_{TOA,j}^k$ and the radiances $L_{TOA,j}^k$ was explained in section 4.4.1.2.1.1. When all other variables are kept constant, both quantities are proportional. The relation between the two can also be written as:

$$L_{TOA}^k = \frac{1}{\pi} \rho_{TOA}^k E_0^k \cos(\theta_s)\left(\frac{d_0}{d}\right)^2$$

The conversion depends on the solar zenith angle θ_s for every detector. They are computed using bilinear interpolation from the solar zenith angles provided in the ancillary data of the segment. The TOA reflectance is corrected for gaseous transmittance as described under section 4.4.1.2.1.2.

4.8.3.2 Reference data computation

The principle behind the determination of the equalization coefficients is the comparison between reflectances obtained from sensor measurements and modelled reference reflectances. The computation of the reference radiances is explained in 4.4.4.2.1.

4.8.3.3 Computation of equalization coefficients

4.8.3.3.1 Ratio of in-flight versus pre-flight

Given the measured and modelled reflectances, we can compare them to derive equalization coefficients. We recall that the DN is proportional to the $L_{TOA,}^k$ the precise relation (for the nominal gain, ie. AVG_g=1) is :

$$DN_{j,acquired,g,T}^{k} - NL_g^k - dc_{i,g,T}^{k}\left(IT + dIT^k\right) - off_{i,g}^k = L^k . A_T^k \cdot \left(IT + dIT^k\right)g_{i,g}^k$$

This relation holds with the absolute calibration coefficient $A_{preflight}^k$ and the equalization coefficients $g_{j,g,\,pre\text{-}flight}^k$ as determined before the launch.

In flight, we can calculate from the measured DN and the pre-flight coefficients, the $L_{jm,\,pre\text{-}flight}^k$ and the $\rho_{j,g,\,preflight}^k$. On the other hand we have the modelled $\rho_{j,g,\,inflight}^k$ values. We take the ratio between the two:

$$\frac{\rho_{jg,in\text{-}flight}^{k}}{\rho_{jg,pre\text{-}flight}^{k}} = \frac{L_{jg,in\text{-}flight}^{k}}{L_{jg,pre\text{-}flight}^{k}}$$

$$= \frac{\left(DN_{j,acquired,g,T}^{k} - NL_g^k - dc_{i,g,T}^{k}\left(IT + dIT^k\right) - off_{i,g}^k\right)\left(IT + dIT^k\right)A_{pre\text{-}flight}^{k}\, g_{jg,pre\text{-}flight}^{k}}{\left(DN_{j,acquired,g,T}^{k} - NL_g^k - dc_{i,g,T}^{k}\left(IT + dIT^k\right) - off_{i,g}^k\right)\left(IT + dIT^k\right)A_{in\text{-}flight}^{k}\, g_{jg,in\text{-}flight}^{k}}$$

Thus the ratio of the in-flight vs the pre-flight calibration coefficients is given by the ratio of the reflectances:

$$R_{jg}^k = \frac{A_{in\text{-}flight}^{k}\, g_{jg,in\text{-}flight}^{k}}{A_{pre\text{-}flight}^{k}\, g_{jg,pre\text{-}flight}^{k}} = \frac{\rho_{jg,pre\text{-}flight}^{k}}{\rho_{jg,in\text{-}flight}^{k}}$$

It is useful to plot the ratio R_{jm}^k as a function of the angle.

4.8.3.3.2   Equalization profiles of the detectors

In the previous result the absolute calibration coefficient A^k and the variations at all different frequencies are combined. The equalization coefficients g_{jg}^k contain these variations, which were categorized before into HF, MF and LW components. We can split the equalization into a high, medium and low frequency part:

$$g_{jg}^k = ghf_{jg}^k\, gmf_{jg}^k\, glf_{jg}^k$$

If we assume that two of the three terms have been characterized using other means, we can determine the remaining term.

4.8.3.3.3   Determination of the low frequency term : polynomial fit

The low frequency terms glf_{jg}^k should model the slow variations due the optics. It is good practice to model these variations with a function with a limited number of parameters. We propose to use a fifth degree polynomial:

$$R_{jg}^k \approx RPoly_{jg}^k = \sum_{p=0}^{5} r_{g,p}^k\, j^p$$

The coefficients $r_{g,p}^k$ are optimised to minimize the quadratic difference between R_{jm}^k and $RPoly_{jg}^k$. This polynomial regression is obtained by using a standard technique for general least squares optimisation, as explained in (Press et al, 2007, [LIT45]). This results in a smoothly varying function.

The residues, not modelled by the polynomial, show high frequency variations. However, these can be disturbed by artefacts caused by the non-uniformities in the desert targets. Because of this; they are not sufficiently accurate to be used for determining the gm_{jg}^k and gh_{jg}^k coefficients. Therefore, will will estimate these coefficients with other target, namely over Antarctica.

4.8.3.3.4   Outlier handling

A concern with least squares optimisation is that its results can be easily disturbed by outliers. For the initial pre-flight determination of glf_{jg}^k, special care must be taken to remove any outliers by manual inspection.

The in-flight low frequency variations can be assumed to be at most slowly varying over time. Therefore we can do the following:
- normalize the in-flight $gl^k_{jg,}$ by dividing them by the pre-flight or previous in-flight $RPoly^k_{jg}$
- calculate the mean and standard deviation of the normalized values (averaged over all angles) and determine a confidence interval around the mean
- all values outside of the confidence interval are assumed outliers and marked
- The new in-flight polynomial is calculated without using the outlier points

4.8.3.4　High and medium frequency (Antarctica)

The high and medium frequency terms can be assessed during flight using a statistical approach. The idea is to average over enough measurements so that the high frequencies stemming from the targets are effectively averaged out.

This can be best achieved with large, bright targets that have only limited high frequency content. Extensive snow covered areas over Antarctica are well suited for this. The DOME-C site, already presented in section 4.5.4.1.3 will used.

The image acquisition will be done as outlined in section 4.5.4. The area is not part of normal operational imaging, so additional dedicated acquisitions with special settings need to be performed for several orbits a day. This can only be done during local summer, which limits the usability of the method.

The images are averaged out over the lines in the same way as in section 4.8.3.1.2. The result contains variations at all frequencies. The low frequencies, which reflect both the target and the imaging variations, need to be separated and removed. This is done by constructing a polynomial model of the data, in the same way as proposed in 4.8.3.3.3 The data is normalized by the model values, so that low frequency variations are removed.

The result still contains both high and medium frequencies. They both need to be applied in the process of multi-angular equalization. There is no explicit need to separate the components.

However, in order to analyse the results and their evolution over time, it is useful to separate the terms .This can be done with standard signal processing techniques: the high frequency part can be isolated well by applying a Hanning filter in frequency space, as proposed in (Fougnie et al 2000,[LIT46]).

4.9   Performance Indicators

As there is no on-board light source available on PROBA-V, an assessment of the instrument's image quality in flight will have to be done using ground targets. To determine instrumental noise effects on the measured signals, ground targets should be spectrally uniform over the measured range. As established elsewhere in this document, ground targets such as desert zones or snow zones are considered as uniform zones. To determine image contrast, here done by measuring instrument system MTF, ground targets should have features of high contrast.

4.9.1 Noise analysis

4.9.1.1   Background

When an image is captured, noise measurements are affected both by the noise effects caused by the instrument capturing the image, as well as by variations in the image itself. To isolate the influence of these image variations, one needs to perform the noise analysis over selected zones which are spectrally uniform with respect to the instrument band considered in the analysis. These uniform zones typically only comprise a sub-region of an entire image, for an instrument with a low resolution and large swath such as PROBA-V. Therefore, to estimate noise over the full FOV, multiple zones need to be selected. A noise analysis is complete only when a sufficiently uniform zone is found and processed for each band, and this for the entire FOV. Aside from image noise, several different noise influences can be analysed. These are discussed in section 4.9.1.3. In section 4.9.1.2, the different statistical methods of analysis are described.

4.9.1.2   Noise analysis methods

- **Averaged pixel value:** over different scan lines of the same uniform zone, a pixel value should be more or less the same. Therefore, the averaged pixel value is a useful measure:

$$\mu_p = <L_{p,l}>_l$$

- **Noise over pixel value**: deviations of different scan lines with respect to the averaged pixel value are a measure of the uniformity of the captured values, and therefore of the noise:

$$\sigma_p = RMSE_l(L_{p,l} - \mu_p) = \sqrt{<(L_{p,l} - \mu_p)^2>_l}$$

- **Averaged region value**: over different scan lines of different pixels covering a uniform region, all averaged pixel values should be more or less the same. Therefore, the average over all pixels in that region, or over all non-overlapping zones covering that region, and lines is a useful measure:

$$\mu_{region} = <L_{p,l}>_{p,l} = <\mu_p>_p$$
$$= <\mu_z>_z$$

- **High Frequency (HF) noise over region value**: a measure of the HF noise over an entire region with respect to subdividing zones is the RMSE of the noise over zone of pixel values covered in that region:

$$\sigma_{HF,region} = RMSE_z(\sigma_z)$$

- **Low Frequency (LF) noise over region value**: a measure of the LF noise over an entire region with respect to subdividing zones is the RMSE of the deviations of averaged zone values with respect to the averaged region value.

$$\sigma_{LF,region} = RMSE_z(\mu_z - \mu_{region})$$

- **N-centred average**: this determines the centred average (average including centre) for a neighbourhood of N pixels:

$$\mu_{p,centerN} = \frac{1}{N+1} \sum_{j=p-N/2}^{p+N/2} \mu_j$$

- **N-neighbourhood average**: this determines the local average (average surrounding centre) for a neighbourhood of N pixels:

$$\mu_{p,localN} = \frac{1}{N} \sum_{\substack{j=p-N/2 \\ j \neq p}}^{p+N/2} \mu_j$$

- **N-centred deviation**: this determines the deviation of a averaged pixel value with respect to the N-centred average value:

$$\sigma_{p,centerN} = \mu_p - \mu_{p,centerN}$$

- **N-neighbourhood deviation**: this determines the deviation of a averaged pixel value with respect to the N-neighbourhood average value.

$$\sigma_{p,localN} = \left| \mu_p - \mu_{p,localN} \right|$$

- **Maximum N-neighbourhood deviation over region value** : This determines the maximum neighbourhood deviation over a region. This is a measure of the local noise:

$$\sigma_{region,localN} = \max_p (\sigma_{p,localN})$$

Crucial remark: For N-centred and N-neighbourhood measures, a problem arises at the border of an image, because fewer than N neighbours can be reached. Therefore, for border pixels the local means are calculated over the useful pixels of the image, and N is reduced accordingly.

4.9.1.3 Noise influences

A noise analysis is performed for each spectral band separately. The following noise influences need to be distinguished:

- **Image noise**, or noise related to the ground target or object scene being measured. This noise can be determined by averaging over the measured values of spectrally uniform subsets of the image, and also calculating the noise terms over these subsets. The high-frequency (HF) noise over the entire image then determines the noise induced by the image. The low-frequency (LF) noise can also be calculated, this is a measure of the uniformity of the image zone considered.
- **Inter-column noise**, or deviations between pixels. This will include discontinuity effects such as defective or degraded pixels. To examine this, first the averaged pixel values are calculated, and then, the average and deviation of each averaged pixel with respect to its nearest neighbours is calculated. The maximal deviation measured over pixels of the entire array should be limited, in order for the image to be reliable. This measure can therefore be used to mark suitable zones (i.e. zones where the maximal neighbourhood deviation is within bounds).
- **Adjacent-array noise** describes the noise effect caused by the merging of different arrays to form one line of pixels. This noise will be found at the edges where array values are merged in this manner. In PROBA-V, two effects need to be distinguished, which are treated similarly. First, the butting of the SWIR arrays for each camera means that at each end of two SWIR arrays, an adjacent-array noise effect results. Second, the overlap of one camera to the next will result in another adjacent-array noise effect, and this for each band. Such noise can be measured by calculating the mean time-averaged signal for a neighbourhood of pixels at one edge in the first array, and calculating the mean time-averaged signal for a neighbourhood of pixels at the adjacent edge in the succeeding array. The difference between both is a measure of the noise between these arrays.
- **Equalization noise** describes the differences caused by the equalization process, which is performed for each uniform subset of the image separately. Hence, in a similar approach to the inter-column noise calculation, one calculates the average and standard deviation for each pixel with respect to its nearest neighbours. Instead of evaluating these local averages over the entire array, the mean average and mean standard deviation are calculated for each uniform subset separately. In this way, the equalization differences between these uniform subsets are assessed.

- **Column noise**, or noise related to a pixel of the detector. This noise will include both the noise induced by the instrument (for each pixel separately), and the noise induced by the image. By subtracting the image noise, the pixel noise or instrument column noise can be determined.
- **Structural noise** can be detected by calculating the MTF of a time-averaged value of a uniform subset of the image. An additional analysis can be performed by taking the two-dimensional MTF of the entire uniform subset-image.

The assessment of image noise is not straightforward, as effects of atmospheric calculations and physical atmospheric variations affect the reliability of the results. As an alternative method, the calculated image noise values can also be extracted from data by other satellites (TBC).

4.9.1.4 Algorithm

4.9.1.4.1 Image noise

Input:
- A set of image subsets (Level 1C), capturing scenes with zones which are spectrally uniform over the mission's band under test. Insofar as possible, the images of these zones cover the entire FOV of the instrument.
- status list of bad pixels

Procedure:
- **Eliminate all 'bad' pixels from the zone images using the bad pixel status list.**
  - See section 4.3.2.
- **Determine for every zone, the averaged zone value and noise value**.
  - For every zone z, determine $\mu_{region=z} = <L_{p,l}>_{p,l}$
  - For every zone z, determine HF noise
    $$\sigma_{HF,region=z} = RMSE_p(RMSE_l(L_{p,l} - \mu_z))$$
- **Eliminate all zones with significantly large HF noise**.
  - First, it can be defined by the user when a noise figure is considered too large.
  - Next, all zones with HF noise larger than the user-defined limit are eliminated.
- **Determine the averaged image value and the image LF and HF noise**:
  - Determine $\mu_{region=image} = <\mu_{region=z}>_z$.
  - Determine $\sigma_{HF,region=image} = RMSE_z(\sigma_{HF,region=z})$.
  - Determine $\sigma_{LF,region=image} = RMSE_z(\mu_z - \mu_{region=image})$.

Output:
- The averaged image value is a measure of the signal level, and is used to identify whether the test describes an L1, L2, L3 or L4 equivalent radiance.
- The HF noise measure corresponds to the measured noise over the image.
- The LF noise measures the uniformity of the considered zone.

4.9.1.4.2 Inter-column noise

Input:
- A set of image subsets (Level 1C), capturing scenes with zones which are spectrally uniform over the mission's band under test. Insofar as possible, the images of these zones cover the entire FOV of the instrument.
- status list of bad pixels

Procedure:
- **Eliminate all bad pixels from the zone images using the bad pixel status list**.
  - See section 4.3.2.

- **Determine for every zone, the averaged pixel values and averaged zone value**
  - For every zone z, determine $\mu_p = <L_{p,l}>_l$.
  - For every zone z, determine $\mu_z = <\mu_p>_p$.
- **Determine for every zone the instrumental noise by subtracting LF noise**:
  - For every zone z, determine $\mu_{p,centerN} = \dfrac{1}{N+1} \displaystyle\sum_{j=p-N/2}^{p+N/2} \mu_j$. This represents the local image contribution.
  - For every zone z, determine $\sigma_{p,centerN} = \mu_p - \mu_{p,centerN}$. This represent the local instrument noise.
- **Determine for every instrumental noise, the N-neighbourhood average and deviation**:
  - For every μ_p, determine $\mu_{p,localN} = \dfrac{1}{N} \displaystyle\sum_{\substack{j=p-N/2 \\ j \neq p}}^{p+N/2} \sigma_{j,centerN}$. **Note**: bad pixels are not counted in value, but their index is used in the definition of the neighbourhood.
  - For every μ_p, determine $\sigma_{p,localN} = \left| \sigma_{p,centerN} - \mu_{p,localN} \right|$
- **Determine for every zone the maximum N-neighbourhood deviation, the local HF noise and maximum difference between N-neighbourhood averages :**
  - For every zone z, determine $\sigma_{z,localN} = \max_p(\sigma_{p,localN})$. This is a measure for the inter-column noise in this zone.
  - For every zone z, determine $\sigma_{HF,z,localN} = RMSE_p(\sigma_{p,localN})$.
  - For every zone z, determine $\sigma_{LF,z,localN} = \max_{N_z}\left(\left| <\sigma_{p,centerN}>_{N_z+1} - <\sigma_{p,centerN}>_{N_z} \right| \right)$, with N_z ranging from beginning of the zone to end of the zone in steps of N_z pixels.
- **Determine the averaged image value, maximum maximorum N-neighbourhood deviation, the maximum local HF noise, and the maximum maximorum difference between N-neighbourhood averages:**
  - Determine $\mu_{\text{intercolum n}} = <\mu_z>_z$.
  - Determine $\sigma_{\text{max,intercolumn}} = \max_z(\sigma_{z,localN})$.
  - Determine $\sigma_{HF,\text{intercolum,localN}} = \max_z(\sigma_{HF,z,localN})$.
  - Determine $\sigma_{LF,\text{intercolum,localN}} = \max_z(\sigma_{LF,z,localN})$.

Output:
- The averaged value is a measure of the signal level.
- The maximum maximorum N-neighbourhood deviation measures the maximum inter-column noise present. This measure has a conservative measure (it over-estimates the noise distributed over the considered image subsets). It can be called **the maximum intercolumn noise.**
- The maximum local HF noise measures the **nominal intercolumn noise**, as it measures the rms distribution of the local deviations. It is always lower than the maximum intercolumn noise.
- The maximum maximorum difference between N-neighborhood averages is a measure of the local LF noise; it determines the noise over a frequency of N_z pixels.

4.9.1.4.3　Adjacent-array noise

Input:
- A set of image subsets (Level 1C), capturing scenes with zones which are spectrally uniform over the mission's band under test. The images of these zones are chosen to be

centred over the region between two adjacent arrays. This can either be the region between two adjacent strips of the SWIR band, or the region between two camera's for all bands.
- status list of bad pixels

Procedure:
- **Eliminate all bad pixels from the zone images using the bad pixel status list**.
    - See section 4.3.2.
- **Determine for every array, over its border region, the averaged pixel values, and the averaged array value**
    - For every couple of bordering arrays *arr1* and *arr2*, a border region B can be

    defined, where $\begin{cases} p \in \left[p_{j-N}, p_j \right] & \textit{for arr}_1 \\ p \in \left[p_{j+1}, p_{j+M} \right] & \textit{for arr}_2 \\ B = \left[p_{j-N}, p_j \right] \cup \left[p_{j+1}, p_{j+M} \right] \end{cases}$

    - For every array *arr*, determine $\mu_p = <L_{p,l}>_l$.
    - For every array *arr*, determine $\mu_{arr} = <\mu_p>_p$.
- **Determine for every border region, the averaged border value and the LF border deviation**.
    - For every border region B, determine $\mu_B = \dfrac{\mu_{arr1} + \mu_{arr2}}{2}$.
    - For every border region B, determine $\sigma_{LF,B} = \left| \mu_{arr1} - \mu_{arr2} \right|$.
- **Determine the averaged image value, the maximum adjacent array noise and the nominal adjacent array noise.**
    - Determine $\mu_{adjacentarray} = <\mu_B>_B$.
    - Determine $\sigma_{max,adjacentarray} = \max_B (\sigma_{LF,B})$.
    - Determine $\sigma_{nominal,adjacentarray} = RMSE_B (\sigma_{LF,B})$.

Output
- The averaged value is a measure of the signal level.
- The maximum adjacent array noise is a conservative measure of the noise expected at a adjacent array crossing.
- The nominal adjacent array noise is a measure of the distribution of noise over different adjacent arrays. The difference between the nominal and the maximum noise is a measure of the discrepancy between different adjacent arrays.

4.9.1.4.4 Equalization noise

Input:
- A set of image subsets (Level 1C), capturing scenes with zones which are spectrally uniform over the mission's band under test. Insofar as possible, the images of these zones cover the entire FOV of the instrument.
- status list of bad pixels

Procedure:
- **Eliminate all bad pixels from the zone images using the bad pixel status list**
    - See section 4.3.2.
- **Determine for every zone the averaged pixel value over a fixed number (TBD 500) of lines**
    - For every zone *z*, determine $\mu_p = <L_{p,l}>_l$.
- **Determine for every zone the instrumental noise by subtracting LF noise**:

- o For every zone z, determine $\mu_{p,centerN} = \dfrac{1}{N+1} \sum_{j=p-N/2}^{p+N/2} \mu_j$. This represents the local image contribution.
  - o For every zone z, determine $\sigma_{p,centerN} = \mu_p - \mu_{p,centerN}$. This represent the local instrument noise.
- **Determine for every zone the averaged zone instrument noise, the HF zone noise**
  - o For every zone z, determine $\sigma_{instrument,z} = <\sigma_{p,centerN}>_p$.
  - o For every zone z, determine
    $$\sigma_{HF,z} = RMSE_p(\sigma_{p,centerN} - \sigma_{instrument,z}) .$$
- **Determine the average instrument noise, and the nominal image noise.**
  - o Determine $\sigma_{instrument} = <\sigma_{instrument,z}>_z$.
  - o Determine $\sigma_{nominal,equalisation} = RMSE_z(\sigma_{HF,z})$.

Output:
- The averaged instrument noise is a measure of the average local noise attributed to the instrument, under the assumption that the image experiences no noise over a local neighbourhood.
- The HF zone noise is a measure of the distribution of the average local noise over that zone. It gives a large value when the distribution is strongly fluctuating, which is an indication of bad equalization.
- The nominal image noise is a measure of the nominal equalization noise over the system.

4.9.1.4.5 Column noise

Input:
- Image subsets used in the image noise calculation. Extract from them the raw values $L_{p,l}$, the averaged zone value $\mu_{region=z}$.
- status list of bad pixels

Procedure:
- **Eliminate all 'bad' pixels from the zone images using the bad pixel status list.**
  - o See section 4.3.2.
- **Determine for every zone the averaged pixel value over a fixed number (TBD 500) of lines**
  - o For every zone z, determine $\mu_p = <L_{p,l}>_l$.
- **Determine for every zone the instrumental noise by subtracting LF noise**:
  - o For every zone z, determine $\mu_{p,centerN} = \dfrac{1}{N+1} \sum_{j=p-N/2}^{p+N/2} \mu_j$. This represents the local image contribution.
  - o For every zone z, determine $\sigma_{p,centerN} = \mu_p - \mu_{p,centerN}$. This represent the local instrument noise.
- **Determine for every zone, the global HF pixel noise value**.
  - o For every zone z, determine <u>global</u> HF pixel noise
    $$\sigma_{HF,p,region=z} = RMSE_l(L_{p,l} - \mu_z) .$$
- **Determine for every zone the pixel column noise, as being the local HF contribution not due to equalization noise. Determine the nominal zone column noise**
  - o For every zone z, determine $\sigma_{p,column,region=z} = \sqrt{\sigma_{p,HF,region=z}^2 - \sigma_{p,centerN}^2}$.

- For every zone z, determine $\sigma_{z,column} = \sqrt{< \sigma^2_{p,column,region=z} >_p}$.

- **Determine for every zone the nominal image column noise.**
  - Determine $\sigma_{column} = \sqrt{< \sigma^2_{z,column} >_z}$.

Output:
- The nominal image column noise is a measure of the column noise of the system.
- The nominal zone column noise is a measure of the column within the specified zone.

4.9.1.4.6   Structural noise

Input:
- A set of image subsets (Level 1C), capturing scenes with zones which are spectrally uniform over the mission's band under test. Insofar as possible, the images of these zones cover the entire FOV of the instrument.
- Status list of bad pixels

Procedure:
- **Eliminate all 'bad' pixels from the zone images using the bad pixel status list:**
  - See section 4.3.2.
  .
- **Interpolate values for eliminated positions**.
  - Linear interpolation of values with adjacent pixel values at places where pixels have been eliminated.
- **Determine for every zone, the 2D fast-fourier transform.**
  - For every zone z, determine $FT2(fr_x, fr_y) = FFT2_{p \to fr_x, l \to fr_y}(L_{p,l})$.
- **Determine for every zone the averaged pixel value**
  - For every zone z, determine $\mu_p = <L_{p,l}>_l$.
- **Determine for every zone, the fast-fourier transform over the averaged pixel line**
  - For every zone z, determine $FT(fr_x) = FFT_{p \to fr_x}(\mu_p)$.
- **Analyse curves**
  - Mark high frequency content,

$$\left. \begin{array}{l} FT(fr_x) \\ FT2(fr_x, fr_y) \end{array} \right\} \geq 0.3\,\sigma_{column}, \textit{for } fr = \sqrt{fr_x^2 + fr_y^2} > 0.2\,fr_{nyq} \text{ (TBC)}$$

Output:
- Signalization of structured noise when condition of high frequency content is fulfilled

4.9.2   MTF assessment

4.9.2.1   Background

A valid approach for MTF assessment is to compare MTF registration for two instruments, imaging the same scene with similar spectral content, but of different spatial resolution. PROBA-V images are of a fairly low resolution of 100 meter at best. Images of a higher resolution satellite of 30 meter or better will therefore have a much better MTF at the spatial frequency range of PROBA-V. The core assumption of this method is that the MTF of the higher resolution instrument is close to perfect, so that the MTF of the image is assumed equal to the MTF of the higher resolution instrument. The MTF of the lower resolution instrument of PROBA-V can thus be derived from this. Since the projection and resampling algorithms of the PF cannot be neglected as an MTF influence, the MTF estimation is performed on L2A images.

4.9.2.2 Algorithm

4.9.2.2.1 Image comparison technique

Step1: Select image couples

- Select a N x N image of PROBA-V Level 2A together with a higher resolution image over the same region. The higher resolution instrument should have similar spectral response curves compared to PROBA-V to have a good comparison. A difference in atmospheric conditions present when the images are captured also affects the results. This can be avoided by using images acquired at about the same time (near-overpasses) and selecting regions which experience stable atmospheric conditions.

Resample higher resolution image to fraction of PROBA-V resolution

- Resample higher resolution image such that:

$$pixelsize_{High\,Res} = \frac{1}{R_x} x \frac{1}{R_y} \; pixelsize_{Low\,Res}$$, where R_x and R_y are integer values, with

a minimum value of 10 .

- Match pixel and line shift of Higher resolution image by correlating the two images (matching their features). Apply pixel and line shift such that both images are registered in the same (p,l)-grid.

Apply 2D Fast-Fourier Transform to both images

- Determine $FT2_{High\,Res}(fr_x, fr_y) = FFT2_{p \to fr_x, l \to fr_y}\left(L_{High\,Res}(p,l)\right)$. The transform is done on R_x*N x R_y*N points.
- Determine $FT2_{Low\,Res}(fr_x, fr_y) = FFT2_{p \to fr_x, l \to fr_y}\left(L_{Low\,Res}(p,l)\right)$ The transform is done on N x N points.
- Take the magnitude of these Fourier spectra and normalize by DC component

$$MTF2_{High\,Res}(fr_x, fr_y) = \frac{\left|FT2_{High\,Res}(fr_x, fr_y)\right|}{\left|FT2_{High\,Res}(0,0)\right|}$$

$$MTF2_{Low\,Res}(fr_x, fr_y) = \frac{\left|FT2_{Low\,Res}(fr_x, fr_y)\right|}{\left|FT2_{Low\,Res}(0,0)\right|}$$

- The corresponding Fourier spectra need to be known at N x N frequencies. Points for which the High Res spectrum is 0 are interpolated by taken the mean of its neighboring values.

Determine Ratio of MTFs

- Determine the ratio of image MTFs. This is a measure of the degradation of the PROBA-V instrument wrt the higher resolution performance. This higher resolution performance can be assumed to be quasi-ideal at the frequencies of PROBA-V

$$MTF2_{system}(fr_x, fr_y) = \frac{MTF2_{Low\,Res}(fr_x, fr_y)}{MTF2_{High\,Res}(fr_x, fr_y)}$$

4.9.3 SNR calculations

4.9.3.1 Background

The calculations of signal-to-noise-ratio (SNR) for each pixel is equivalent to the approach used to calculate the column noise terms. The averaged pixel value can be taken as the signal per pixel. This provides an estimation of the SNR due to the instrument alone.

4.9.3.2 Algorithm

Input:
- Image subsets used in the column noise calculation. Extract from them the averaged pixel values μ_p , and the pixel column noises $\sigma_{p,column,region=z}$.

Procedure:
- **Determine for every zone the SNR per pixel, defined as the ratio of signal over noise**:
  - For every zone z, determine $SNR_p = \dfrac{\mu_p}{\sigma_{p,column,region=z}}$.
- **Determine for every zone the minimum zone SNR, the average zone SNR and the distribution on the zone SNR**:
  - For every zone z, determine $SNR_{z,\min} = \min_p(SNR_p)$.
  - For every zone z, determine $\mu_{z,SNR} = <SNR_p>_p$.
  - For every zone z, determine $\sigma_{z,SNR} = RMSE_p(SNR_p - \mu_{z,SNR})$.
- **Determine the guaranteed SNR, the average SNR and the SNR distribution**.
  - Determine $SNR_{\min} = \min_z(SNR_{z,\min})$.
  - Determine $\mu_{SNR} = <\mu_{z,SNR}>_z$.
  - Determine $\sigma_{SNR} = RMSE_z(\sigma_{z,SNR})$.

Output:
- The guaranteed SNR is a measure for the minimal radiometric resolution of the instrument.
  - The average SNR and SNR distribution are useful as auxiliary specification of the overall radiometric resolution of the instrument.
  - The zone SNR specifications are similar measures, applied only to a specific zone, and are also useful as auxiliary specifications.

The SNR per pixel is a useful measure of the radiometric resolution given for each pixel.

4.10 Calibration Validation

In the previous sections the theoretical basis and processing steps of a number of PROBA-V radiometric calibration methods are described. This section describes the validation approach of the radiometric calibration using independent means like a comparison to other space-borne sensors (described in section 4.10.1), ground-based measurements (described in section 4.4.2) and APEX underflights (described in section 0).

The Committee on Earth Observing Satellites (CEOS) defines validation as the process of assessing, by independent means, the quality of the data products derived from the system output. One can distinguish 3 stages in validation (NASA's validation hierarchy) :

- Stage 1: Product accuracy has been estimated using a small number of independent measurements obtained from selected locations at particular times. Some ground data collection involved.
- Stage 2: Product accuracy has been assessed over a widely distributed set of locations and at a number of times via several ground data collection and validation efforts.
- Stage 3: Product accuracy has been assessed and the uncertainties in the product well established via independent measurements in a systematic and statistically robust way representing global conditions.

As quantitative information will be deduced from PROBA-V images and temporal analysis is crucial, a Stage 3 validation of the radiometric calibration is needed.

We distinguish pre-launch and post-launch validation activities:

Pre-launch validation activities include 1) the verification of radiometric calibration algorithms and 2) the characterization of error budget.

During the pre-launch phase, the radiometric calibration algorithms will be tested and verified by applying them to

- **VEGETATION archive data available at VITO.** For radiometric calibration, before launch, a number of SPOT-VGT scenes over Antarctica, deserts, sun glint, deep convective clouds areas and Rayleigh sites will be processed using the PROBA-V algorithms. The retrieved calibration parameters will be compared to the values in the calibration parameter files. The aim is to validate the core of the algorithms including the RTF calculations with 6SV and/or Libradtran, assumptions made on surface properties (e.g.desert BRDF model and parameters), etc. using real satellite data from a spectrally similar sensor. These algorithm cores can be considered as 'generic' for spectrally similar sensors.

- **simulated PROBA-V images generated by the System Performance Simulator**: For radiometric calibration, before launch, simulated PROBA-V images generated by the System Performance Simulator will be used as a supporting verification strategy. The aim is:
  ✓ to evaluate and quantify the sensitivity of the vicarious calibration algorithms to specific PROBA-V radiometric uncertainty sources (e.g. noise, compression, temperature dependencies ...)
  ✓ to validate those radiometric IQC algorithms for which no comparable SPOT-VGT data exist (e.g. camera-to-camera calibration, linearity checks)
  ✓ to validate that the IQC workflow can process images from PF (via the Central DataBase). The SPS will generate images in a format that can be converted into a L1A or L1B. This can be registered as input data in the central data base which can be read by IQC.

For the different radiometric calibration methods described and prototyped, the error budget is determined following this approach: the prototypes are run taking into account the uncertainty

of a number of input parameters (e.g. aerosol model). The output of the prototypes is analysed statistically to determine the error budget associated with this uncertain input parameter.

Post-launch validation of radiometric calibration methodology includes 1) refinement of algorithms and 2) uncertainty evaluation. During the post-launch phase the radiometric calibration algorithms will be tested and refined with PROBA-V data. A consistency analysis for the various algorithms will be performed with PROBA-V and a cross-sensor comparison will be made. Furthermore ground-based measurements and APEX underflights will be performed at an ad hoc basis to validate the radiometric calibration coefficients by independent means. The radiometric calibration algorithms often are based on radiative transfer code which necessitates a number of input parameters that are uncertain. In case of reflectance-based methods, in-situ reflectance measurements of homogeneous reference sites acquired simultaneously with the satellite overpass also introduce errors and the accuracy of this reflectance-based method is smaller than the radiance-based methods (Fox, 2004 [LIT47]). By applying the radiometric calibration methods systematic or random errors are introduced. Random errorsare minimized by averaging a large number of measurements. During validation systematic errors in one or more methods introduced by e.g. target BRDF or aerosol load can be detected by consistency analysis of the various absolute and relative radiometric calibration methods and by comparing multiple sensors (cross-sensors).

4.10.1 Cross-sensor calibration over stable deserts

4.10.1.1 Introduction

Cross sensor calibration is the term used for describing calibration methodology which employs data from sensors from other satellite systems, which is called "exogenous data".

Because the other systems can be assumed to be calibrated well, this is a valuable addition to the methods acting on the data of the satellite itself. Also, it is of great interest to obtain calibrations that are in line with those of other systems, especially with well established systems. For PROBA-V this is even more important as the prime goal of the mission is to provide proper data continuity and consistency with VGT. This makes proper cross sensor calibration between VGT and PROBA-V essential.

The most straightforward way to perform cross-sensor calibration would be to use simultaneous observations of the same location using different sensors. This is often not realizable in practice, therefore observations taken at different times have to be used. The different time implies different conditions; therefore a methodology to map observations to a common standard is needed. This can be borrowed from other calibration methods (multi-temporal calibration). It requires the use of stable test sites such as deserts (or Antarctica).

If we want to compare observations form different sensors, in general we will have to take into account following elements that cause differences:

Differences between the imaging instruments:

- spectral responses of the several band can differ: this may require spectral resampling/adjustment

- instrument geometry, instrument resolution

Differences stemming from the acquisition: different timing:

- Different atmospherical conditions

- Difference in geometry: different sun angles causing different illumination of the surface

- Not exactly the same surface area is imaged

- Slight instability of the site.

We will now describe a methodology to bridge the gap between the PROBA-V and exogenous or reference data. The procedure is schematically geven in Figure 40. It mainly consists of the following steps : (1) creation of reference database (including cloud detection, atmospheric correction and averaging), (2) preparation of the PROBA-V data (ie. Preprocessing, cloud detection, atmospheric correction and averaging), (3) Finding Comparable observations, (4) Spectral adjustment of reference reflectance spectra to the PROBA-V spectral bands and (5) Data comparison to retrieve the cross-sensor calibration coefficient.

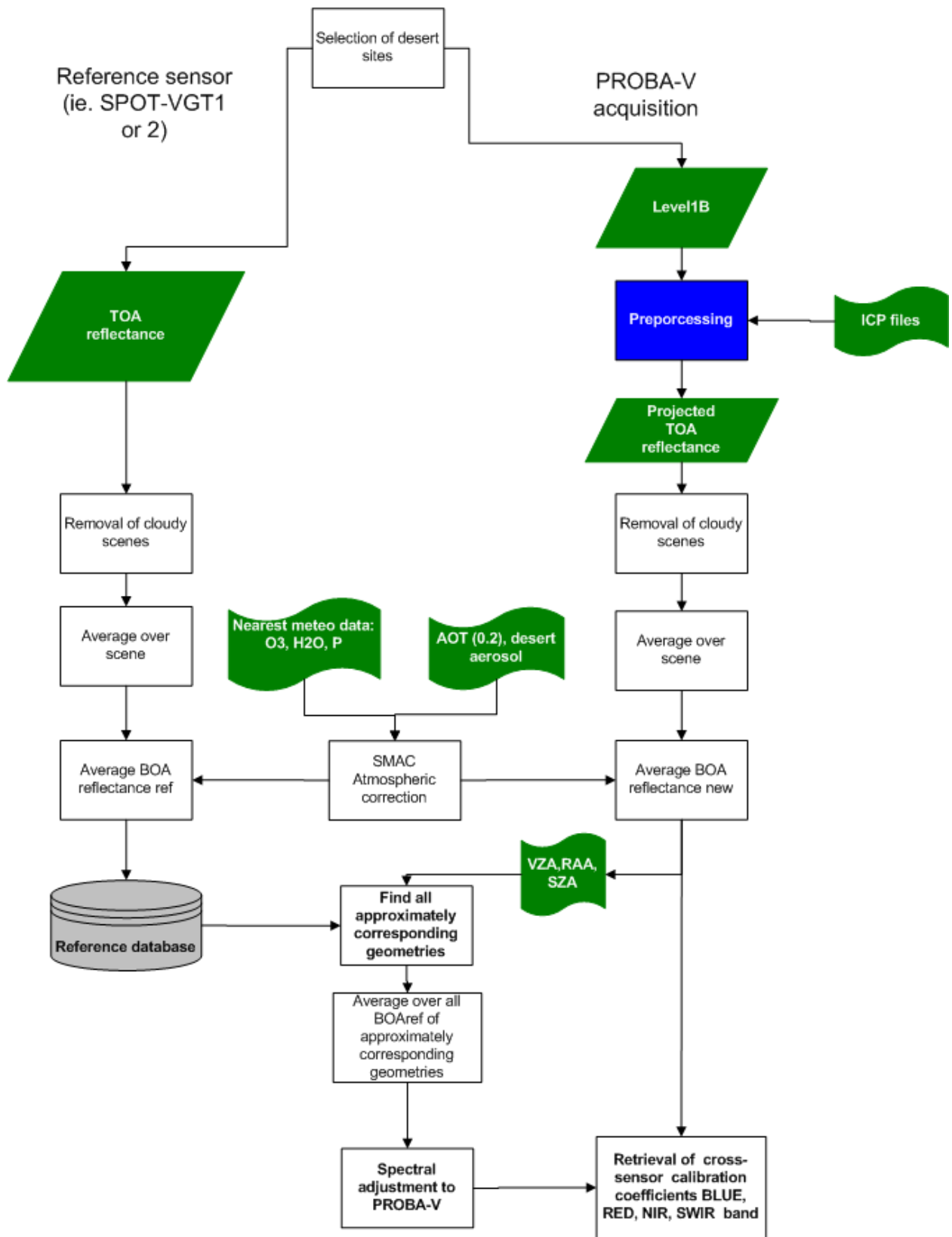The different steps are described in detail in the following paragraphs.

Figure 40: Cross sensor calibration overview

4.10.1.2 Algorithmic implementation

4.10.1.2.1 Creation of reference database

For the creation of the BOA reflectance database of the reference sensor (ie SPOT-VGT1 or SPOT-VGT2) the procedures (steps b to e) described under section 4.5.3.2.1 needs to be applied.

4.10.1.2.2 Preparation of PROBA-V data

Following the procedures described under section 4.5.3.2.1 (steps a to d) the average BOA reflectance for each site ($\overline{\rho}_{BOA}^{new}$) is obtained from the DNs per pixel.

4.10.1.2.3 Finding Comparable observations

For every PROBA-V observation, we search through the datasets of available exogenous observations (i.e. from SPOT-VGT) for comparable observation, similar to the procedure described in section 4.5.3.2.2. .If several acquisitions from a certain sensor match the criteria, the average is retained after outlier selected. This gives $\rho_{BOA,g}^{k,meas,VGT}$. In order to remove the outliers in the reference observations the results of deserts absolute calibration is used. If the absolute calibration differs more than 20 % from 1 the observation is not used in the mean calculation..

4.10.1.2.4 Spectral adjustment: Conversion from exogeneous to PROBA-V sensor characteristics

Starting from pairs of observations, the general idea is to process the reference sensor data in order to generate reflectance data as would be obtained by the PROBA-V sensor. In case the PROBA-V spectral response curves significantly differ from those of SPOT-VGT a spectral resampling/adjustment of the BOA reflectance spectra will be needed to correct for differences in spectral sensitivities between the reference sensor and the PROBA-V sensor.

For this we will use the Rahman-Pinty-Verstraete (RPV) BRDF model parameters in function of wavelength for each site.

First, the theoretical desert spectrum in function of wavelength ($\rho^{model}(\lambda)$) is calculated for site g with the RPV BRDF model for the corresponding sun and viewing geometry and spectrally resampled to the spectral response curves of each band of the reference sensor (i.e. SPOT VGT1 or SPOT VGT2; S_{VGT}^{k})

For each band k (= BLUE, RED, NIR, SWIR) of reference sensor (VGT1 or 2)

$$\textbf{Calculate } \rho_{BOA,g}^{k(VGT),model} = \frac{\int_{0}^{\infty} S_{VGT}^{k}(\lambda)\rho^{model}(\lambda)d\lambda}{\int_{0}^{\infty} S_{VGT}^{k}(k)(\lambda)d\lambda}$$

$$\text{With } \rho^{model}(\lambda) = \rho^{RPV\_BRDF(site\ g,\ \overline{\theta}_{s}^{new},\ \overline{\theta}_{v}^{new},\ \Lambda\overline{\phi}^{new}}$$

Ideally, the values $\rho_{BOA,g}^{k(VGT),model}$ obtained using the model would be identical to the actual VGT measured BOA reflectance values $\rho_{BOA,g}^{k,meas,VGT}$

In practice this will not be the case.

We now intend to calculate an adjusted desert spectrum $\rho^{adjusted\,model}(\lambda)(\rho_{BOA,g}^{meas,VGT})$ for which they are identical:

$$\rho^{k,adjusted\,model}(\lambda)(\rho_{BOA,g}^{meas,VGT}) = \rho_{BOA,g}^{k,meas,VGT}$$

Once the adjusted spectrum is known, the responses for all spectral bands as they were obtained from the PROBA-V sensor can be calculated in a straightforward way as follows:

For each band k (= BLUE, RED, NIR, SWIR) of PROBA-V

$$\textbf{Calculate}\;\; \rho_{BOA,g}^{k(PROBA-V),adjusted\,model} = \frac{\int_0^\infty S_{PROBA-V}^k(\lambda)\rho^{adjusted\,model}(\lambda)(\rho_{BOA,g}^{meas,VGT})d\lambda}{\int_0^\infty S_{PROBA-V}^k(k)(\lambda)d\lambda}$$

The main issue is the calculation of the adjusted desert spectrum $\rho^{adjusted\,model}(\lambda)(\rho_{BOA,g}^{meas,VGT})$.

For each of the spectral bands, the solution has to obey the equality $\rho^{k,adjusted\,model}(\lambda)(\rho_{BOA,g}^{meas,VGT}) = \rho_{BOA,g}^{k,meas,VGT}$. This still leaves open a large number of spectra as potential solutions. We will use a practical solution for which we determine an adjustment spectrum $Adj(\lambda)(\rho_{BOA,g}^{meas,VGT})$ which is defined as:

$$\rho^{k,adjusted\,model}(\lambda)(\rho_{BOA,g}^{meas,VGT}) = Adj(\lambda)(\rho_{BOA,g}^{meas,VGT}).\rho^{model}(\lambda)$$

As description of the model we choose a piecewise linear function, with a tie point at each of the peak wavelengths ($\lambda_{peak,VGT}^k$) of the VGT sensitivity curves. At each of the tie points, an adjustment factor (Adj_{VGT}^k) will be determined. The adjustment spectrum is then described as follows (assuming $\lambda_{peak,VGT}^k$ are in ascending order)

$$Adj(\lambda)(\rho_{BOA,g}^{meas,VGT}) = Adj(\lambda)(\;Adj_{VGT}^{k:first..last},\lambda_{peak,VGT}^{first}) = Adj_{VGT}^{first}$$

for $\quad \lambda \le \lambda_{peak,VGT}^{first}$

$$= \frac{(\lambda_{peak,VGT}^k - \lambda)}{(\lambda_{peak,VGT}^k - \lambda_{peak,VGT}^{k-1})}Adj_{VGT}^{k-1} + \frac{(\lambda - \lambda_{peak,VGT}^{k-1})}{(\lambda_{peak,VGT}^k - \lambda_{peak,VGT}^{k-1})}Adj_{VGT}^k$$

for $\quad \lambda_{peak,VGT}^{k-1} < \lambda \le \lambda_{peak,VGT}^k$

$$= Adj_{VGT}^{last}$$

for $\quad \lambda_{peak,VGT}^{last} < \lambda$

For adjustment spectra given with this functional form, the calculation of $\rho_{BOA,g}^{k,meas,VGT}$ can be split into independent parts:

$$\rho_{BOA,g}^{k,meas,VGT} = \rho^{k,adjusted\,model}(\lambda)(\rho_{BOA,g}^{meas,VGT}) = \frac{1}{\int\limits_{0}^{\infty} S_{VGT}^{k}(k)(\lambda)d\lambda}.$$

$$\int\limits_{0}^{\lambda_{peak,VGT}^{k}} S_{VGT}^{k}(\lambda)\rho^{adjusted\,model}(\lambda)(\rho_{BOA,g}^{meas,VGT})d\lambda$$

$$+ \sum\limits_{k=first+1}^{k=last} \int\limits_{\lambda_{peak,VGT}^{k-1}}^{\lambda_{peak,VGT}^{k}} S_{VGT}^{k}(\lambda)\rho^{adjusted\,model}(\lambda)(\rho_{BOA,g}^{meas,VGT})d\lambda$$

$$+ \int\limits_{\lambda_{peak,VGT}^{last}}^{\infty} S_{VGT}^{k}(\lambda)\rho^{adjusted\,model}(\lambda)(\rho_{BOA,g}^{meas,VGT})d\lambda$$

For the first and last terms, the adjusted model equals the unadjusted one, except for the fixed correction factors Adj_{VGT}^{first} and Adj_{VGT}^{last}. The middle terms can be split further into terms depending resp and on Adj_{VGT}^{k-1} and Adj_{VGT}^{k}.

$$\int\limits_{\lambda_{peak,VGT}^{k-1}}^{\lambda_{peak,VGT}^{k}} S_{VGT}^{k}(\lambda)\rho^{adjusted\,model}(\lambda)(\rho_{BOA,g}^{meas,VGT})d\lambda =$$

$$Adj_{VGT}^{k-1} \int\limits_{\lambda_{peak,VGT}^{k-1}}^{\lambda_{peak,VGT}^{k}} S_{VGT}^{k}(\lambda)\frac{(\lambda_{peak,VGT}^{k}-\lambda)}{(\lambda_{peak,VGT}^{k}-\lambda_{peak,VGT}^{k-1})}d\lambda + Adj_{VGT}^{k} \int\limits_{\lambda_{peak,VGT}^{k-1}}^{\lambda_{peak,VGT}^{k}} S_{VGT}^{k}(\lambda)\frac{(\lambda-\lambda_{peak,VGT}^{k-1})}{(\lambda_{peak,VGT}^{k}-\lambda_{peak,VGT}^{k-1})}d\lambda$$

Writing out the complete equations shows that the adjustment factors Adj_{VGT}^{k} appear all outside the integrals. The integrals can be computed, reducing the equation to a linear one, containing the 4 variables Adj_{VGT}^{k}. Such an equation is obtained for every band, so in total the problem is reduced to a set of 4 linear equations

The set of equations can be easily solved using standard linear algebra techniques, resulting in values for the adjustment factors, which cvompletley determined the adjustment spectrum, and in turn the reflectance values for the adjusted model.

4.10.1.2.5 Data comparison

Finally, an estimate of the cross-sensor calibration coefficient is obtained as the ratio of $\overline{\rho}_{BOA}^{new}$ to $\rho_{BOA}^{(PROBA-V),adjusted\,model}$.

$$A_{Cross,VGT/PROBA} = \frac{A_{VGT}}{A_{PROBA\_V}} = \frac{\overline{\rho}_{BOA}^{new}}{\rho_{BOA}^{(PROBA-V),adjusted\,model}}$$

4.10.1.2.6 Outlier removal and daily averaging

A daily average is calculated by averaging the results obtained over the different sites after outlier removal. A site is removed if it is detected as an outlier in at least one of the spectral bands. A robust outlier selection procedure based on the median and standard deviation from the median is used for this.

4.10.1.3 Error sources

The radiometric inter-comparison focuses on the concordance of the radiometric calibration of the different sensors. In order to be able to appreciate this concordance, it is necessary to know the order of magnitude of external sources of uncertainties. These are:

- The **differences of the spectral responses** for the compared similar bands or ,if corrected for, the **uncertainty on the spectral adjustment factor**
- The **variation of the target reflectance** itself due to the angular difference between two compared observations or due to stability of the target
- The variation of **aerosol** (AOT and model)
- The **inaccuracy of the geolocation** of the viewed pixels for each sensors
- **Uncertainty in meteo data** (H2O, O3, P)

For the shorter wavelengths (especially blue), atmospheric uncertainty (aerosol and meteo) will have the largest contribution to the total uncertainty. For the longer wavelengths, the variation of the target reflectance will have the largest impact.

5. GEOMETRIC CALIBRATION

See [PVDOC-981] Algorithm Theoretical Baseline Document Geometric Calibration

Appendix 1 FLOWCHART CONVENTIONS

Flow concepts are shown diagrammatically throughout the document. The convention for the various elements displayed in these diagrams is shown in Figure 41.
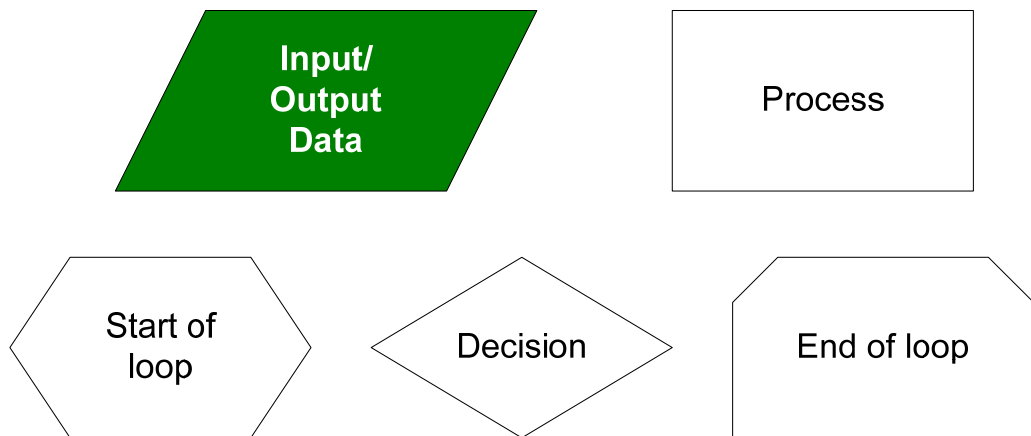

Figure 41: Conventions used in processing flow diagrams